

HYPERFINE INTERACTIONS AND NUCLEAR STRUCTURE

Thesis by

Menachem Levanoni

In Partial Fulfillment of the Requirements

For the Degree of

Doctor of Philosophy

California Institute of Technology

Pasadena, California

1970

(Submitted March 13, 1970)

ACKNOWLEDGMENTS

Some of the experiments reported here were carried out in collaboration with Dr. F.C. Zawislak and Dr. D.D. Cook. The author wishes to express his appreciation for their contributions to this work.

The author would also like to thank Drs. J.D. Bowman and E.N. Kaufmann who introduced him to the experimental technique and guided him during the early stages of this work.

Mr. H. Henrikson's contributions in designing the experimental apparatus, are gratefully acknowledged.

Finally, the author takes pleasure in expressing his sincere gratitude to Professor Felix Boehm for his constant interest and encouragement during the course of this work. Research with the Physics 34 group has been a pleasant and rewarding experience.

This work was supported in part by the United States Atomic Energy Commission.

ABSTRACT

An automatic experimental apparatus for perturbed angular correlation measurements, capable of incorporating Ge(Li) detectors as well as scintillation counters, has been constructed.

The gamma-gamma perturbed angular correlation technique has been used to measure magnetic dipole moments of several nuclear excited states in the osmium transition region. In addition, the hyperfine magnetic fields, experienced by nuclei of 'impurity' atoms embedded in ferromagnetic host lattices, have been determined for several '4d' and '5d' impurity atoms.

The following magnetic dipole moments were obtained in the osmium transition region

$$\mu_{2^+}({}^{190}\text{Os}) = 0.54 \pm 0.06 \text{ nm}$$

$$\mu_{4^+}({}^{190}\text{Os}) = 0.88 \pm 0.48 \text{ nm}$$

$$\mu_{2^+}({}^{192}\text{Os}) = 0.56 \pm 0.08 \text{ nm}$$

$$\mu_{2^+}({}^{192}\text{Pt}) = 0.56 \pm 0.06 \text{ nm}$$

$$\mu_{2^+}({}^{192}\text{Pt}) = 0.62 \pm 0.14 \text{ nm.}$$

These results are discussed in terms of three collective nuclear models; the cranking model, the rotation-vibration model and the pairing-plus-quadrupole model. The measurements are found to be in satisfactory agreement with collective descriptions of low lying nuclear states in this region.

The following hyperfine magnetic fields of 'impurities' in

ferromagnetic hosts were determined;

$$H_{\text{int}}(\text{Cd } \underline{\text{Ni}}) = - (64.0 \pm 0.8) \text{kG}$$

$$H_{\text{int}}(\text{Hg } \underline{\text{Fe}}) = - (440 \pm 105) \text{kG}$$

$$H_{\text{int}}(\text{Hg } \underline{\text{Co}}) = - (370 \pm 78) \text{kG}$$

$$H_{\text{int}}(\text{Hg } \underline{\text{Ni}}) = - (86 \pm 22) \text{kG}$$

$$H_{\text{int}}(\text{Tl } \underline{\text{Fe}}) = - (185 \pm 70) \text{kG}$$

$$H_{\text{int}}(\text{Tl } \underline{\text{Co}}) = - (90 \pm 35) \text{kG}$$

$$H_{\text{int}}(\text{Ra } \underline{\text{Fe}}) = - (105 \pm 20) \text{kG}$$

$$H_{\text{int}}(\text{Ra } \underline{\text{Co}}) = - (80 \pm 16) \text{kG}$$

$$H_{\text{int}}(\text{Ra } \underline{\text{Ni}}) = - (30 \pm 10) \text{kG},$$

where in $H_{\text{int}}(\underline{\text{AB}})$; A is the impurity atom embedded in the host lattice B. No quantitative theory is available for comparison. However, these results are found to obey the general systematics displayed by these fields. Several mechanisms which may be responsible for the appearance of these fields are mentioned.

Finally, a theoretical expression for time-differential perturbed angular correlation measurement, which duplicates experimental conditions is developed and its importance in data analysis is discussed.

TABLE OF CONTENTS

	<u>Page</u>
I INTRODUCTION	1
<u>PART 1: THE EXPERIMENTAL TECHNIQUE AND EXPERIMENTAL</u> <u>APPARATUS</u>	6
II DESCRIPTION OF THE PERTURBED ANGULAR CORRELATION TECHNIQUE	
1. Introduction	7
2. The Directional Angular Correlation between Gamma Rays Emitted in Cascade	7
3. Perturbation of the Angular Correlation by a Static Magnetic Interaction	12
4. Perturbation of the Angular Correlation by Fluctu- ating Electric or Magnetic Fields	13
5. Methods of Analysis of Time-Differential and Time- Integral Measurements	17
III DESCRIPTION AND OPERATION OF THE EXPERIMENTAL APPARATUS	
1. Introduction	21
2. The Correlation Table and its Operation	21
3. The Dual Slow/Fast Coincidence System	30
4. Production of External Magnetic Fields	36
5. Automatic Operation	40
6. Experimental Procedure	45

PART 2: MAGNETIC MOMENT MEASUREMENTS IN THE OSMIUM

	<u>REGION</u>	
		49
IV	THE MAGNETIC MOMENTS OF THE FIRST 2^+ AND 4^+ STATES IN ^{190}Os	
	1. Introduction	50
	2. Source Preparation	50
	3. The 2^+ State	51
	4. The 4^+ State	59
V	THE MAGNETIC MOMENT OF THE FIRST 2^+ STATE IN ^{192}Os	
	1. Introduction	61
	2. Source Preparation	66
	3. The Gamma-Gamma Cascade	66
	4. The Method and Results	67
VI	THE MAGNETIC MOMENTS OF THE FIRST AND SECOND 2^+ STATES IN ^{192}Pt	
	1. Introduction	69
	2. The First 2^+ State	69
	3. The Second 2^+ State	71
VII	DISCUSSION OF EXPERIMENTAL RESULTS	
	1. Summary of Magnetic Moments in the Osmium Region	73
	2. Collective Nuclear Models and the Osmium Region	75
	(a) Introduction	75
	(b) The Cranking Model	76
	(c) The Rotation-Vibration Model	79
	(d) The Pairing-Plus-Quadrupole Model	82
	(e) Discussion	86

<u>PART 3: HYPERFINE MAGNETIC FIELDS AT "IMPURITY" ATOMS</u>		
	<u>IN FERROMAGNETIC HOSTS</u>	89
VIII	INVESTIGATION OF INTERNAL MAGNETIC FIELDS OF ^{111}Cd IN NICKEL	
	1. Introduction	90
	2. Preparation of Sources	90
	3. The Gamma-Gamma Cascade	91
	4. Experimental Procedure	94
	5. Data Analysis and Results	95
IX	THE INTERNAL MAGNETIC FIELDS AT Hg SITES IN Ni, Co, AND Fe HOSTS	
	1. Introduction	103
	2. Source Preparation and the Cascade	103
	3. Results	106
X	THE HYPERFINE MAGNETIC FIELDS EXPERIENCED BY Tl NUCLEI IN THE FERROMAGNETS	
	1. Introduction	107
	2. Source Preparation	107
	3. The Gamma-Gamma Cascade and Results	109
XI	THE MAGNETIC MOMENT OF THE 50 keV, $3/2^-$ STATE IN ^{223}Ra AND THE INTERNAL MAGNETIC FIELDS ACTING ON Ra NUCLEI DIFFUSED INTO FERROMAGNETIC HOSTS	
	1. Introduction	111
	2. The Magnetic Moment of the $3/2^-$ State	111

3.	Preparation of Ferromagnetic Sources	115
4.	Experimental Techniques and Results	115
XII	DISCUSSION OF EXPERIMENTAL RESULTS	
1.	Summary of Experimental Results	118
2.	Status of Theoretical Investigations	120
	APPENDIX A: ANALYSIS OF TIME-DIFFERENTIAL MEASUREMENTS	
1.	Introduction	126
2.	The General Theoretical Expression	129
3.	Time Dispersion in the Detector System	130
4.	Time Dispersion in the 'Electronics' Section	131
5.	Time Response of the Detector-Plus-'Electronics' System	132
6.	The Modified Perturbed Correlation Function	133
7.	Time-Dispersion in the Multichannel Analyzer	135
8.	The Observed, Discrete Perturbed Angular Correlation Function	135
9.	Useful, Simplified Versions of the Observed Correlation	139
	APPENDIX B: SOURCE THICKNESS EFFECTS ON ANGULAR CORRELATIONS	141
	REFERENCES	143

I INTRODUCTION

The measurements described in this manuscript deal with two, related, branches of physics, namely nuclear structure and hyperfine interactions. The common factor is the experimental technique of perturbed angular correlation, which very often makes use of hyperfine interactions as a nuclear probe. The discussion is presented in three parts.

In part one the experimental technique and apparatus are described. Chapter II reviews the perturbed angular correlation technique. Perturbations relating from the interactions of nuclei with their environment are discussed. Specific measuring techniques and data analysis methods are also described. Chapter III describes in detail an experimental apparatus which was used in most of the measurements described below. This automatic system, capable of incorporating any combination of Ge(Li) and scintillation detectors, has been used to improve existing measuring techniques. In effect, it enables data collection and analysis at twice the rate of the conventional system. The automatic operation of this system is described in enough detail to permit easy duplication.

Part two is devoted to magnetic dipole moments of excited states in the osmium region.

Nuclear ground-state spins and magnetic moments, determined from nuclear magnetic resonance, atomic and molecular beam, and optical spectroscopy experiments have played a large part in the development of the nuclear shell model. The use of Mössbauer

effect and perturbed angular correlation methods has permitted the measurement of spins and moments of nuclear excited states. Based on these and other spectroscopic properties of excited states in nuclei, theoretical descriptions of nuclear structure have been developed, which account for many of the observed nuclear properties. In fact, large deviations of measured magnetic moments from shell model predictions were instrumental in the discovery of collective excitations.

Collective excitations in nuclei are usually divided into two groups; "spherical" nuclei exhibit energy spectra which could be explained in terms of vibrations about a spherical core. These are the so-called vibrational nuclei found near closed shells. The "deformed" nuclei display energy level bands, similar to those found in molecular spectra, which are described as rotational bands of a deformed rigid rotor. These nuclei are found in regions away from closed shells. In between the spherical and deformed regions a third class of nuclei is found. These exhibit large deviations from both the rotational and the vibrational excitation models. Such is the case of the osmium transition region, a region of disappearance of nuclear deformation. This region, which includes the isotopes of W, Os, and Pt, has been used for a number of years as a critical testing ground of nuclear structure models. Chapters IV, V, and VI describe the measurements of five magnetic moments of low excited states in ^{190}Os , ^{192}Os , and ^{192}Pt , respectively. The results are discussed and compared with collective nuclear models, in Chapter VII. Three such models are discussed: the cranking model, the rotation-

vibration model, and the pairing-plus-quadrupole model. The pairing-plus-quadrupole model currently offers the best microscopic description of collective excitations in nuclei, over a wide range of the periodic table. It is the only successful collective model, so far, in which no a priori assumptions about the nuclear shape, were made. It is therefore capable of investigating "vibrational" nuclei, "rotational" nuclei, and in particular, nuclei in transition regions. Until recently, the osmium-transition region has been carefully avoided by theorists who wished to compare their predictions with experimental results.

Part three deals with hyperfine interactions. This field has been growing steadily in recent years and provides valuable data in the understanding of magnetic and electric properties of solids. Its growth started from within nuclear physics by experimentalists who, for the last ten years, have been utilizing the strong hyperfine interactions to probe the nucleus.

The hyperfine magnetic field at a nucleus of an atom in a ferromagnetic crystal has a complex origin. It involves phenomena incompletely understood even for the elemental crystals such as Fe, Co, and Ni. Substituting one ferromagnetic atom by an 'impurity' atom, further complicates theoretical investigation and indeed this problem is largely unresolved. These fields exhibit systematic oscillatory behavior (apart from the rare earths region) as a function of the atomic number of the impurity atoms. A quantitative theory which describes these systematics is non-existent. In fact,

recent attempts encountered difficulties in predicting the correct signs of several observed fields (the sign is determined relative to the external field needed to polarize the ferromagnetic domains). The mechanisms responsible for these internal fields, are presumably known. However, theoretical investigations are very difficult and reflect our poor understanding of the solid state and in particular, magnetism. Chapters VIII, IX, X and XI describe measurements of nine hyperfine magnetic fields. They were performed on Cd, Hg, Tl, and Ra nuclei, embedded in the ferromagnetic host lattices of Fe, Co, and Ni. The measurement on Cd was a search for internal magnetic fields other than the field experienced by those Cd nuclei whose atoms are located in regular sites. The Hg measurement resolved large discrepancies in earlier results. The measurements on Tl and Ra are particularly important since they are in regions where, from systematics, one expects the hyperfine fields to change their signs. As such, these measurements are sensitive tests of forthcoming hyperfine interaction models. In Chapter XII the experimental results are summarized. The status of current theoretical investigations is also discussed.

Appendices A and B treat two experimental difficulties related to the measuring techniques. In Appendix A an expression is developed for the time-differential perturbed angular correlation measurement, which takes into account all time-dispersions in the response of various components of the experimental apparatus to timing information. The importance of the various terms in it is also discussed. In Appendix B, the effects of the thickness of

sources, used in an angular correlation experiment, are discussed and the necessity for use of thin sources in the case of low energy gamma rays is demonstrated.

The large number of individual experiments reported here made a concise description of them a necessity. These experiments can be found (in almost as much detail) in Refs. (1), (2), (3), and (4).

PART 1: THE EXPERIMENTAL TECHNIQUE AND EXPERIMENTAL APPARATUS

The perturbed angular correlation technique is an experimental method which permits the measurement of the Larmor precession frequency of the magnetic moment (or spin) of an excited state of a nucleus, under the influence of a static magnetic field. It makes use of the fact that the preferred direction of emission of electromagnetic radiation from a radioactive nucleus depends on the nuclear spin orientation in space. The experimental system consists basically of two, gamma sensitive detectors. One detector is stationary and is used to define a preferred direction in space with respect to which the other, movable detector is used to trace the angular correlation pattern. The introduction of high resolution Ge(Li) detectors, made possible the use of this technique in many cases (such as the ones described here) of interest to the nuclear physicist as well as the solid state physicist.

II. DESCRIPTION OF THE PERTURBED ANGULAR CORRELATION TECHNIQUE

II.1 Introduction

In 1950, Brady and Deutsch⁽¹⁾ recognized the possibility of measuring the g-factors of nuclear excited states using an anisotropic angular correlation between gamma rays emitted in cascade. Aepli et al.⁽²⁾ performed the first such measurement in 1951. Since that time the technique has been used extensively, and improvements in electronics and radiation detectors in recent years have allowed the measurement of moments previously inaccessible. The complete mathematical treatment of the theory of angular correlations is to be found in several comprehensive articles⁽³⁾. A short outline of the theoretical results needed to analyze data collected in our experiments is presented below.

II.2 The Directional Angular Correlation between Gamma Rays Emitted in Cascade

The probability of emission of a gamma ray from a nucleus depends on the angle between the emission direction and the nuclear spin axis. Generally, in a radioactive sample the nuclear spins are randomly oriented leading to an isotropic emission pattern for gamma rays. However, the observation of the direction of emission of the first gamma ray of a gamma-gamma cascade selects an ensemble of nuclei whose spins have a preferred orientation in space relative to the observed propagation direction. If one then measures the emission direction of the second member of the cascade, it will in general show an anisotropic distribution about the direction of emission of the first.

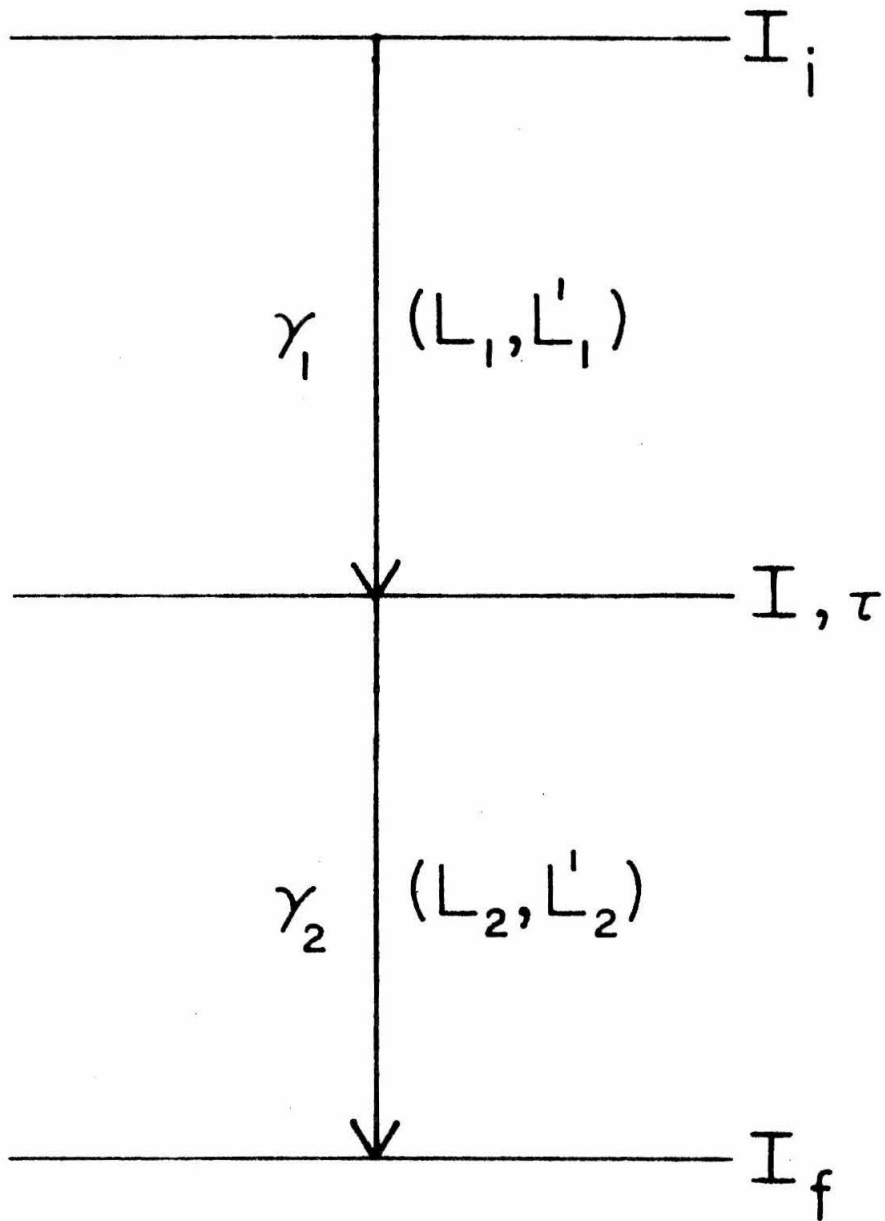


Figure 1

Ideal gamma-gamma cascade. The symbols are defined in the text.

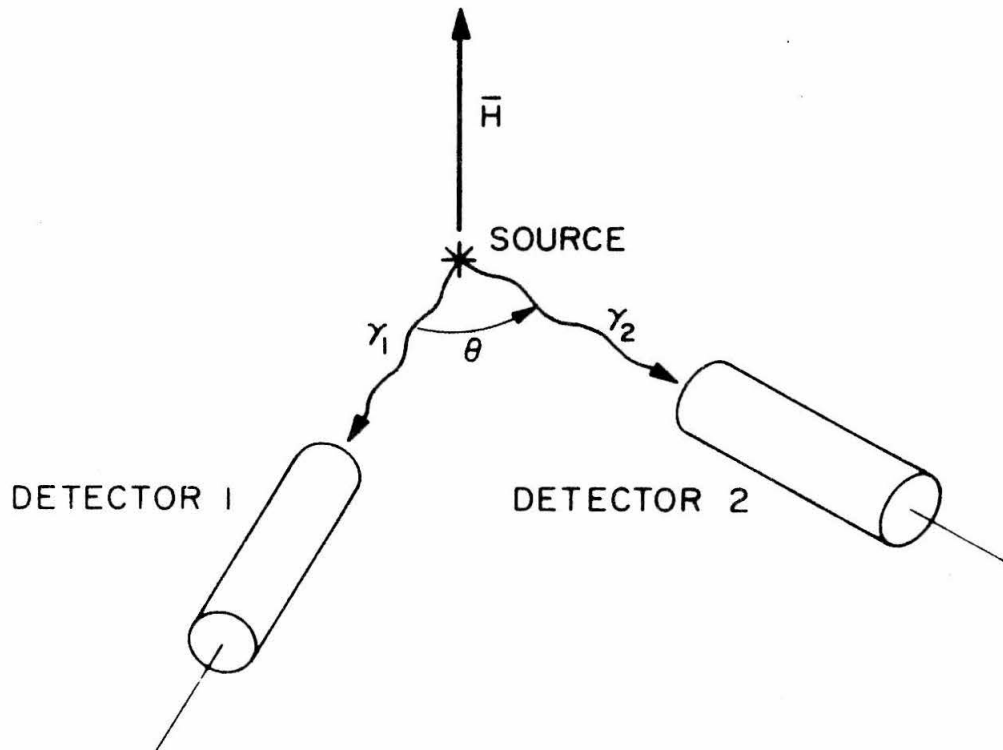


Figure 2

Geometrical arrangement of the source, detector, and magnetic field
in a perturbed angular correlation experiment.

An idealized gamma-gamma cascade is depicted in Figure 1, where I_i , I , and I_f are the spins of the initial, intermediate, and final state, respectively. The two gamma rays, γ_1 and γ_2 , have multiplicities (L_1, L_1') and (L_2, L_2') . The notation (L, L') indicates a possibly mixed multipole transition: for instance, for a mixed M1 + E2 (or E1 + M2) transition, L and L' would be equal to 1 and 2, respectively. If γ_1 and γ_2 are detected by counters separated by the angle θ in the geometry shown in Figure 2, then the probability distribution for the observation of γ_2 at the angle θ relative to γ_1 is given by

$$W(\theta) \propto 1 + \sum_{\substack{k=2 \\ \text{(even)}}}^{k_{\max}} A_{kk} P_k(\cos \theta). \quad (1)$$

The $P_k(\cos \theta)$ are Legendre polynomials and the coefficients A_{kk} depend on the spins of the nuclear states, I_i , I , and I_f , and the multiplicities of the two gamma radiations, (L_1, L_1') and (L_2, L_2') . It turns out that the A_{kk} can be written in the factored form⁽⁷⁾,

$$A_{kk} = A_k(\gamma_1) \cdot A_k(\gamma_2), \quad (2)$$

where $A_k(\gamma_1)$ and $A_k(\gamma_2)$ each depend on the properties of only one of the transitions of the cascade. For a mixed multipole transition, $A_k(\gamma)$ has the explicit form⁽⁴⁾,

$$A_k(\gamma_1) = \frac{F_k(L_1 L_1' I_i I) + 2\delta(\gamma_1) F_k(L_1 L_1' I_i I) + \delta^2(\gamma_1) F_k(L_1' L_1' I_i I)}{1 + \delta^2(\gamma_1)}, \quad (3)$$

where the F_k are tabulated coefficients⁽⁵⁾ and the mixing amplitude δ is defined as the ratio of the reduced transition matrix element for the higher multipole, to that of the lower multipole;

$$\delta(\gamma_1) = \langle I ||L_1' \pi_1' ||I_i \rangle / \langle I ||L_1 \pi_1 ||I_i \rangle. \quad (4)$$

A similar expressions holds for $A_k(\gamma_2)$. Thus, the measurement of A_{kk} can determine the size and sign of a mixing amplitude.

In practice, radiation detectors subtend a finite solid angle. Therefore, the detection of γ_1 and γ_2 indicates that the angle between emission directions falls in a range of angles centered about θ . Also the detection efficiency for gamma-ray pairs within this range of angles is not uniform, because the efficiency of each detector depends on the path length traversed by the radiation in the active detector volume. The replacement of A_{kk} in Eq. (1) by $Q_k^1 Q_k^2 A_{kk}$ is needed to account for these effects, where Q_k^1 and Q_k^2 are correction factors for the smearing of the angular correlation in the detector accepting γ_1 and γ_2 , respectively. In the following, the Q_k 's will not be written explicitly but are understood to be present in all experimentally measured angular correlation coefficients. The index k of the sum in Eq. (1) must satisfy the inequality

$$0 < k < \text{Min} (2I, L_1 + L_1', L_2 + L_2') \quad (5a)$$

for mixed multipole radiation and

$$0 < k < \text{Min} (2I, 2L_1, 2L_2) \quad (5b)$$

for pure multipole radiation. In all measurements reported here, k_{max} is not greater than 4.

II.3 Perturbation of the Angular Correlation by a Static Magnetic Interaction

The presence of an electromagnetic field at the nucleus, while it is in the intermediate state with spin I , will cause transitions among the $(2I + 1)$ magnetic substates corresponding to different projections of the spin on the chosen direction of the quantization axis. In other words, the preferred direction of orientation of the spin vector in the intermediate state is altered, thereby changing the angular correlation. The application of a static magnetic field causes a precession of the nuclear spin about the applied field direction with the Larmor frequency

$$\bar{\omega} = -g\mu_N\bar{H}/\hbar, \quad (6)$$

in which \bar{H} is the applied magnetic field, g is the nuclear g -factor of the intermediate state, and μ_N is the nuclear magneton. If \bar{H} is perpendicular to the plane of the detectors (cf. Fig. 2) and γ_2 is emitted after the nucleus has been in the intermediate state for a time t , then the angular correlation pattern will be of the form,

$$W(\theta, H, t) \propto 1 + \sum_{\substack{k=2 \\ \text{(even)}}}^k A_{kk} P_k(\cos(\theta - \omega t)). \quad (7)$$

The observed pattern is obtained by multiplying Eq. (7) by the probability that γ_2 will be emitted at time t after the emission of γ_1 . This is given by a Poisson distribution.

$P(t) = \frac{1}{\tau} e^{-t/\tau}$ where τ is the mean life of the intermediate state in the cascade. The result, in three equivalent forms, is given by

$$\begin{aligned}
WT(\theta, H, t) &\propto \frac{1}{\tau} e^{-t/\tau} \left[1 + \sum_{\substack{k=2 \\ \text{(even)}}}^k A_{kk} P_k(\cos(\theta - \omega t)) \right] \\
&\propto \frac{1}{\tau} e^{-t/\tau} \left[1 + \sum_{\substack{k=2 \\ \text{(even)}}}^k b_k \cos(k\theta - k\omega t) \right] \quad (8) \\
&\propto \frac{1}{\tau} e^{-t/\tau} \left[1 + \sum_{\substack{k=2 \\ \text{(even)}}}^k c_k (\cos(\theta - \omega t))^k \right]
\end{aligned}$$

where

$$b_2 = \frac{\frac{3}{4} A_{22} + \frac{5}{16} A_{44}}{1 + \frac{1}{4} A_{22} + \frac{9}{64} A_{44}} \quad , \quad b_4 = \frac{\frac{35}{64} A_{44}}{1 + \frac{1}{4} A_{22} + \frac{9}{64} A_{44}}$$

and

$$c_2 = \frac{\frac{3}{2} A_{22} - \frac{15}{4} A_{44}}{1 - \frac{1}{2} A_{22} + \frac{3}{8} A_{44}} \quad , \quad c_4 = \frac{\frac{35}{8} A_{44}}{1 - \frac{1}{2} + \frac{3}{8} A_{44}} \quad .$$

Equation (8) describes the pattern which would have been observed experimentally if the experimental apparatus had a perfect time response. However, since the correlation apparatus has a characteristic resolving time τ_0 , the observed pattern depends on the relative magnitudes of τ_0 and the mean life of the intermediate state τ . If $\tau_0 \ll \tau$ the observed pattern resembles closely that of Eq. (8). If $\tau_0 \approx \tau$, time dispersions in the experimental system interfere with the angular distribution pattern resulting in a modification of the correlation. This will also happen if $\tau_0 \approx 1/\omega$ unless the time

response of the apparatus is taken into account in data analysis. Appendix A describes in detail the intrinsic time dispersions in the various components of a typical experimental apparatus and presents a modified expression, for the time differential perturbed angular correlation, which duplicates experimental conditions. If $\tau_0 \gg \tau$ the observed correlation pattern will be that of Eq. (8), integrated over all time, resulting in the integral correlation

$$\overline{W(\theta, H)} = \frac{1}{\tau} \int_0^{\infty} e^{-t/\tau} W(\theta, H, t) dt \propto 1 + \sum_{\substack{N=2 \\ \text{(even)}}}^k \frac{b_N \cos(N\theta - N\Delta\theta)}{\sqrt{1 + (N\omega\tau)^2}} \quad (9)$$

where $\tan(N\Delta\theta) = N\omega\tau$.

II.4 Perturbation of the Angular Correlation by Fluctuating Electric or Magnetic Fields

In addition to fields applied by the experimenter, the nuclei under study experience magnetic fields and electric field gradients arising from their chemical environment. These fields fluctuate in time with the thermal vibrations in a solid or molecular collisions in a liquid. The fluctuations of the fields' magnitudes and directions are, in most cases, random in time. The effect of these time-dependent interactions on an angular correlation has been treated by Abragam and Pound⁽⁶⁾. To characterize the randomness of the fluctuations, they define a "correlation function" $G(T)$ as the ensemble average of the product $\langle f(t)f(t - T) \rangle$, where $f(t)$ is some scalar random function of time. The function $G(T)$ indicates the degree to which the value of 'f' at time 't' can be predicted from a knowl-

edge of 'f' at the earlier time 't - T'. Abragam and Pound⁽⁶⁾ assume that the form $G(T) = G(0) \cdot \exp(-T/\tau_c)$ applies to the case of a liquid source. The constant τ_c , so defined, is known as the correlation time and represents the time after which $f(t)$ has significantly changed its value. When taking the time-dependent perturbing fields into account, they find that Eqs. (1) and (7) are modified to

$$W(\theta, t) \propto 1 + \sum_{\substack{k=2 \\ \text{(even)}}}^{k_{\max}} \exp(-\lambda_k t) A_{kk} P_k(\cos \theta) \quad (10)$$

and

$$W(\theta, H, t) \propto 1 + \sum_{\substack{k=2 \\ \text{(even)}}}^{k_{\max}} \exp(-\lambda_k t) A_{kk} P_k(\cos(\theta - \omega t)), \quad (11)$$

respectively. The exponential character of the attenuation factors has been predicted by Dillenburg and Maris⁽⁷⁾ for an interaction random in space and time, regardless of the nature, strength, or frequency of the interaction. The constant λ_k is proportional to the correlation time τ_c . Specifically, for an electric interaction⁽⁸⁾

$$\lambda_k = \frac{\tau_c}{40} \frac{(I+1)(2I+3)}{(2I-1)I} \left(\frac{eQ}{\hbar} \right)^2 \left(\frac{\partial^2 V}{\partial z^2} \right)^2 [1 - (2I+1)W(I, 2kI, II)], \quad (12)$$

and for a magnetic interaction⁽⁸⁾

$$\lambda_k = \frac{2\tau_c}{3} I(I+1) \left(\frac{g\mu_N H_{\text{int}}}{\hbar} \right)^2 [1 - (2I+1)W(I, kI, II)]. \quad (13)$$

The undefined quantities are the electric quadrupole moment of the intermediate state, Q , the g -factor of that state, g , the electric field gradient and magnetic field at the nucleus, $\partial^2 V / \partial z^2$ and H_{int} ,

respectively, and the Racah⁽⁹⁾ coefficients, W.

The total time integrated correlation functions corresponding to Eqs. (10) and (11) are

$$\overline{W(\theta)} \propto 1 + \sum_{\substack{k=2 \\ \text{(even)}}}^{k_{\max}} G_{kk} A_{kk} P_k(\cos \theta) \quad (14)$$

and, the complex but manageable expression for $k_{\max} = 4$,

$$\begin{aligned} \overline{W(\theta, H)} \propto & 1 + \frac{1}{4} A_{22} G_{22} \left\{ 1 + \frac{3 \cos(2\theta - 2\Delta\theta_{22})}{[1 + (2\omega\tau G_{22})^2]^{1/2}} \right\} + \\ & + \frac{1}{64} A_{44} G_{44} \left\{ 9 + \frac{20 \cos(2\theta - 2\Delta\theta_{24})}{[1 + (2\omega\tau G_{44})^2]^{1/2}} + \frac{35 \cos(4\theta - 4\Delta\theta_{44})}{[1 + (4\omega\tau G_{44})^2]^{1/2}} \right\}, \end{aligned} \quad (15)$$

respectively, where $\tan(N\Delta\theta_{Nk}) = N\omega\tau G_{kk}$ and $G_{kk} = 1/(1 + \lambda_k\tau)$.

These effects are clarified by the following simple argument. The integrated correlation function including the exponential attenuation is given by

$$\overline{W(\theta, H)} \propto 1 + \sum_{\substack{k=2 \\ \text{(even)}}}^{k_{\max}} \frac{1}{\tau} \int_0^{\infty} e^{-t/\tau} A_{kk} e^{-\lambda_k t} P_k(\cos(\theta - \omega t)) dt \quad (16)$$

using the substitution $t = \frac{1}{1 + \lambda_k\tau} T = G_{kk} T$ we obtain

$$\overline{W(\theta, H)} \propto 1 + \sum_{\substack{k=2 \\ \text{(even)}}}^{k_{\max}} \frac{1}{\tau} \int_0^{\infty} e^{-T/\tau} G_{kk} A_{kk} P_k(\cos(\theta - \omega G_{kk} T)) dT. \quad (17).$$

Equation (17) is seen to be identical to the expression for $\overline{W(\theta, H)}$ obtained for a rotated angular correlation without attenuation but

which has the angular correlation coefficients $A'_{kk} = A_{kk} G_{22}$, and which is rotated with the Larmor precession frequencies $\omega'_{kk} = \omega_L G_{kk}$. Therefore, not only is the angular correlation attenuated, but also the precession frequency is effectively reduced.

In the measurements on osmium and platinum, the radioactive atom is assumed to be located in a regular lattice site of cubic Fe metal. The short intermediate state lifetime, $\tau \approx 10^{-11}$ sec., and the absence of an electric quadrupole interaction in a cubic symmetry indicate the product $\lambda_k \tau$ is very small and the integral attenuation coefficients G_{kk} are approximately unity. The g-factor measurement of the 50 keV state in Ra²²³ was performed with a liquid source. Also, this state has a rather long lifetime ($\tau = 9.1 \times 10^{-10}$ sec) so that considerable attenuation was expected. However, no such attenuation could be found and the angular correlation coefficients (corrected for finite solid angles subtended by the detectors) agreed well with the theoretical values given by Eqs. (2) and (3).

On the other hand, the attenuations found in the Ra Ni, Ra Co and Ra Fe sources cannot be explained as resulting from magnetic interactions. Scattering of the 50 keV gamma ray in the source material is partially responsible for the observed attenuation while electric quadrupole effects could explain the rest.

II.5 Methods of Analysis of Time-Differential and Time-Integral Measurements

In a time-differential measurement, the Larmor frequency of precession is determined directly from Eq. (8). In practice, the

magnetic field is usually reversed periodically and the quantity

$$R(\theta, t) = \frac{WT(\theta, +H, t) - WT(\theta, -H, t)}{WT(\theta, +H, t) + WT(\theta, -H, t)} = \frac{\sum_{k=2}^{k_{\max}} b_k \sin(k\theta) \sin(k\omega t)}{1 + \sum_{k=2}^{k_{\max}} b_k \cos(k\theta) \cos(k\omega t)} \quad (18)$$

which is independent of the lifetime of the intermediate state, is determined. The measurements in Cd¹¹¹ (Chapter VIII) were analyzed in terms of the difference $WT(\theta, +H, t) - WT(\theta, -H, t)$ and the mean life of the intermediate state was also determined.

In all other measurements, the integral correlation was observed. In such cases, the spin rotation angle $\omega\tau$ is determined. It represents the mean angle of precession of the nuclear spin while in the intermediate state.

Three different methods are often used in obtaining $\omega\tau$.

(a) In the integral-rotation method, the angular correlation is measured first without and then with the perturbing magnetic field and the mean precession angle $\omega\tau$ is determined from Eq. (9). The measurements of the 2^+ state of ¹⁹⁰Os and of the Ra Fe alloy were performed with an improved version of this method in which the angular correlation parameters and the field effect parameters were determined simultaneously.

(b) In the integral-reverse-field method, the magnetic field direction is reversed periodically and the ratio

$$R(\theta) = \frac{\overline{W(\theta, +H)} - \overline{W(\theta, -H)}}{\overline{W(\theta, +H)} + \overline{W(\theta, -H)}}, \quad (19)$$

which is independent of the normalization of the function $\overline{W(\theta, H)}$, is determined. In most available cases, $\omega_T \ll 1$. Equation (19) then simplifies considerably and one gets:

$$R(\theta) = \frac{-2b_2 \sin(2\theta) - 4b_4 \sin(4\theta)}{1 + b_2 \cos(2\theta) + b_4 \cos(4\theta)} \omega_T + O[(\omega_T)^3]. \quad (20)$$

Thus, the field reversal ratio $R(\theta)$ is proportional to the mean precession angle ω_T . The proportionality constant represents the logarithmic derivative $\overline{\partial W(\theta)}/\overline{W(\theta)}$ of the angular distribution. Most of the measurements described below were performed using this method.

(c) Equation (9) was derived on the assumption that each detector is used to detect only one gamma ray in the investigated cascade. If, however, both detectors are used to detect both γ_1 and γ_2 , the observed correlation is described by a superposition of two functions of the form (9), describing rotations in opposite directions. A rotation is no longer present and only an attenuation of the angular correlation pattern can be observed:

$$\overline{W_{\text{atten}}(\theta, H)} \propto 1 + \sum_{\substack{N=2 \\ \text{(even)}}}^k \frac{b_N}{1 + (N\omega_T)^2} \cos(N\theta). \quad (21)$$

Use of this, the integral-attenuation method is limited to cases in which the mean precession angle is appreciable ($\omega_T \approx 1$) because of counting statistics. Also, only the magnitude of ω_T can be determined by this method. However, if, as in the cases of the 2^+ state in

^{190}Os and the Ra Fe alloy mentioned above, the two opposite precessions can be separated, a significant improvement is achieved.

In all integral measurements the quantity actually determined is the mean precession angle. At present, a value for ω_T of about 0.01 radians is the smallest one can measure with good accuracy. For a g-factor of ≈ 0.3 and a mean life of $\approx 10^{-9}$ sec, Eq. (6) indicates that a magnetic field of about 6 kG may be sufficient to produce a measurable ω_T . This is the case for the measurement of the magnetic moment in Ra²²³ described in Chapter XI. In the measurements on osmium and platinum (cf. part 2) the lifetimes of all but one of the investigated states are of the order of 10^{-11} sec. For these, a magnetic field of at least 500 kG is needed. No laboratory magnet can produce such a large field. In these cases, the large internal hyperfine fields at the sites of osmium or platinum nuclei in a ferromagnetic lattice were utilized in the measurements of magnetic moments. On the other hand, in the measurements on thalium, mercury, and radium, knowledge of g-factors allowed measurements of several hyperfine fields of particular interest to the growing field of hyperfine interactions.

III. DESCRIPTION AND OPERATION OF THE EXPERIMENTAL APPARATUS

III.1 Introduction

The perturbed angular correlation apparatus described below was constructed during the spring and summer of 1968. The correlation table was designed by Mr. H. Henrikson of Physics 34, and all parts were expertly machined by Mr. V. Stephensen at the central engineering shop. Digital electronic circuits, necessary for complete automation of the apparatus were designed and built by the author, as well as several interface units (routing, gating, etc.). Commercial units were used in the coincidence circuits themselves. Actual experimentation with this apparatus started in September 1968.

The design criteria of the apparatus were as follows. It should be reliable over an extended length of time. Its properties should be independent of small temperature fluctuations with time. It should be capable of using two Ge(Li) detector systems, two scintillation spectrometers, or a combination of both types. It should be capable of mounting small aligning magnets as well as large electromagnets, and it should be fully automated. The results are described in detail, below.

III.2 The Correlation Table and its Operation

The correlation table, shown in Figs. 3 and 4, consists of four sections: a circular rail, a motorized carriage, a clamped carriage and a center post.

The circular rail supports both carriages and the center post. The carriages are constrained to rotate about the center post. One



Figure 3: The correlation table utilizing two Ge(Li) detectors. The radioactive source is fixed between the pole tips of the magnet on the center post. The motorized carriage is at left of picture.



Figure 4: The correlation table with a Ge(Li) detector and a scintillation counter.

carriage is clamped in a fixed position while the other is allowed to rotate through a maximum angle of 180° . A 1/50 HP, 115 VDC motor is mounted under the rotating carriage. A spur-gear on the motor shaft engages a large diameter ring-gear which is concentric with the circular rail. The two detector systems are set on their respective carriages, facing the center post. The center post supports the aligning magnet and the radioactive source. Its height is adjustable to allow lining up of the source with the detectors.

Angular positions are precisely marked on the rail, in steps of 1° . In addition, there are seventy-two holes in increments of 5° on the rail. One-half inch diameter steel pins are secured, at preset angles, in their respective holes (special attachments are available for any angle between two holes). The moving system is stopped at the preset angles by means of a latching device. The accuracy of this arrangement is better than one minute of arc.

The latching device, shown in Figs. 5 and 6, is located inside the motorized carriage. It consists of a spring loaded latching yoke, a potentiometer, a push-button switch and a solenoid. The latching yoke engages the steel pins on the rail. The potentiometer controls the current supplied to the motor's armature circuit (cf. Fig. 7). The switch is of the double-pole, double-throw type. When actuated, it first opens the motor's armature circuit, stopping the motor. It then shorts the armature circuit to suppress harmful induced currents in it. The solenoid is used to disengage the latching yoke.

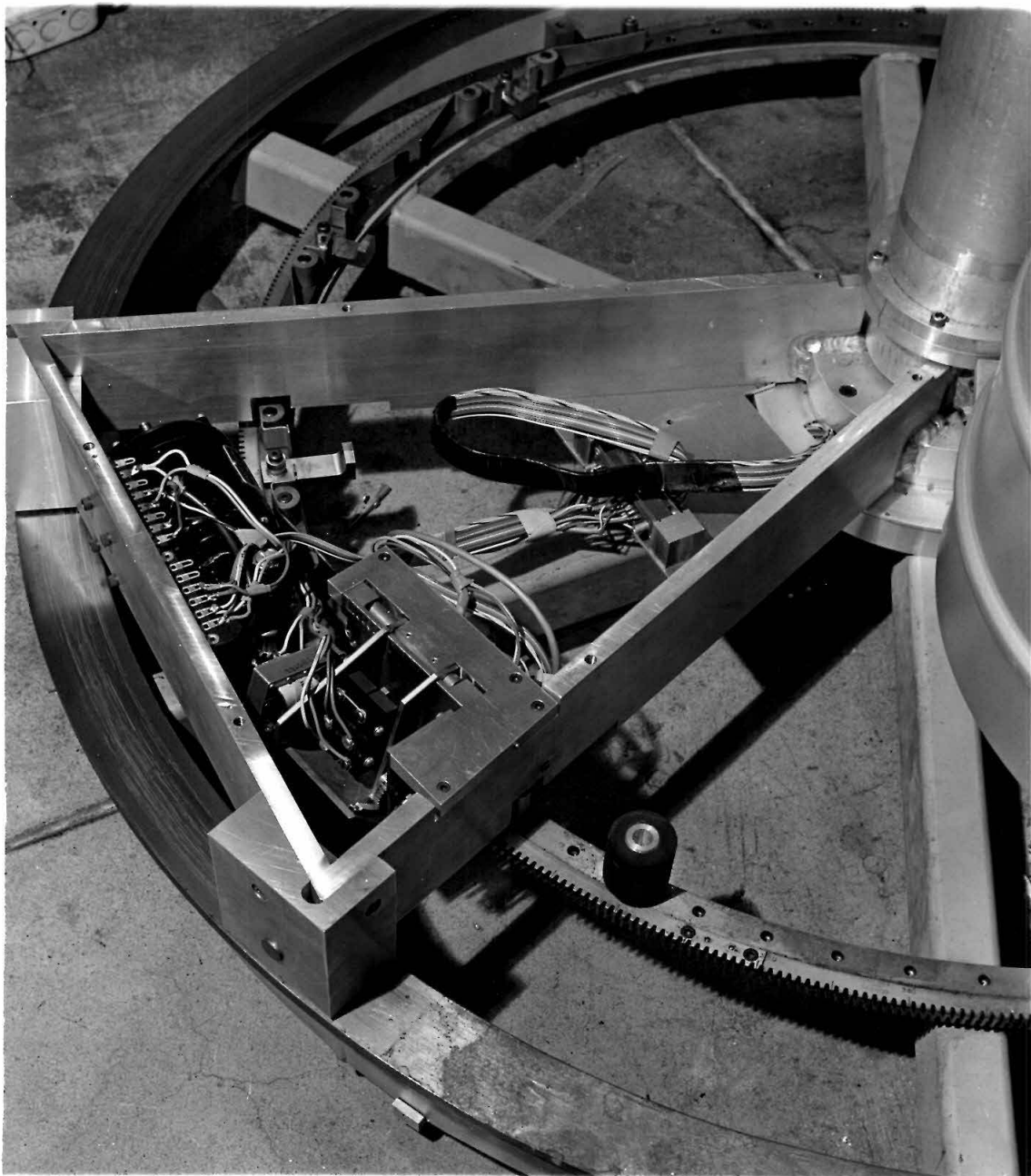


Figure 5: The motorized carriage with its DC motor and latching device. The solenoid which disengages the latching yoke and the "brake" switch which stops the motor, are clearly visible. See text.

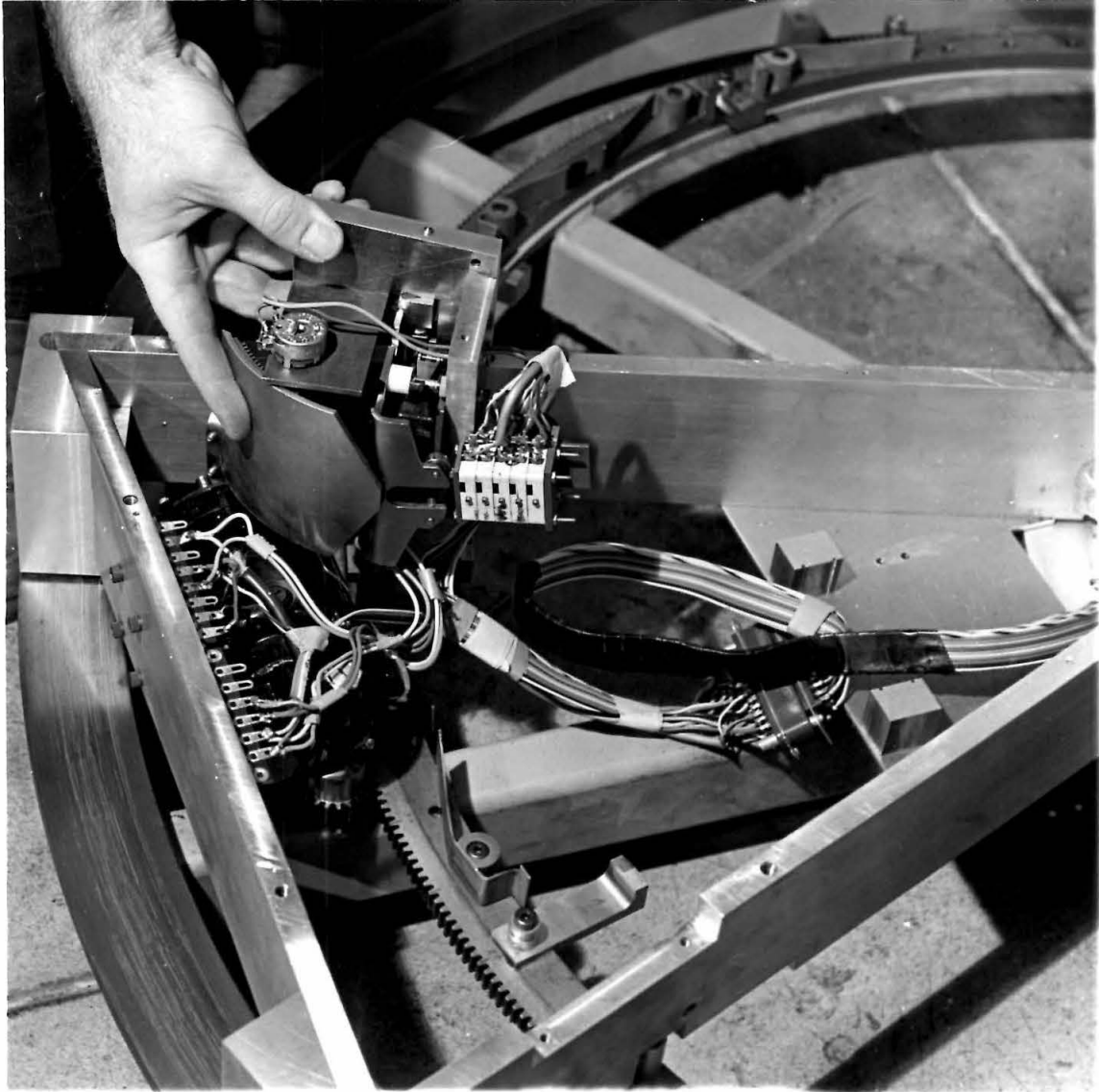


Figure 6: The motorized carriage with the latching device partially removed. The latching yoke, potentiometer and the series of "position" switches are visible. See text for explanations.

Two other mechanisms are also located under the motorized carriage (cf. Fig. 6). The first consists of two push-button switches, one on each side of the carriage. When the proper one is actuated it triggers a latching relay located inside the control panel. The latching relay, in turn, reverses the motor's armature current. This reverses the direction of rotation of the moving system. The second mechanism is a series of four push-button switches. Depending on the angle at which the moving carriage stops, a different switch is actuated. This information is essential in monitoring the operation of the correlation table (cf. Sec. III.4). It is also used in the routing of the coincidence spectra (cf. Sec. III.3).

It should also be mentioned that both carriages were specifically designed to carry the full load of Ge(Li) detectors with their associated liquid nitrogen, cryostat/dewar systems. However, mountings for scintillation counters are also available, as seen in Fig. 4.

The operation of the correlation table will be described next. The reader is frequently referred to Figs. 7 and 8. These figures describe the controls of the system. Several of these controls are also duplicated on the control panel for manual operation.

Electrical power for the system is turned on by pressing the push-button on/off switch (A in Fig. 8), located on the control panel. This switch starts a sequential timer motor (B). This motor first actuates switch No. 1, for continuous supply of AC

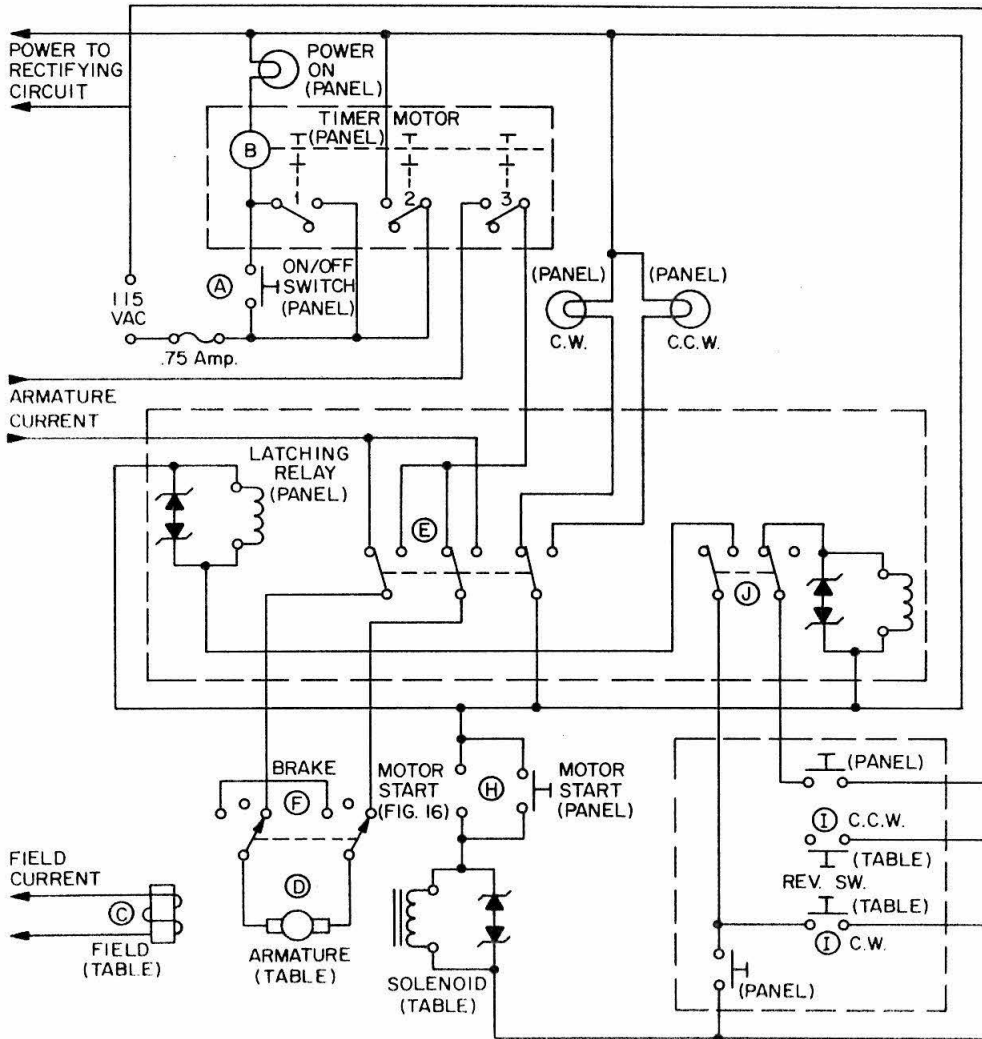


Figure 8

Control circuit for automatic operation of the correlation table.
 For explanations, see text.

power. It then actuates switch No. 2 which supplies power to the rectifying circuit (Fig. 7). At this time, the motors' field-coils (C) are energized but no current is supplied to its armature circuit. Switch 3 is actuated last and supplies current to the armature circuit (D) via contacts (E) on the latching relay. The motor is now turning and the motorized carriage is rotating about the center post. Its rotation speed is set by a potentiometer (P_1 in Fig. 8) on the control panel. As the moving system approaches its intended stopping angle, the latching yoke (cf. Fig. 6) is slowly raised by special guides on the correlation rail (cf. Fig. 4). The yoke in turn, slowly turns potentiometer P_2 (Fig. 5). As a result, the motor's armature current is reduced, and the moving system smoothly slows down. When the intended stopping point is reached, the spring-loaded yoke starts its motion toward the pin on the rail. This actuates the "brake" switch (F) which stops the motor by first opening the armature circuit and then shorting it. The system is set in motion again when the solenoid (G) is actuated. This is done, manually or automatically by closing the power circuit at (H). When the moving system reaches one of its end points, the appropriate reversal switch (I) is actuated. It, in turn, actuates the latching relay at (J), which then reverses the motor's armature current via contacts (E).

III.3 The Dual Slow/Fast Coincidence System

A block diagram of a dual slow/fast coincidence system is shown in Fig. 9. The system shown in the figure utilizes two Ge(Li)

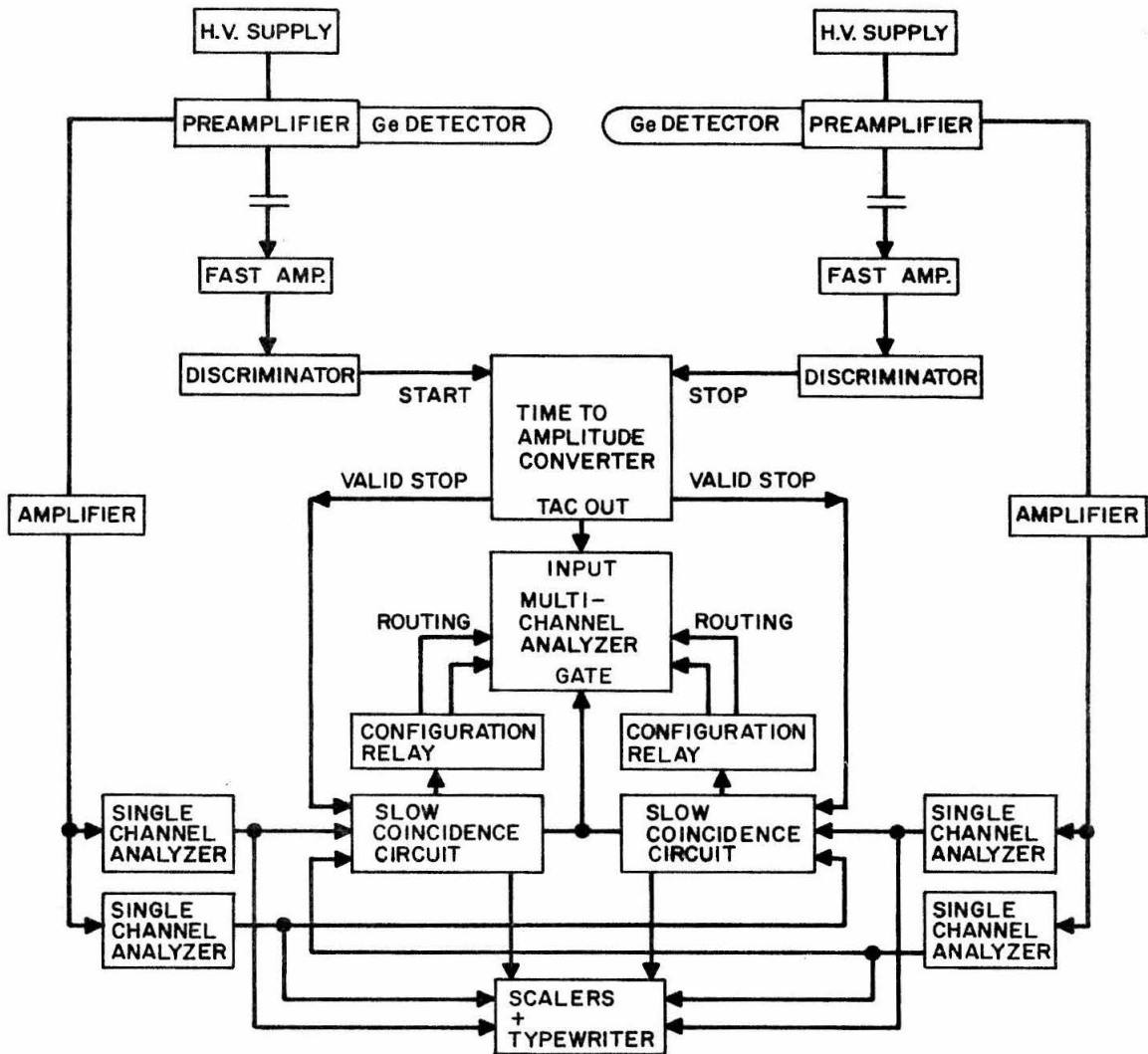


Figure 9

Block diagram of the dual slow/fast coincidence circuit for two Ge(Li) detectors (Sec. III.3).

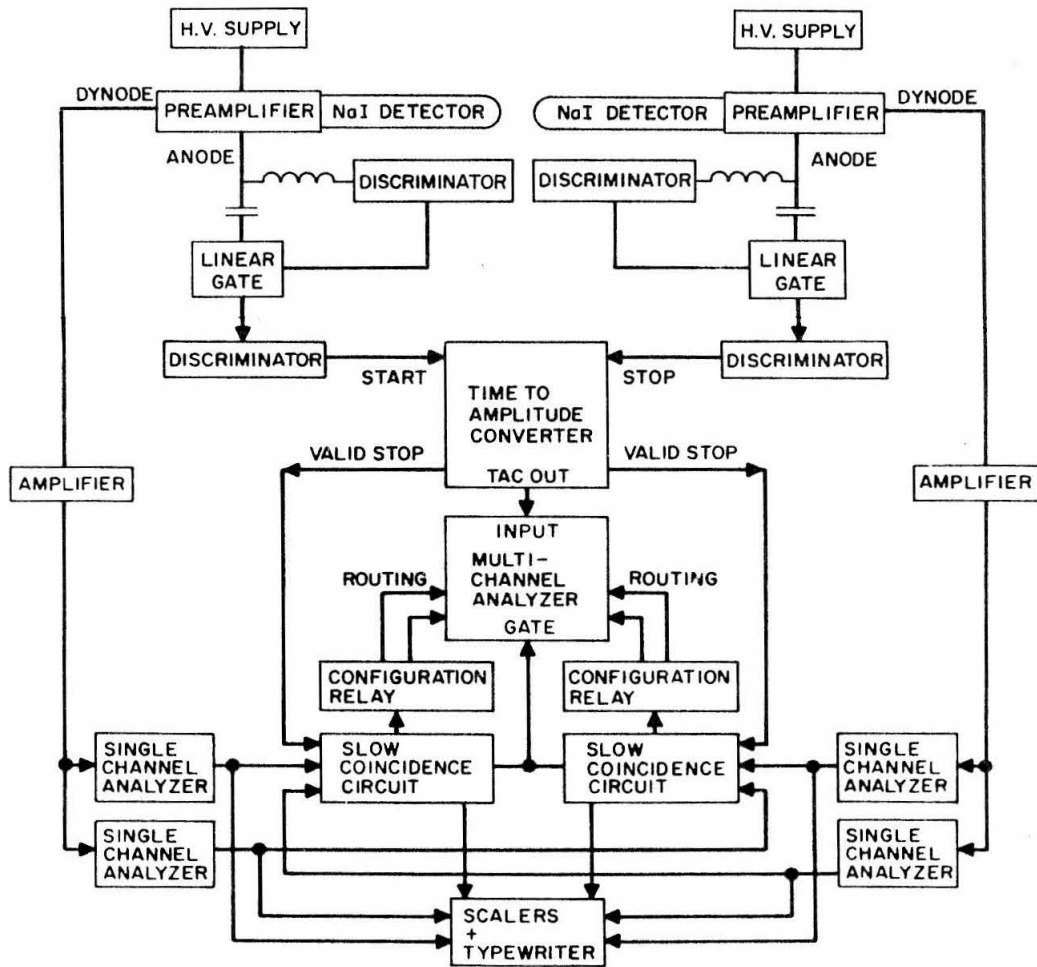


Figure 10

Block diagram of the dual slow/fast coincidence circuit for two scintillation counters.

detectors. A similar system (Fig. 10) was used for scintillation counters. The system consists, basically, of two slow/fast coincidence circuits, coupled to a single time-to-amplitude converter (TAC). The two coincidence circuits operate in parallel independently of one another. Data are stored in appropriate sections of a multichannel analyzer (MCA). A digital routing circuit controls the routing of input data. Also, other data, important for monitoring the operation of the correlation apparatus, are stored in counting scalers and printed out at regular intervals.

A slow/fast coincidence circuit consists of two sections. The 'fast' section is sensitive mainly to time differences between any two gamma rays, detected by the two detectors. There is practically no energy discrimination in this section and therefore no information (except in very special cases) about any particular cascade. This section simply tells us that two gamma rays were detected, one in each detector, with a known delay between them. However, by making the resolving time of this section extremely short, it discriminates against random coincidences. As a result, the majority of coincidences it reports are 'true' ones, belonging to a real cascade although not necessarily to the investigated one. The 'slow' section on the other hand, is energy sensitive. It selects the gamma-ray energies which belong to the cascade under investigation, and rejects all others. It does not discriminate against random coincidences and accepts all gamma rays which satisfy the energy conditions, regardless of their origin. Coupling the two sections together results, therefore, in a system which has a high

efficiency in selecting a particular cascade out of the multitude of gamma rays of different energies and different origins, emitted by a radioactive source.

In Fig. 9, the 'fast' section consists of the following components: two 0.01 μf capacitors, which differentiate the output pulses from the charge-sensitive preamplifiers (ORTEC model 118A). Two fast amplifiers (EG & G model AN 201/N) which amplify and shape the timing pulses. The outputs of two fast discriminators (EG & G model T 105/N) are triggered when their inputs exceed their preset threshold levels, and a TAC (EG & G model TH 200 A/N), which converts the time delay, between its 'start' and 'stop' input pulses, to a proportional voltage pulse. A TAC resolving time of 100 nsec is often used as the 'fast' coincidence requirement. The 'slow' section consists of two linear amplifiers (Canberra model 1416), and two single-channel analyzers (ORTEC model 406A) which select the appropriate gamma-ray energies and reject all others. The use of this 'slow' section, coupled to two higher resolution Ge(Li) detectors makes it possible to investigate particular cascades with radioactive sources, whose energy spectra are highly complex. This was not possible with scintillation spectrometers which have an energy resolution which is an order of magnitude worse than the resolution of Ge(Li) spectrometers. The two 'slow' pulses from the single-channel analyzer, and the 'fast' valid-stop pulse of the TAC output (corresponding to a successful completion of a time-to-amplitude conversion) enter a 'slow' coincidence unit (RIDL model 32-3) with a typical resolving time of 2 μsec .

The time spectrum from the TAC is stored in the MCA which is gated by the triple coincidence output pulses of the coincidence circuit. These pulses are also used to route the time spectrum to different sections of the MCA (corresponding to the different angles in an angular correlation measurement, or to the opposite magnetic field directions in a field reversal measurement).

Since each spectrometer is capable of detecting both gamma rays in the investigated cascade, it is obviously advantageous to use two such coincidence systems, simultaneously. In this case (Figs. 9 and 10) one coincidence system uses γ_1 from detector A and γ_2 from detector B, while the other uses γ_2 from detector A and γ_1 from detector B.

The advantages of such a system are twofold: It increases the counting efficiency of the conventional coincidence system by a factor of 2 since the two coincidence systems operate independently of each other; also, since the roles of the two gamma rays in one coincidence system are reversed in the other, it makes possible the simultaneous observation of the two opposite precessions of the angular correlation pattern in a transverse magnetic field (see Sec. II.5). The TAC time spectrum, stored in the analyzer, is therefore a superposition of two time spectra. It thus results in a flat background (due to random coincidences), on which the two time 'prompts' (for integral measurements) are superimposed. Additional advantages which specifically pertain to integral-rotation measurements, are described in Sec. IV.3. In these measurements which are conventionally performed in two steps (cf. Sec. II.5) it is actually

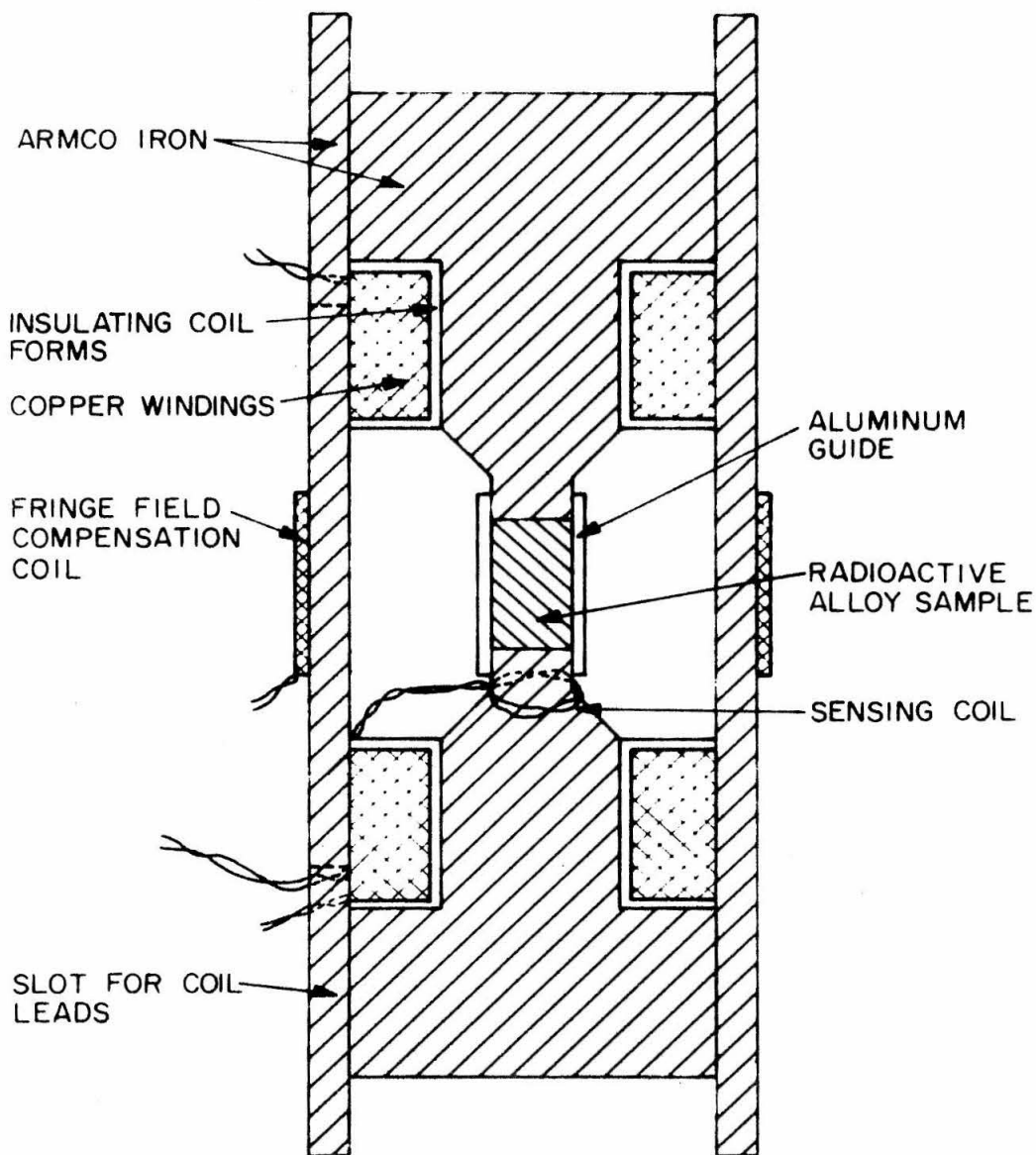
possible to determine the angular correlation coefficients and the mean precession angle, in one step. This is a significant improvement for the usually time-consuming, coincidence experiments.

III.4 Production of External Magnetic Fields

Two types of electromagnets were used in the various experiments.

All measurements of magnetic moments in the osmium region utilized the strong internal magnetic fields of impurities in Fe lattice host. For these cases, the small polarizing field, needed to align the magnetic domains in the host, was supplied by the 'mini-magnet' shown in Fig. 11. This magnet consists of a small, fully enclosed, cylindrically symmetric, electromagnet, having a 'toroidal H' geometry. The coined source is used to complete the continuous flux return path. This magnet design minimizes external fringing fields in the region of the radiation detectors. To further reduce the stray fields, a compensation coil which carries an adjustable fraction of the magnet current is wound on the magnet body. In this way, the stray field due to the magnet can be reduced to less than 10^{-3} G in the region of the detectors. A current of 2 amperes through the magnet coils completely aligns the Fe source. This can be seen in the field saturation curve shown in Fig. 12, taken with a ballistic galvanometer.

All other measurements were performed with a water cooled electromagnet, capable of producing a field greater than 30 kG in a 1 mm pole gap. A diagram of the magnet assembly is given in Fig. 13.



SCALE 2:1

Figure 11

Cross-section of the "toroidal H" magnet used in the measurements on ^{190}Os , ^{192}Os , ^{192}Pt and ^{111}Cd .

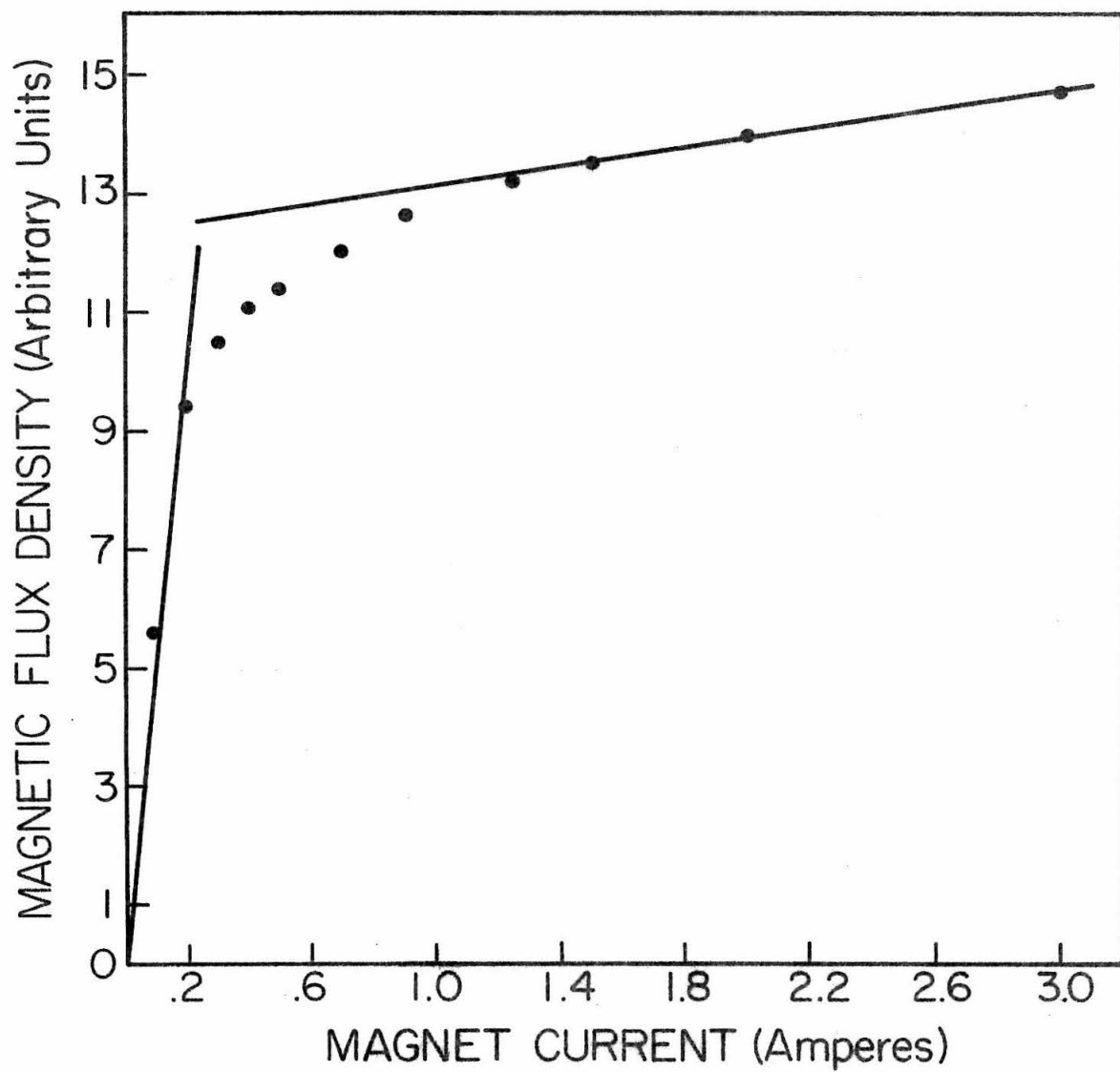


Figure 12

Field saturation curve for a typical ferromagnetic source. Operating current is 3.0 amps. Curve was obtained through the use of a ballistic galvanometer.

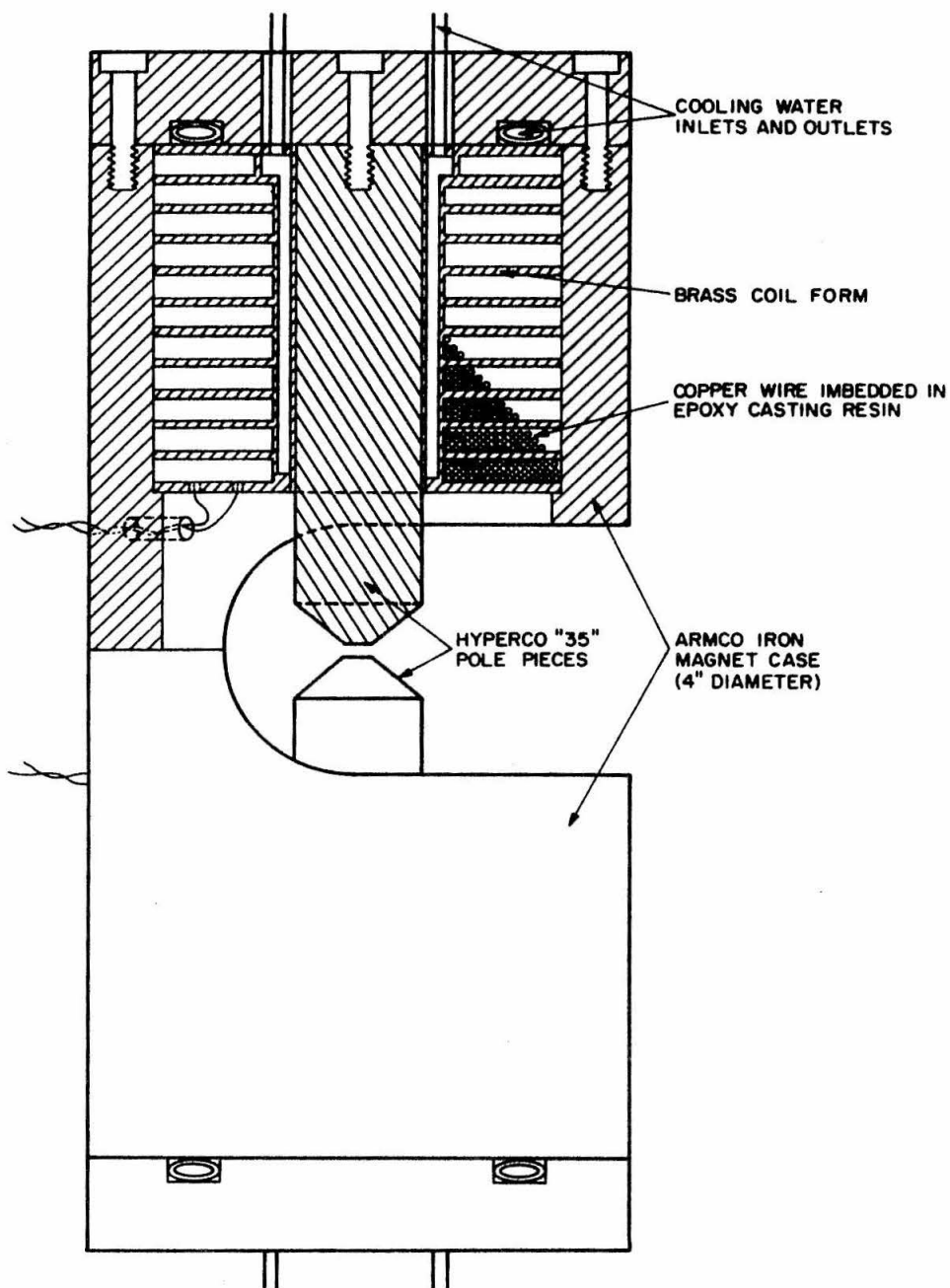


Figure 13

Cutaway view of the high-field electromagnet used in the ^{198}Hg , ^{203}Tl and ^{223}Ra experiments.

The iron magnet body, which serves as a flux return path, was designed to minimize external fringing fields. A current of approximately 20 amperes was drawn from a programmable dc power supply (Sorenson model DCR 60-25). When the magnetic field had to be reversed, the problem of arc suppression, which arises when the current through an inductive load is abruptly changed, had to be dealt with. This was done in several steps: First the small control current of the power supply was shut off bringing down the magnet current. Then the magnet current was reversed through the use of a relay. In the last step, the control current was brought up to its former level restoring the magnet current to its original, but reversed, level. This was done automatically as described in the following section.

III.5 Automatic Operation

The experimental apparatus is controlled by two timing oscillators (Canberra model 1490 C). One enables data accumulation, while the other disables it. These timers are part of a timer/scaler system which also includes six printing scalers (Canberra model 1476) and a teletype scanner (Canberra model 1488) which transmits the information stored in the scalers, to a teletype typewriter.

To start the operation, the 'enable' timer is turned on. Its dc output level changes. A Schmitt trigger, coupled to it, actuates and enables data analysis in the MCA. When performing an angular correlation measurement, data are routed to sections of the

MCA which correspond to appropriate angular positions of the motorized carriage. This is done through the use of a routing circuit shown in Fig. 14. The operation of this circuit is described in the caption to the figure. For a field reversal measurement data are routed through a different circuit described in Fig. 15.

When the data accumulation period is over, several operations take place sequentially: The 'enable' timer turns off. The Schmitt trigger returns to its stable state, blocking further data analysis. The 'disable' timer is turned on. The scanner activates the typewriter which types the information stored in the timer/scaler system during the data accumulation period. For angular correlation measurements it also triggers a monostable multivibrator (shown in Fig. 16) which actuates a relay, closing the power circuit to the solenoid inside the motorized carriage. The solenoid actuates and the motorized carriage rotates to the next angle (see Sec. III.3). For a field reversal measurement, the relay shorts the control circuit of the magnet's power supply. A bistable multivibrator (flip-flop) shown in Fig. 15 is then triggered, actuating two relays. One reverses the magnet current while the other routes the data to a different section of the MCA. The monostable multivibrator then returns to its stable state causing the magnet current to return to its former (but reversed) value. At this time, data accumulation is still blocked.

When the 'disable' interval is over, the 'block' timer turns off. It also turns on the 'enable' timer and data analysis starts again.

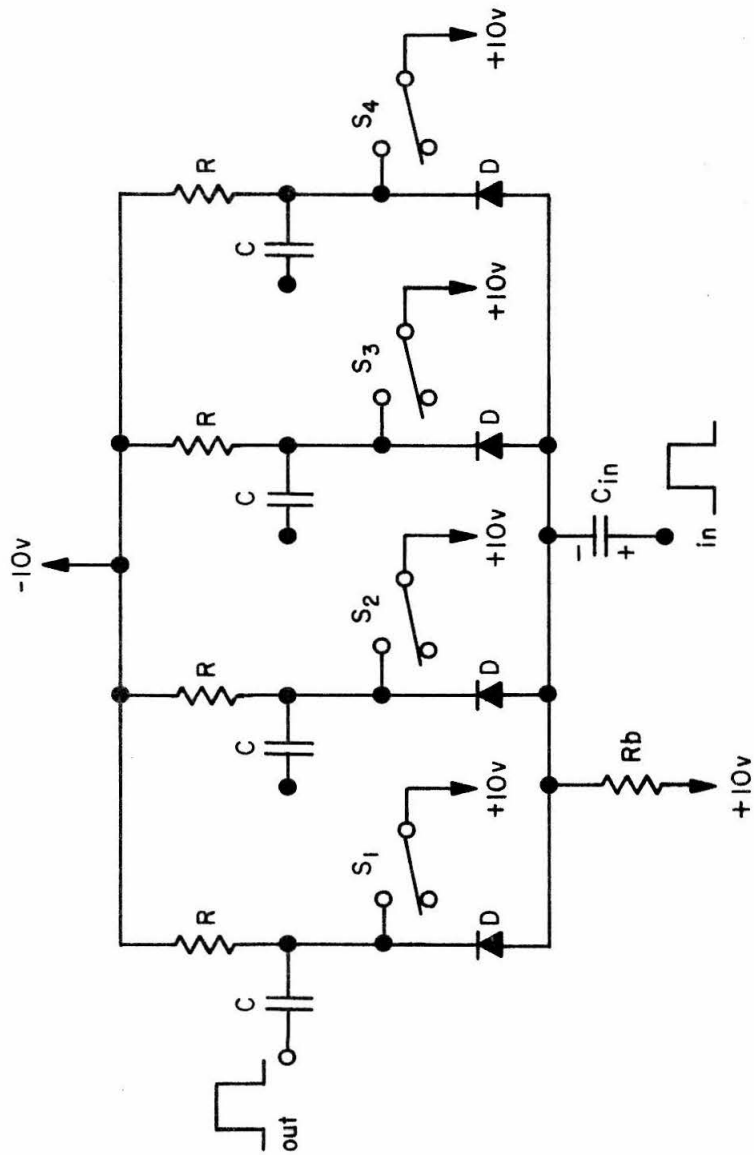


Figure 14: Angular correlation routing circuit, using only passive elements. Switches S_1 through S_4 (normally closed) are located under the motorized carriage (Fig. 6). At different angles, a different switch opens, allowing input pulses to be transmitted to the corresponding output stage. The four output stages are AC coupled to the Ext. Routing inputs of the MCA.

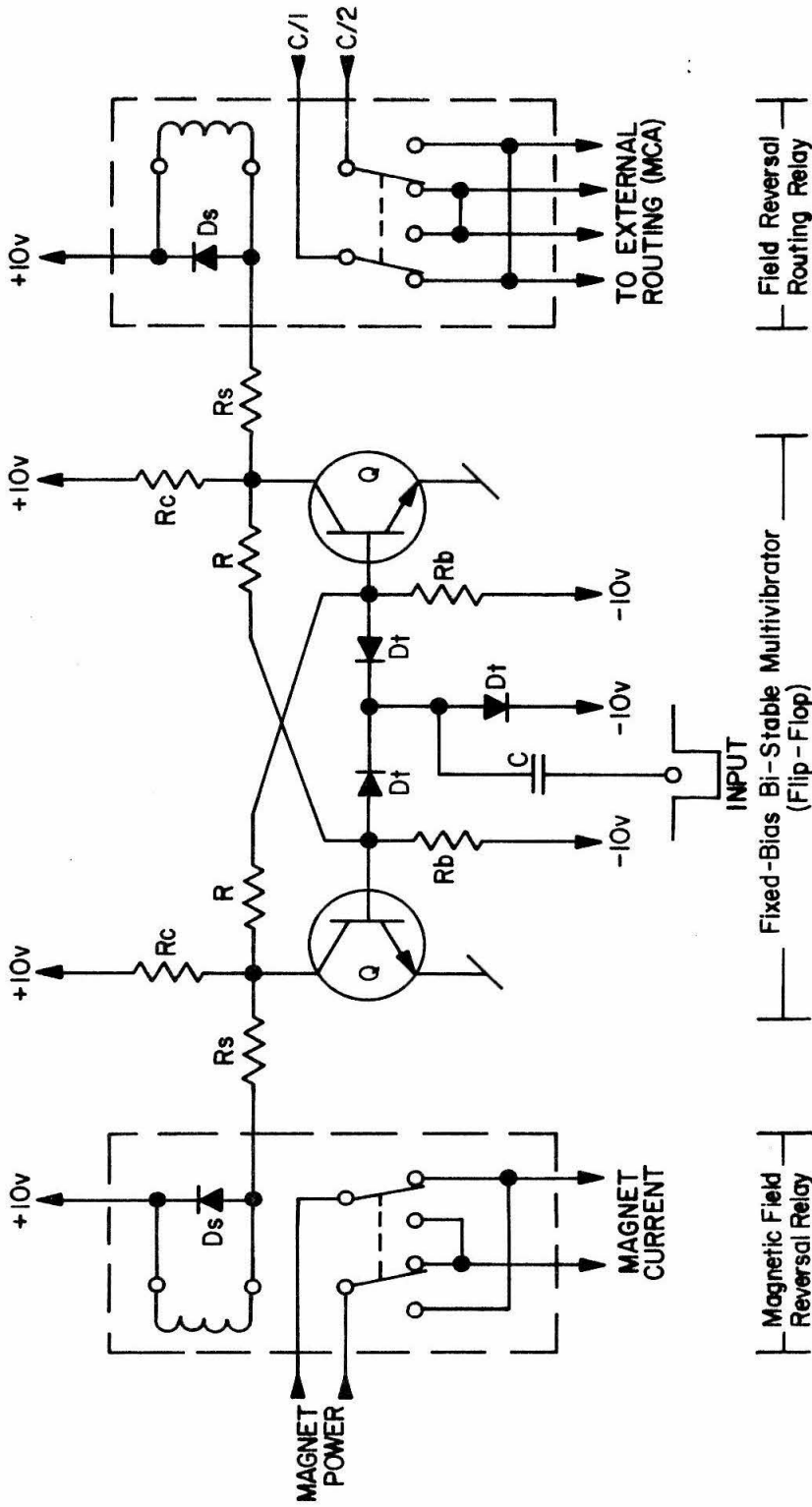


Figure 15: Field-reversal routing circuit utilizing a fixed bias bi-stable multivibrator with symmetrical triggering. Magnet current is reduced before the reversal relay is actuated. C/1 and C/2 refer to the triple coincidence outputs from the two coincidence circuits shown in Figures 9 and 10.

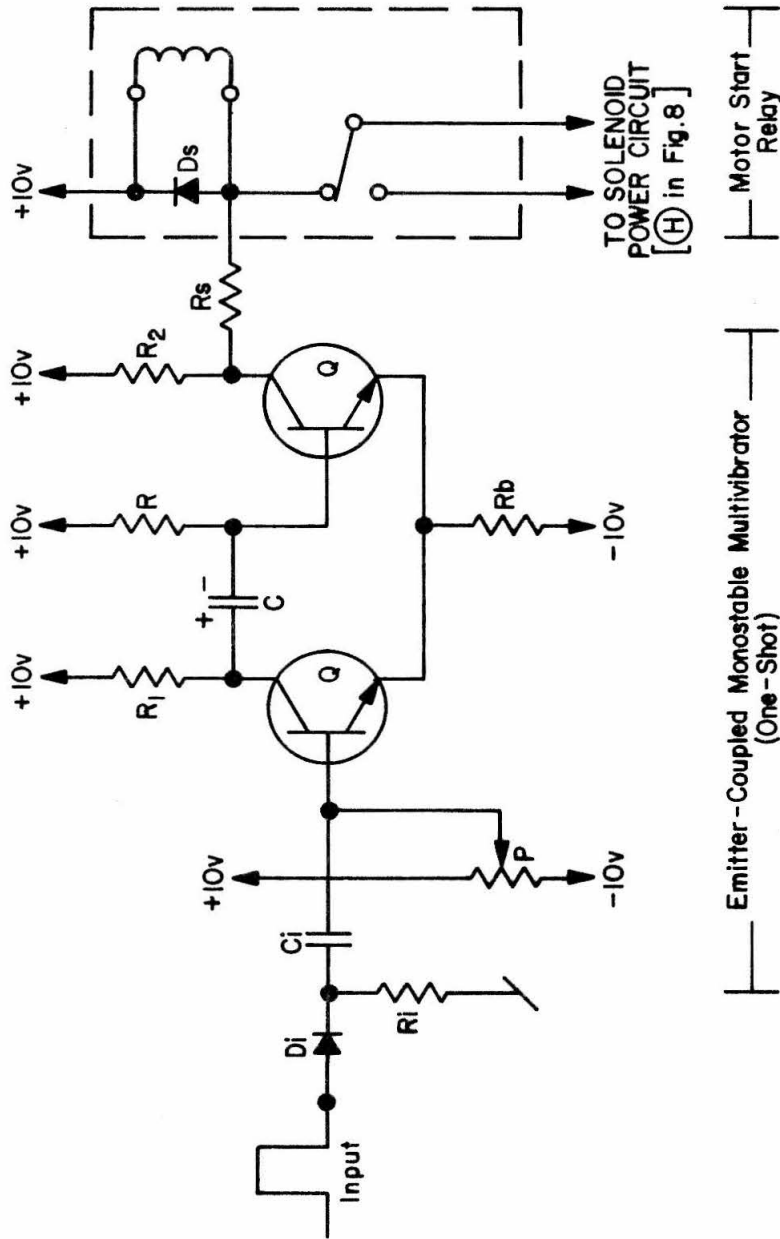


Figure 16: A monostable multivibrator used to start rotation of the motorized carriage. The time during which it is in its unstable state is easily adjusted through potentiometer P. In a field-reversal measurement, the relay shorts the control circuit of the magnet power-supply (not shown), reducing the magnet current.

This operation keeps going until stopped manually.

III.6 Experimental Procedure

Before starting any measurement, the system goes through several tests and calibrations. These include linearity checks of the TAC and the MCA, calibration of the time scale displayed by the MCA, and determination of the system's resolving time for the appropriate energies. Linearity checks are usually performed with random coincidences and the TAC time spectrum displayed in the MCA, should be flat. The time scale and resolving time calibrations are performed using annihilation radiation, together with introduction of known delays into the coincidence circuits. Operation of this circuit is also checked with an oscilloscope.

The radioactive source is then placed in the center of the correlation table facing the two detectors. An energy spectrum from one spectrometer is stored in the MCA and the two single channel analyzers coupled to this detector are adjusted to accept the two gamma rays in the investigated cascade and reject all others. This procedure is repeated for the other detector. Care must be exercised to insure that γ_1 from detector A and γ_2 from detector B are coupled to one coincidence circuit, while γ_2 from detector A and γ_1 from detector B are coupled to the other. The 'fast' sections are adjusted next. First, the threshold levels of the fast discriminators are adjusted to discriminate against electronic "noise", and achieve the best time resolution available. This is found to be, in most cases, just above the "noise". The resolving time of the TAC

is then set to the desired value. In the last step the 'slow' coincidence units are adjusted for the appropriate resolving time and for maximum overlap of the three input pulses. The apparatus is now ready for operation (it may be necessary to repeat the calibration checks for possible changes due to the above-mentioned adjustments).

When performing angular correlation measurements, centering of the source has become absolutely crucial. Since, in many cases, the investigated cascade has a small anisotropy, source decentering effects can completely distort the angular correlation pattern. Therefore, the system is first allowed to run through several cycles and the source is centered to better than 1 percent by observing the 'singles' count rates in the single channel analyzers, coupled to motorized detectors system, at different angles. The information printed out by the typewriter at regular intervals is then used to correct for the remaining decentering of the source. Other effects due to source thickness are described in Appendix B.

The angular correlation measurement now takes place. Data accumulation period at each angle is usually set to less than 10 minutes (usually 3 minutes). This is, in most cases, an appropriate period since then: (i) the radioactive decay of the source has negligible effect; (ii) high frequency interference due to fluctuations in power lines, voltage levels, temperature, etc., are averaged out; (iii) low frequency interference due to similar fluctuations have negligible effects. The data printed out by the time/scaler system, are checked periodically for any unusual

results which would indicate malfunctions in the operation of the system. These data include the coincidence rate and the 'singles' rates in each of the coincidence circuits. The operation of the correlation table is also monitored by gating off different scalers at different angles for angular correlation measured, or at different directions of the magnetic field in a field reversal measurement.

Data are read out and analyzed daily. The different sets of data are compared for internal consistency, and all data sets in which malfunctions are detected are discarded. When measuring several different sources of the same radioactivity (such as a liquid source and the different ferromagnetic sources), the measurements are performed in identical experimental set-ups, to allow determination of possible effects due to the different compositions of the various sources.

When using the integral-reverse-field method, the angular correlation of the investigated cascade is first measured. The angle θ at which this distribution reaches its maximum logarithmic slope is determined. Then the field reversal measurement is performed with the movable detector fixed at that angle. This measurement is repeated at the mirror angle $2\pi-\theta$ and the change in the sign of the field-reversal ratio $R(\theta)$ is observed. For an integral rotation measurement, the angular correlation is measured once without an applied magnetic field, and then with an applied field. The mean precession angle is then derived directly. The use of our dual-integral-rotation technique enables the determination of the mean precession angle in one step by measuring the angular correlation with

an applied magnetic field, and observing the two oppositely precessed angular distributions.

PART 2: MAGNETIC MOMENT MEASUREMENTS IN THE OSMIUM REGION

The nuclei of osmium and platinum are members of a transition region in which the shape of the nuclear surface turns from deformed to spherical. Nuclei in this region are therefore particularly suited for a critical test of nuclear models. Also, in this region it has been predicted that the nuclear surface switches abruptly from prolate to oblate shape before becoming spherical. Neither the rotational model nor the vibrational model, are capable of quantitative description of nuclear properties in this region, being "deformed" or "spherical" oriented models. A model which treats the nucleon-pairing and the quadrupole surface forces on the same footing has recently been put forward by Kumar and Baranger¹⁾. This model was found to be in good agreement with many experimental results.

The experiments described below were undertaken in order to furnish more data on nuclei in this important region and to resolve discrepancies in existing results.

IV. THE MAGNETIC MOMENTS OF THE FIRST 2^+ AND 4^+ STATES IN ^{190}Os .

IV.1 Introduction

The magnetic moment of the first 2^+ state, at 186.7 keV, in ^{190}Os has been measured before by Goldring and Gilad et al.^(2,3), who observed the precession of the Coulomb excited 2^+ state in an external magnetic field. Their result $\mu = 0.56 \pm 0.06$ nm was recently re-evaluated to $\mu_{2^+}(^{190}\text{Os}) = 1.10 \pm 0.17$ nm due to lifetime correction⁽⁴⁾. This last result is in disagreement with all other collective magnetic moments in this region, as well as with recent calculation based on collective models.

The magnetic moment of the first 4^+ state, at 547.9 keV, has never been measured. However, if both the 2^+ and 4^+ state are of purely collective character, the ratio of their magnetic moments should equal the ratio of their spins, i.e., $\mu_{4^+} = 2\mu_{2^+}$. Measurements on these states would then test the applicability of existing collective models to low-lying states in this region.

IV.2 Source Preparation

In order to obtain a sufficiently large mean precession angle during the short lifetime of the investigated nuclear state, the strong hyperfine magnetic field experienced by source nuclei embedded in a host Fe lattice was utilized.

^{190}Ir activity was obtained by bombarding highly enriched ^{190}Os isotope with 15 MeV protons at the Oak Ridge cyclotron producing a high specific activity source via the reaction $^{190}\text{Os}(p,n)^{190}\text{Ir}$. Chemical separation of Ir from Os was not attempted. About 30 mg of

the active Ir-Os alloy was deposited in a pot made of 1300 mg of pure (99.99 percent) Fe. The pot was sealed with a tapered Fe pin and then melted for 15 minutes in an induction furnace using a levitating Ag boat. The sample was cut into small pieces and the activity of each piece was measured. It was found that the activities of the small samples were proportional to their weights, thus ensuring uniform distribution of activity in the Fe host, and resulting in a 0.5 at. percent dilute solution. The samples were then remelted for an additional 15 minutes, coined into a cylindrical shape and placed between the pole-tips of a small, fully enclosed, toroidal electromagnet (cf. Sec. II.5). A field saturation curve was run for each source with the help of a ballistic galvanometer, and the magnet subsequently operated at twice the saturation current. The sources were also annealed, but no measurable differences in the internal magnetic field were observed.

IV.3 The 2^+ State

The measurement of the magnetic moment of the 2^+ state was performed with two Ge(Li) detectors. From the level diagram of ^{190}Os shown in Fig. 1, it is seen that three strong cascades; the $4^+(361 \text{ keV})2^+(187 \text{ keV})0^+$, the $2^+(371 \text{ keV})2^+(187 \text{ keV})0^+$, and the $3^+(569 \text{ keV})2^+(187 \text{ keV})0^+$ cascades can be used in the measurement. The energy spectrum of ^{190}Os taken with a Ge(Li) spectrometer is shown in Fig. 2. Clearly, the $3^+(569 \text{ keV})2^+(187 \text{ keV})0^+$ cascade is the most favorable one, having a minimum of interference from other cascades.

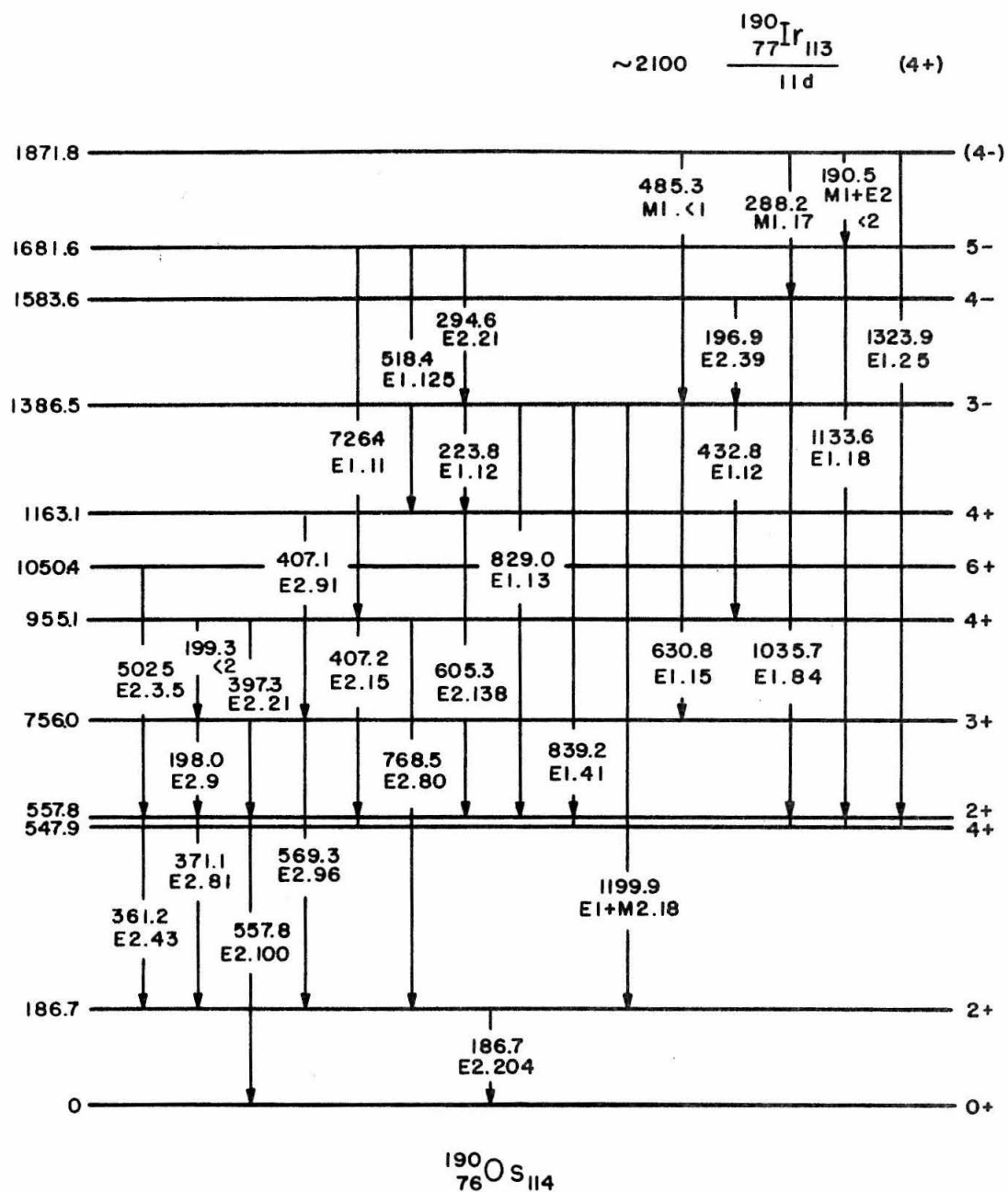


Figure 1

Level diagram of ^{190}Os (proposed by Yamazaki et al.⁽⁶⁾).

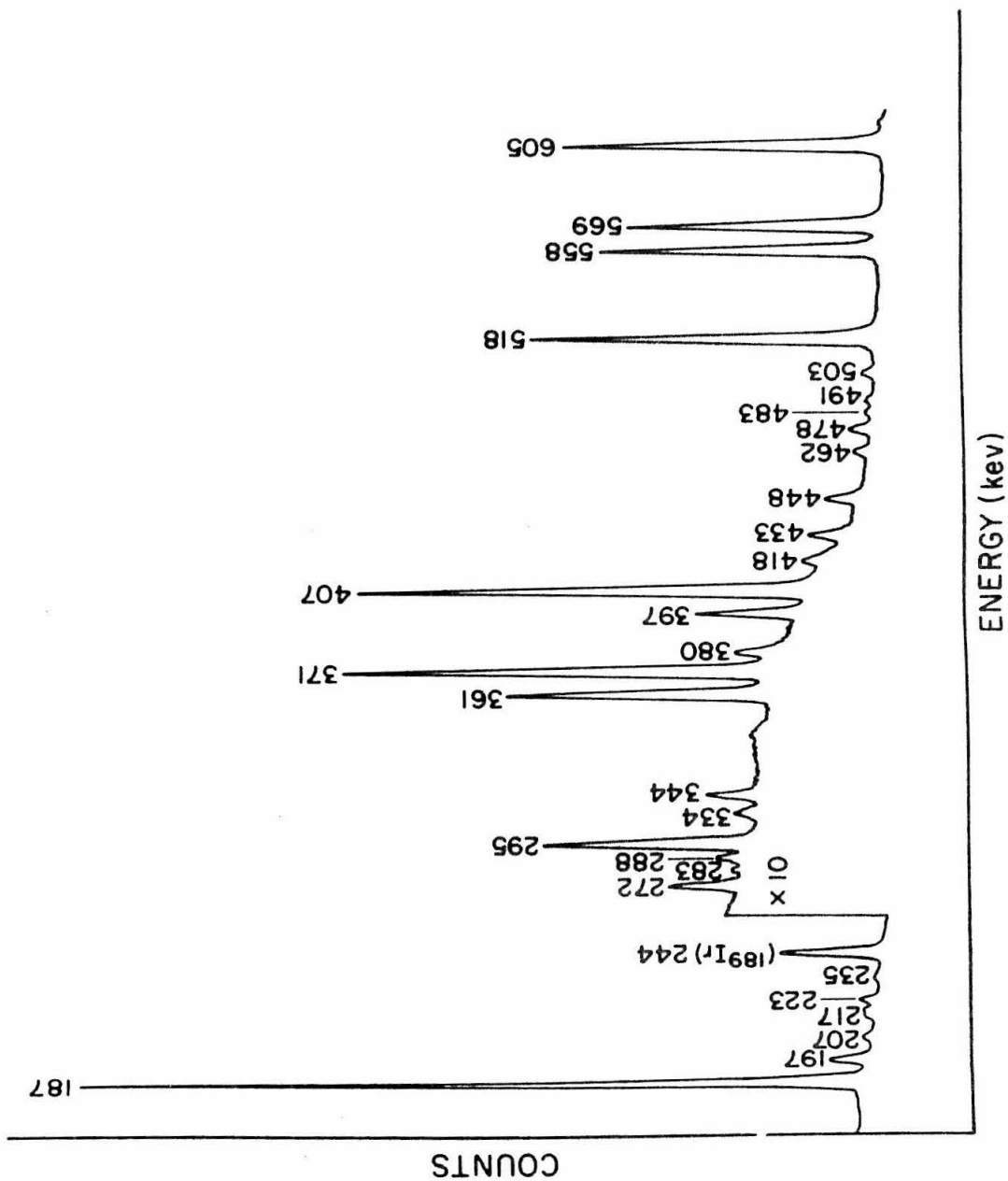


Figure 2a

Ge(Li) energy spectrum of ^{190}Ir decay. (a) Energies from 170 keV to 620 keV.

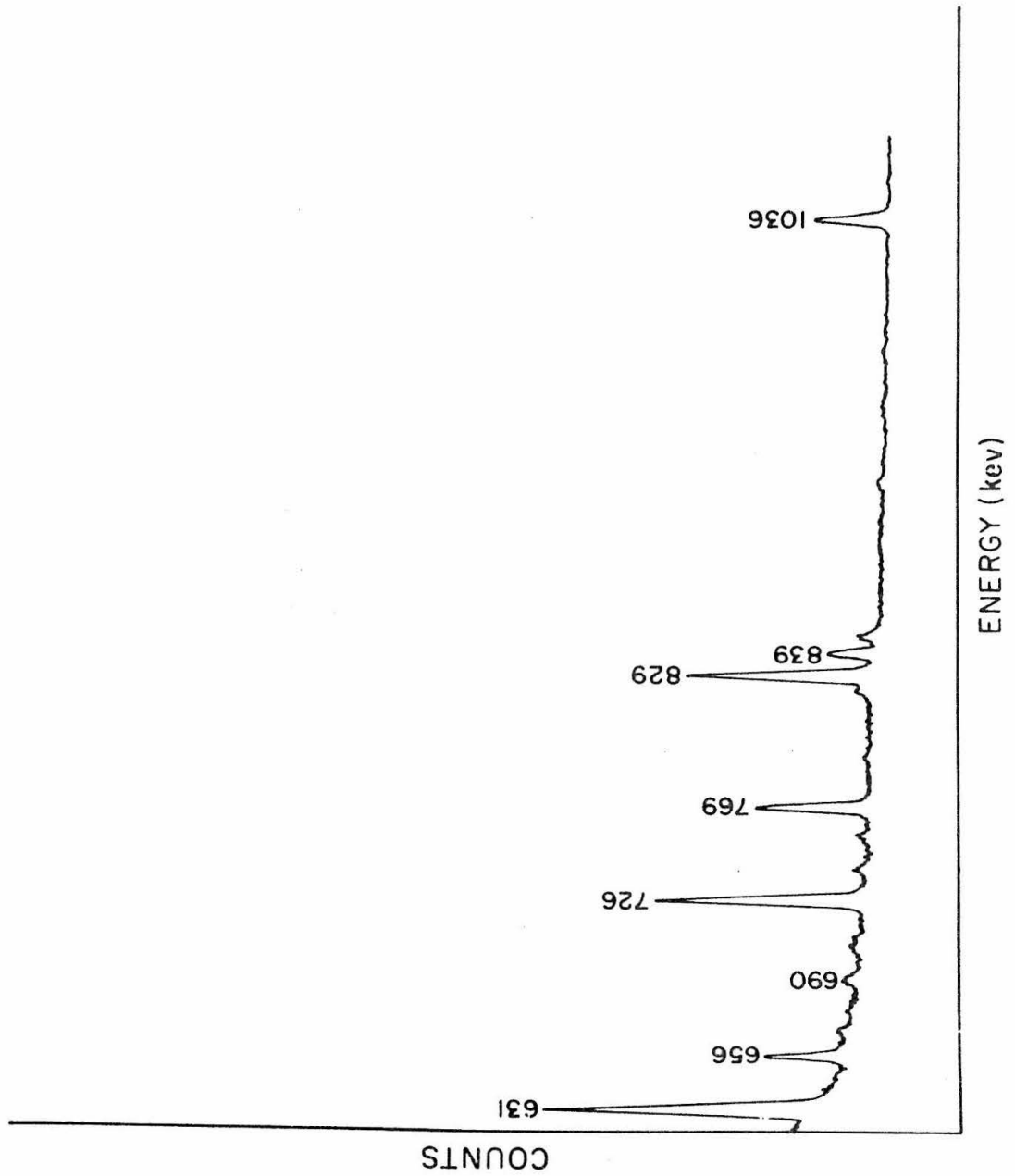


Figure 2b

Ge(Li) energy spectrum of ^{190}Ir decay. (b) Energies above 620 keV.

Since the mean precession angle of the magnetic moment of this state, in the internal magnetic field of the Fe host, was expected to be large ($\omega_T \simeq 1$), the integral-rotation method (cf. Sec. II.5) in which the precession of the angular correlation pattern is observed directly, was used.

In observing the two opposite precessions simultaneously, as described in Sec. III.3, with the magnetic field in one direction only, we were able to derive the angular correlation coefficients together with the mean precession angle. This dual-integral rotation method has the additional advantage of eliminating systematic errors such as detector misalignment and source decay. Figure 3a shows time coincidence spectra obtained in the measurement of the angular correlation for the $3^+(569 \text{ keV})2^+(187 \text{ keV})0^+$ cascade. In Fig. 3b we see the time spectra for the same angular distribution, measured in the presence of an external aligning magnetic field. The opposite precessions of the angular correlation pattern in the two coincidence systems are clearly displayed. Figure 4 shows the observed angular distribution with, and without an applied magnetic field, together with the attenuated angular distribution obtained by adding up the two oppositely precessed angular distributions. This distribution simulates the case in which the detector cannot distinguish between the two radiations in the cascade. A non-linear least-squares fitting program was used in simultaneously fitting both distributions using the expression (Sec. II.3):

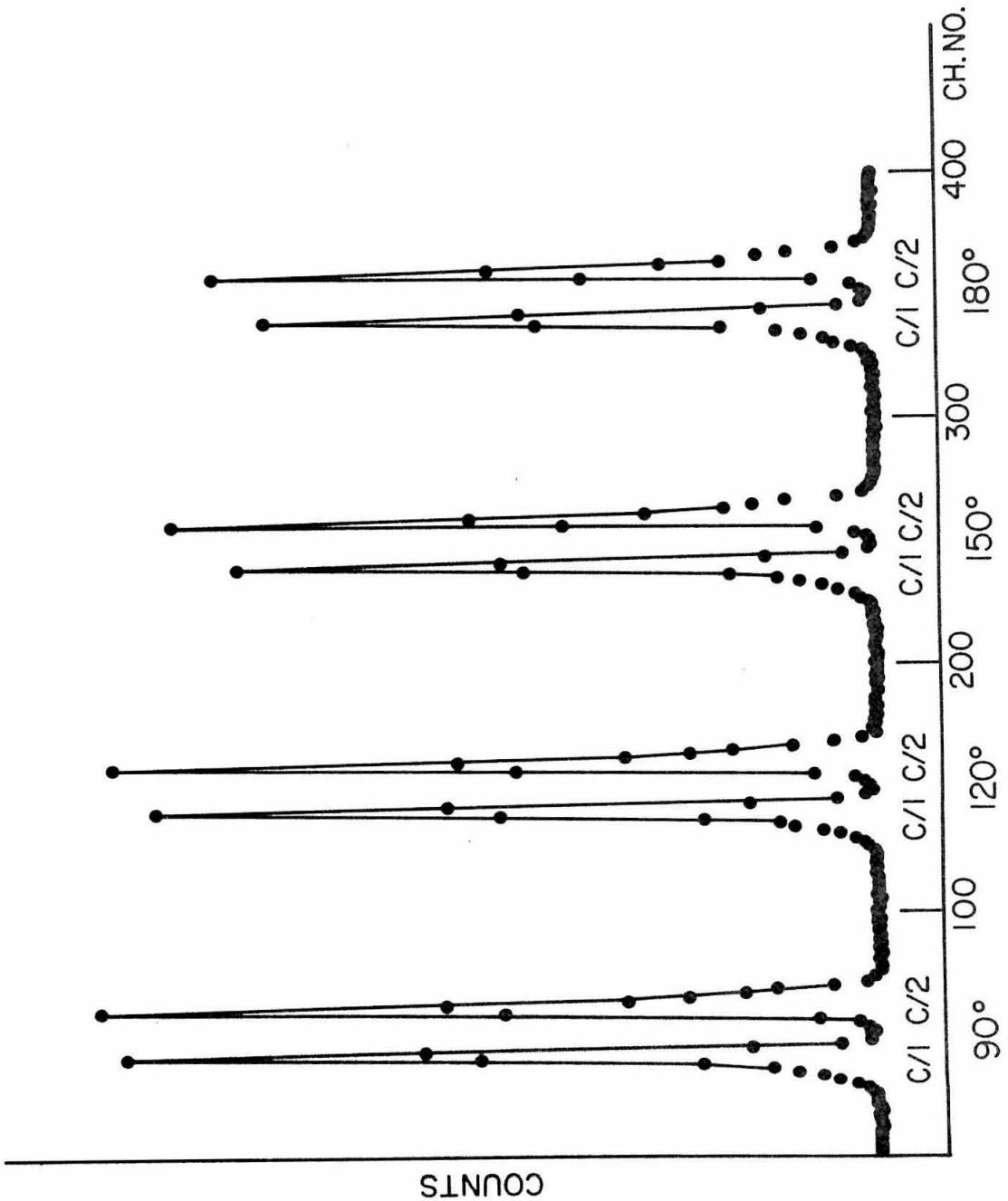


Figure 3a: Time spectra in ^{190}Os . Time "prompts" are due to the two coincidence circuits C/1 and C/2. Angles refer to angular separation of the two detectors.

(a) Angular distribution without an aligning magnetic field.

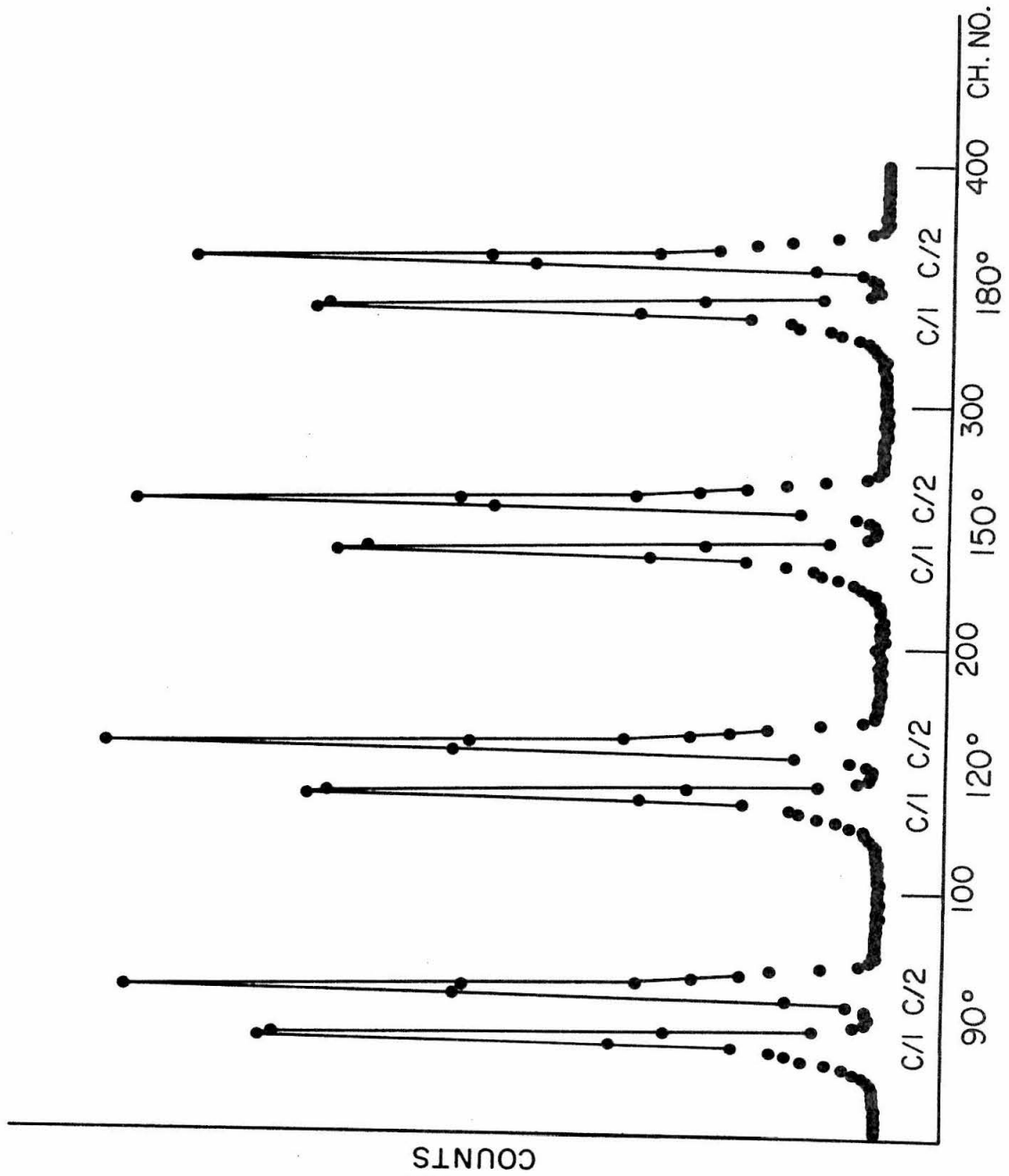


Figure 3b: Time spectra in ^{190}Os , stored in quarters of the MCA. Same as Figure 3a. (b) Angular distribution with the source aligned by an external magnetic field.

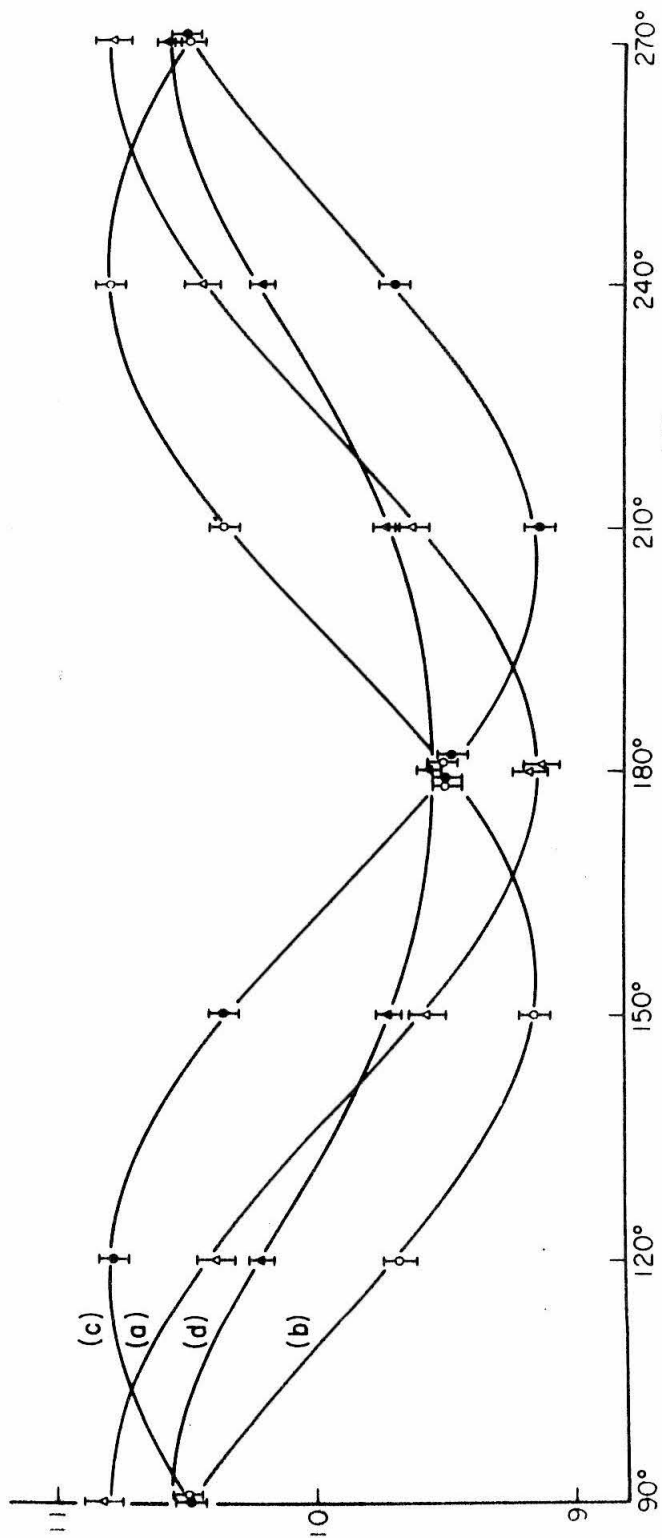


Figure 4: Angular correlation of the 3^+ (569 keV) 2^+ (187 keV) 0^+ cascade in ^{190}Os .

(a) Without an external aligning magnetic field. (b) With an aligning field; C/1 only. (c) With an aligning field; C/2 only. (d) Attenuated correlation obtained by summing curves (b) and (c). Curves (b) and (c) were obtained simultaneously from the data shown in Figure 3b.

$$W(\theta, H) = 1 + \frac{b_2}{[1 + (2\omega\tau)^2]^{1/2}} \cos [2\theta - \arctan (2\omega\tau)] \\ + \frac{b_4}{[1 + (4\omega\tau)^2]^{1/2}} \cos [4\theta - \arctan (4\omega\tau)].$$

The results are: $b_2 = -0.13 \pm 0.05$, $b_4 = -0.008 \pm 0.006$, and $\omega\tau = 0.65 \pm 0.05$. Using the internal magnetic field $H = -1.43 \times 10^6$ Oe and the mean life of the 2^+ state $\tau = 3.46 \times 10^{-10}$, both taken from the compilation of Ref. 4, we get $\mu_{2^+}({}^{190}\text{Os}) = 0.54 \pm 0.06$ nm.

IV.4 The 4^+ State

The magnetic moment of the first 4^+ state, at 547.9 keV, in ${}^{190}\text{Os}$ was measured with two 7.6 cm x 7.6 cm NaI(Tl) detectors. Two cascades were investigated: the $3^-(839 \text{ keV})4^+(361 \text{ keV})2^+$ cascade displayed a small negative anisotropy and therefore was not used in the precession measurements. The $4^-(1030 \text{ keV})4^+(361 \text{ keV})2^+$ cascade showed a positive anisotropy with angular correlation coefficients (uncorrected for geometry) $A_2 = +0.068 \pm 0.007$ and $A_4 = +0.01 \pm 0.04$. This result is inconsistent with the spin $I = 3$ previously proposed for the 1584 keV state⁽⁵⁾, however, it is in agreement with recent results of Yamazaki et al.⁽⁶⁾, who assigned $I^\pi = 4^-$ for the 1584 keV state.

The mean precession angle of the magnetic moment of this 4^+ state in the internal magnetic field of the Fe host was measured using the integral-reverse field method (Sec. II.5). From the angular correlation measurement, a maximum magnitude of field

reversal ratio $R(\theta)$ was inferred at $\theta = \pm 3\pi/4$ radians. The weighted average value of the measurements at $+ 3\pi/4$ and $- 3\pi/4$ radians was $R(\theta = 3\pi/4) = (0.60 \pm 0.12) \times 10^{-2}$ from which the corresponding mean precession angle was found to be $\omega\tau = 0.060 \pm 0.014$ radians. The mean life of the 4^+ state is $\tau = (4 \pm 2) \times 10^{-11} \text{sec}^{(7)}$ and consequently, the magnetic moment of this state was found to be $\mu_{4^+}({}^{190}\text{Os}) = 0.88 \pm 0.48$. The large uncertainty is mainly due to the uncertainty in the lifetime.

V. THE MAGNETIC MOMENT OF THE FIRST 2^+ STATE IN ^{192}Os

V.1 Introduction

Several measurements of the magnetic moment of the first 2^+ state, at 206 keV, in ^{192}Os have been reported. Keszthelyi et al.⁽⁸⁾ using the gamma-gamma perturbed angular correlation technique, and the internal magnetic field of osmium in iron, obtain $\mu_{2^+}(^{190}\text{Os}) \simeq 0.24$ nm. Pramila and Grodzins⁽⁹⁾, using the same technique reported $\mu_{2^+} = 0.24 \pm 0.06$ nm which was later revised upwards to $\mu_{2^+} = 0.40 \pm 0.06$ nm⁽¹⁰⁾. Goldring et al.⁽²⁾ and Gilad et al.⁽³⁾, precessing the magnetic moment of the Coulomb excited 2^+ state in an external magnetic field, reported $\mu_{2^+} = 0.60 \pm 0.08$. However, their result was based on a half-life value of this state which is almost twice the presently adopted value $T_{1/2} = 2.10 \times 10^{-10}$ sec. Consequently, their recalculated value is $\mu_{2^+}(^{192}\text{Os}) = 1.0 \pm 0.14$ ⁽⁴⁾.

The measurements described above have all encountered difficulties in data analysis. The gamma-gamma correlation measurements were all performed with two NaI spectrometers. From the level diagrams of ^{192}Os and ^{192}Pt shown in Fig. 5, and from the Ge(Li) and NaI energy spectrum of the decay of ^{192}Ir shown in Fig. 6 and Fig. 7, it is seen that the following cascades interfere with the measured $3^+(484 \text{ keV})2^+(206 \text{ keV})0^+$ cascade: $4^+(468 \text{ keV})2^+(316 \text{ keV})0^+$, $3^+(604 \text{ keV})2^+(316 \text{ keV})0^+$, $3^+(612 \text{ keV})2^+(308 \text{ keV})0^+$, $4^+(589 \text{ keV})2^+(206 \text{ keV})2^+$, and $4^+(589 \text{ keV})2^+(396 \text{ keV})2^+(316 \text{ keV})0^+$ all in ^{192}Pt , and the $3^+(201 \text{ keV})2^+(489 \text{ keV})0^+$ in ^{192}Os . The poor

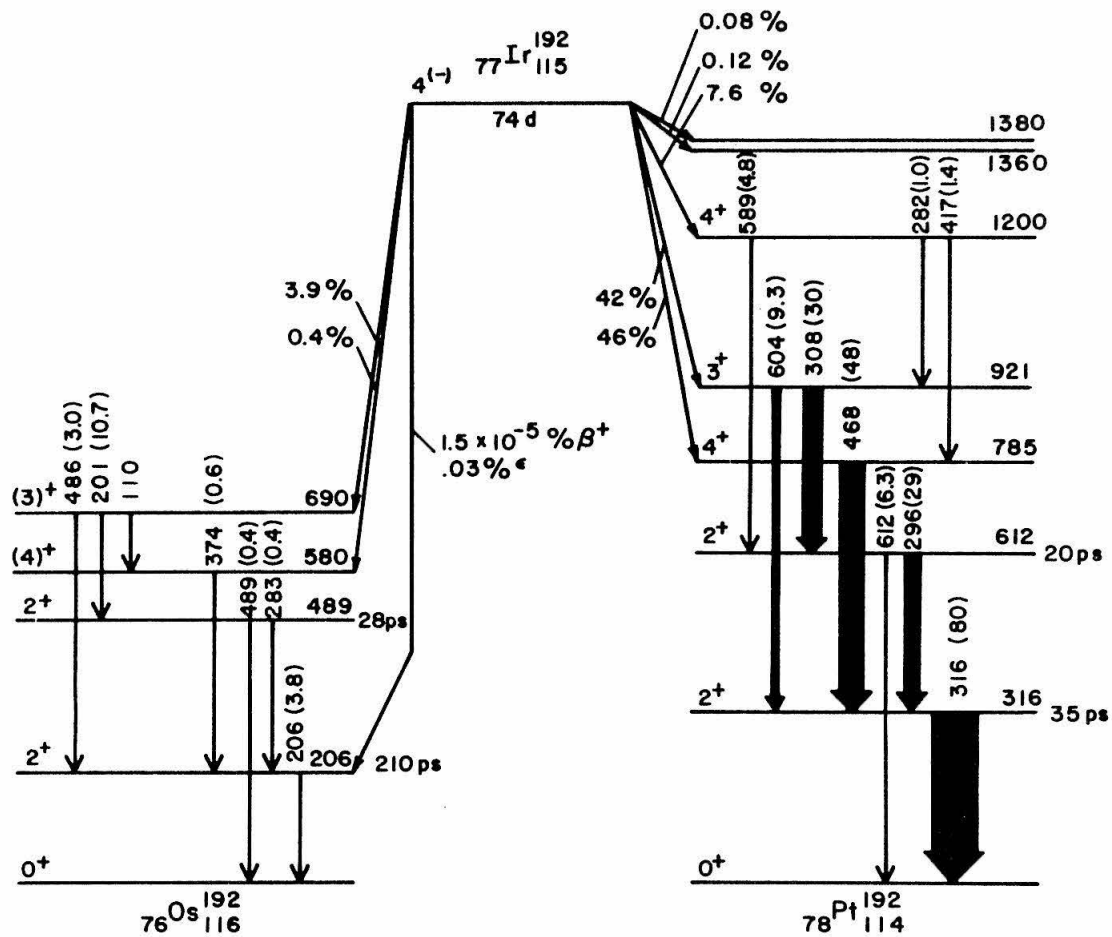
Decay Scheme of Ir¹⁹²

Figure 5

The decay scheme of ^{192}Ir . Intensities are shown in parentheses.

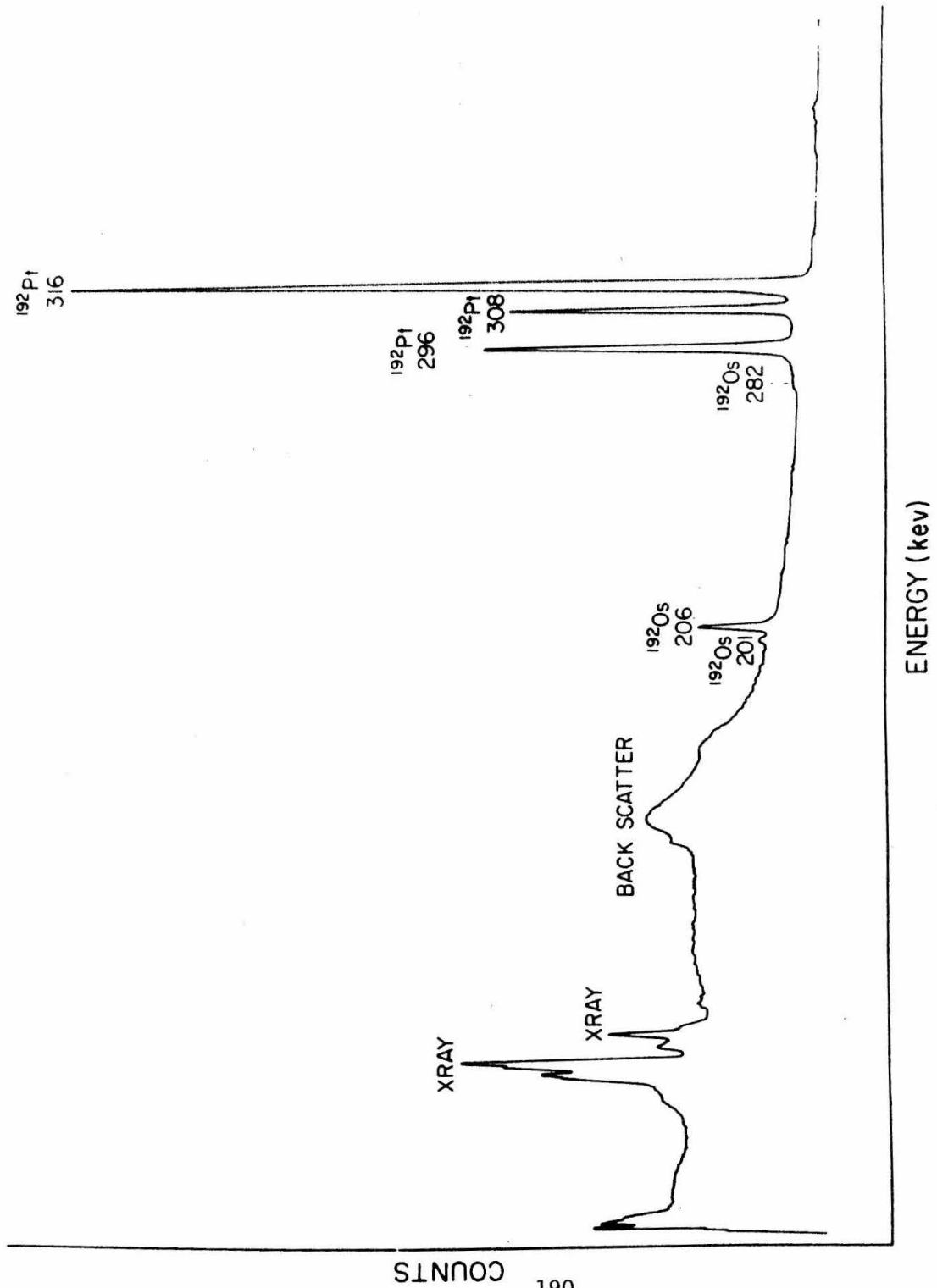


Figure 6a: Ge(Li) energy spectrum of ^{190}Ir decay.
 (a) Energies below 400 keV.

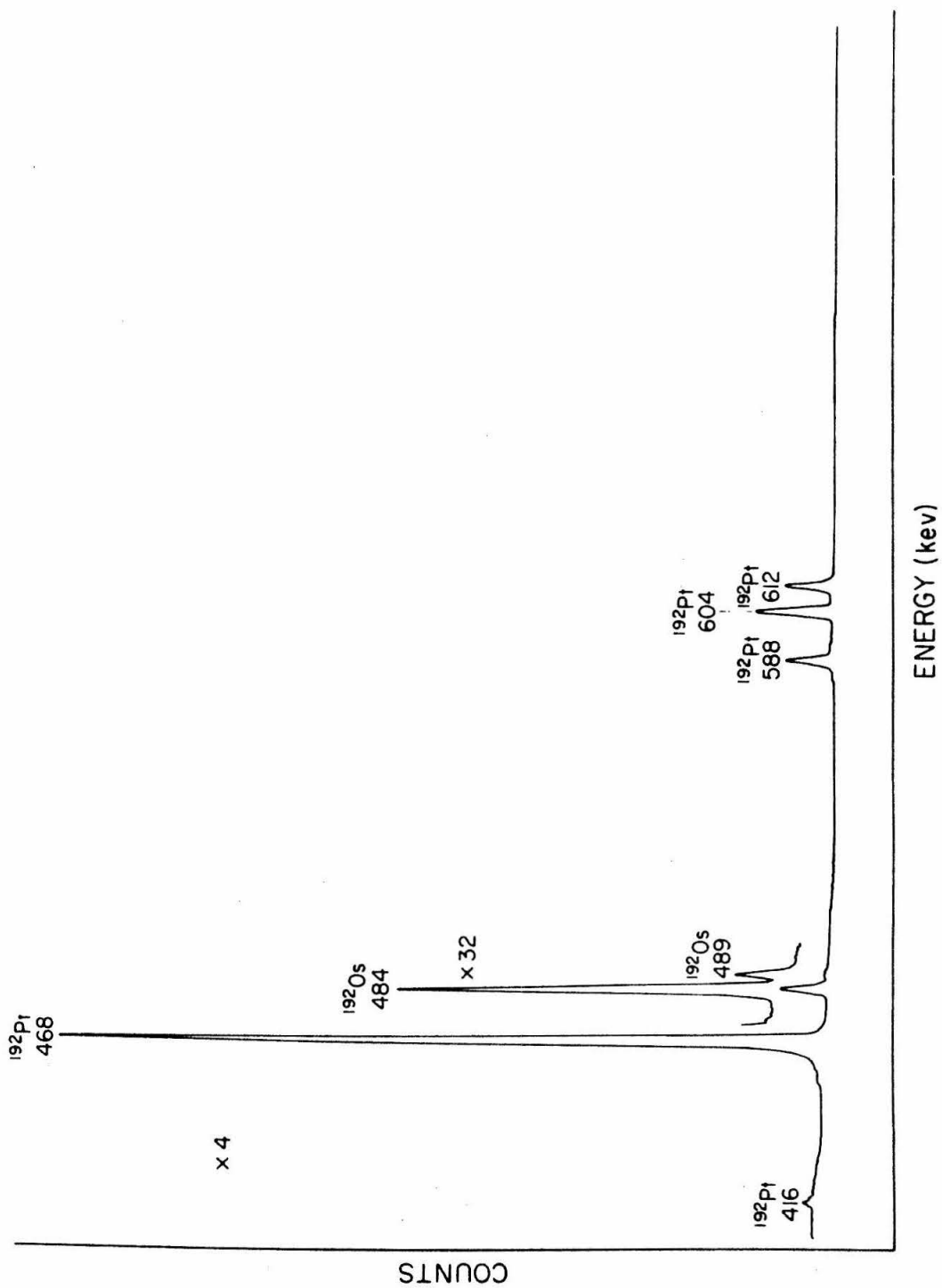


Figure 6b: Ge(Li) energy spectrum of ^{192}Ir decay.

(b) Energies above 400 keV (scale x4 relative to (a)).

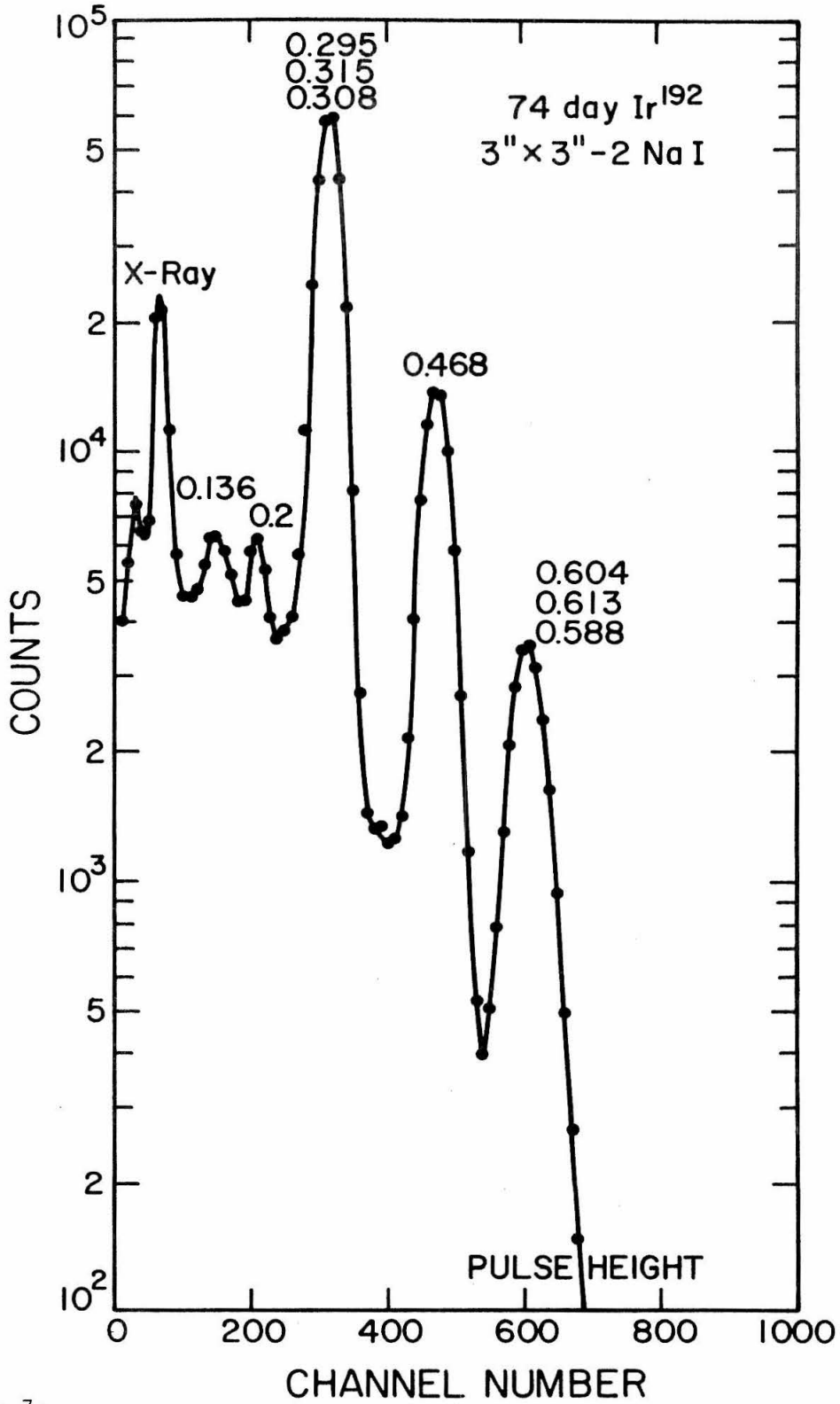


Figure 7:

energy resolution of NaI spectrometers results in the need of considerable corrections due to interference from these cascades. The Coulomb excitation measurements suffer from the appearance of strong perturbations during the excitation process, which may alter the hyperfine interaction and complicate data analysis considerably.

V.2 Source Preparation

The ^{192}Ir activity was produced by bombarding highly enriched ^{191}Ir powder, with neutrons at the MTR reactor (flux $\approx 10^{14}$ neutrons/ $\text{cm}^2\text{-sec}$). Since the thermal neutron absorption cross section is large in this case ($\sigma \approx 400$ barns), a very high specific activity was obtained. Consequently, only a few micrograms of activity were needed in preparing the ferromagnetic source. Several sources of different strength were prepared using the procedure described in Sec. IV.2. The source actually used in the measurement was then chosen to yield the highest coincidence rate without hurting the energy resolution or the true-to-random ratio.

V.3 The Gamma-Gamma Cascade

The magnetic moment of this 2^+ state was measured with two $5.0\text{ cm}^2 \times 1.0\text{ cm}$ Ge(Li) spectrometers having energy resolution of 2.6 keV at the 1330 keV ^{60}Co line. The only available cascade for this measurement is the $3^+(484\text{ keV})2^+(206\text{ keV})0^+$. This cascade is one of the weaker ones in the decay of ^{192}Ir . Also, the 206 keV line sits on a relatively large sloping background (Fig. 6). Our Ge(Li) detectors not only minimized interference from the strong ^{192}Pt

cascades, but also discriminated against the weak 489-201 keV sequence in ^{192}Os . This last cascade has the 2^{+} state in ^{192}Os as intermediate state. However, the half-life of the 2^{+} is much smaller than that of the 2^{+} state ($\tau_{2^{+}},/\tau_{2^{+}} \approx 0.13$) so that contributions from this cascade are small to begin with.

V.4 The Method and Results

The integral-reverse field method was used in measuring the magnetic moment of this state. The angular correlation coefficients, uncorrected for geometry, were found to be $A_2 = -0.157 \pm 0.008$ and $A_4 = -0.005 \pm 0.017$. The field reversal measurement was performed at a constant angle $\theta = \pm 3\pi/4$ between the detectors. For the large mean precession angle observed in this case, the field reversal ratio $R(\theta)$ is given by

$$R(\theta) = (\pm 3\pi/4) = \bar{\tau} \frac{b_2 \sin[\arctan(2\omega\tau)]}{1 - b_4 \cos[\arctan(4\omega\tau)]}$$

where b_2 and b_4 are the coefficients of $\cos(2\theta)$ and $\cos(4\theta)$, respectively, in $W(\theta)$. The weighted average result is

$$R(\theta = 3\pi/4) = (9.06 \pm 0.54) \times 10^{-2}.$$

Using the measured values of b_2 and b_4 , the mean precession angle $\omega\tau$ was derived from the above equation and found to be $\omega\tau = 0.58 \pm 0.07$ radians. The lifetime of this 2^{+} state is $\tau = 3.03 \times 10^{-10} \text{ sec}^{(4)}$, from which the magnetic moment was found to be $\mu_{2^{+}}(^{192}\text{Os}) = 0.56 \pm 0.08 \text{ nm}$.

This measurement was also repeated with one NaI detector accepting the 468 keV composite peak which includes the 484 keV and

and 489 keV osmium gamma rays and a Ge(Li) detector accepting the 206 keV line. A magnetic moment $\mu \simeq 0.12$ nm was found. The Ge(Li) energy "window" was then shifted to the background just on the high side of the 206 keV line and the measurement repeated. When the results of the first measurement were normalized to the results of the second, a magnetic moment $\mu \simeq 0.6$ nm was derived, but due to the sloping nature of the background under the 206 line, the accuracy of such a procedure is poor in this case; it is even worse for a two NaI detector configuration as is easily seen in Fig. 7.

VI. THE MAGNETIC MOMENTS OF THE FIRST AND SECOND 2^+ STATES IN ^{192}Pt .

VI.1 Introduction

The platinum isotopes are located at the spherical end of the osmium transition region. As such they should, and do, display a more vibrational character than the osmium isotopes. However, measurements on the 2^{+1} state in ^{194}Pt (11) and calculations based on the pairing-plus-quadrupole model (to be discussed in Chapter VII) showed deviations from pure collective excitations for all 2^{+1} states in the even Pt isotopes. Measurements of magnetic moments would therefore help in determining the excitation character of these states.

The magnetic moments of the 2^+ and 2^{+1} states described below were measured using the integral-reverse-field method described in Sec. II.5. The ferromagnetic source used in the measurements is the same one which was used in the measurement on the 2^+ state in ^{192}Os .

VI.2 The First 2^+ State

The magnetic moment of the first 2^+ state, at 316.49 keV, in ^{192}Pt was measured with two Ge(Li) detectors using the cascade $2^+(296 \text{ keV})2^+(316 \text{ keV})0^+$, (Fig. 5). The angular correlation measurement resulted in angular correlation coefficients, uncorrected for geometry, $A_2 = -0.095 \pm 0.005$ and $A_4 = 0.118 \pm 0.006$. Precessions were measured at angles $\theta = \pm 115^\circ$ between the detectors. At this angle the logarithmic derivative of the observed angular distribution, shown in Fig. 8, reaches its largest absolute value, and maximizes the integral-reverse field ratio $R(\theta)$ which for $\omega\tau \ll 1$ can be written as (Sec. II.5):

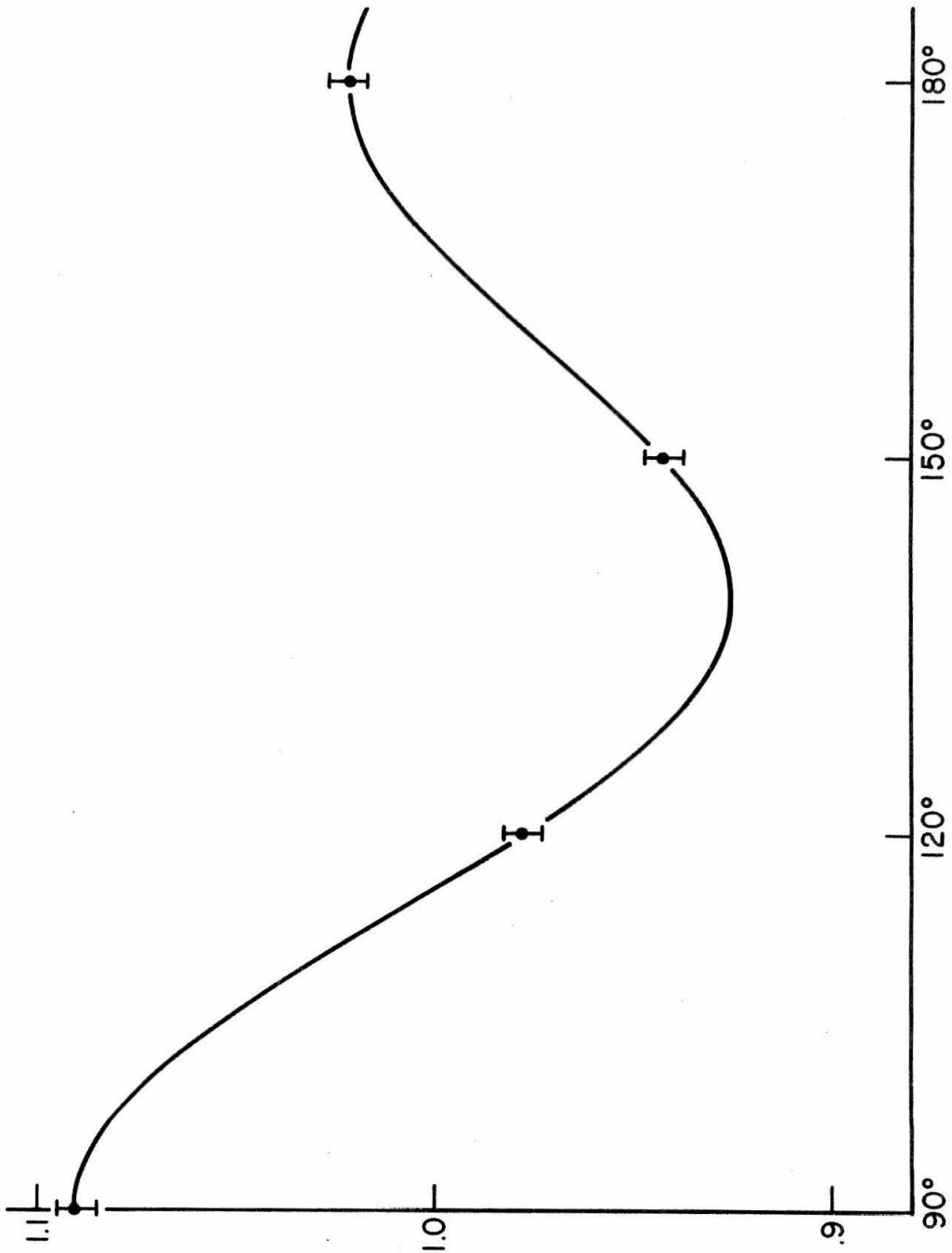


Figure 8: Angular distribution of the $2^+(296 \text{ keV})2^+(316 \text{ keV})0^+$ cascade in ^{192}Pt .

$$R(\theta) = - \frac{\partial W / \partial \theta}{W(\theta)} \omega \tau + 0[(\omega \tau)^3].$$

The field reversal measurement resulted in

$$R(\theta = 115^\circ) = (2.67 \pm 0.14) \times 10^{-2}$$

from which $\omega \tau = 0.088 \pm 0.006$ radians was obtained. With an internal magnetic field of platinum in iron $H = -1.235 \times 10^6$ Oe⁽⁴⁾ and the mean life to this state $\tau = (5.05 \pm 0.43) \times 10^{-11}$ sec⁽⁴⁾, the magnetic moment was found to be $\mu_{2^+}({}^{192}\text{Pt}) = 0.56 \pm 0.06$.

The result is in excellent agreement with Coulomb excitation measurements⁽¹²⁾ and also with other gamma-gamma perturbed correlation measurements which were performed with two NaI detectors and had to use the $4^+(468 \text{ keV})2^+(316 \text{ keV})0^+$ cascade because of the poorer energy resolution of NaI spectrometers^{8,13,14,15}.

VI.3 The Second 2^+ State

There are several cascades in ${}^{192}\text{Pt}$, which have the second 2^+ state, at 612.43 keV, as an intermediate state. The strong $3^+(308 \text{ keV})2^+(296 \text{ keV})2^+$ cascade has practically an isotropic angular distribution. All other cascades involve at least one radiation belonging to the 600 keV group and usually one of the 300 keV group (Figs. 6 & 7). Use of high resolution, high efficiency detectors is then highly desirable. The $2^+(308 \text{ keV})2^+(612 \text{ keV})0^+$ cascade was studied in order to obtain the magnetic moment of the second 2^+ state, at 612.43 keV, in ${}^{192}\text{Pt}$. Possible interference from the highly anisotropic $3^+(604 \text{ keV})2^+(316 \text{ keV})0^+$ cascade was minimized by the use of high resolution Ge(Li) spectrometers. The gamma rays were detected by

40 cm³ and a 25 cm³ detector having 2.8 keV and 3.1 keV energy resolution, respectively, at the 1330 keV ⁶⁰Co line. The experimental angular correlation coefficients were found to be $A_2 = -0.11 \pm 0.01$ and $A_4 = -0.029 \pm 0.011$. Field reversal measurements were conducted at angles $\theta = \pm 150^\circ$, at which the angular distribution reaches its maximum logarithmic slope. The results are: $R(\theta = 150^\circ) = (1.26 \pm 0.25) \times 10^{-2}$ from which $\omega\tau = 0.054 \pm 0.011$ radians was obtained. The mean life of this state has recently been measured⁽¹³⁾ to be $\tau = (2.9 \pm 0.3) \times 10^{-11}$ sec. Using this value and the internal magnetic field $H = -1.235 \times 10^6$ Oe, we get $\mu_{2^+}({}^{192}\text{Pt}) = 0.62 \pm 0.14$. This result agrees with predictions based on most collective nuclear models and makes the measured small magnetic moment of the 2^+ state in ¹⁹⁴Pt ($\mu_{2^+}({}^{194}\text{Pt}) = 0.14$ ^(8,11)) stand out in contrast. This discrepancy is possibly due to incorrect value of the measured mean life of that state.

VII. DISCUSSION OF EXPERIMENTAL RESULTS

VII.1 Summary of Experimental Results in the Osmium Region

The results of our experiments on ^{190}Os , ^{192}Os and ^{192}Pt are summarized in Table VII.1. The g-factor of all investigated states are the same within experimental errors. This would indicate the validity of collective description of low-lying states in this region. Unfortunately, these measurements depend on the lifetimes of these states which are not known very accurately. Therefore, it is not possible, using our results, to determine the possible systematic trends of magnetic moments in this region.

All g-factors display the reduction from the hydrodynamical model value of $\approx Z/A$. This is attributed to pairing-force effects which cause the nucleus to deviate from a rigid motion (see Sec. VII.2). The g-factor of the second 2^+ state in ^{192}Pt may indicate that the non-collective effects, in all 2^+ states of the Pt isotopes, proposed by Kumar and Baranger (cf. Sec. VII.2) are not present. This g-factor is also in contrast with the measured g-factor of the equivalent state in ^{194}Pt , by Agarwal et al.,⁽¹¹⁾ mentioned in Sec. VI.3. However, since the mean precession angle ω_T for the 2^+ state in ^{194}Pt is approximately the same as our ω_T for the same state in ^{192}Pt , it is very possible that the measured lifetime of the 2^+ state in ^{194}Pt is wrong, being too high by a factor of 2. The g-factors of the first 2^+ states in ^{190}Os and ^{192}Os indicate that earlier measurements by the Goldring group at the Weizmann Institute are inaccurate, being too high by approximately a factor of 2.

TABLE VII.1

	$^{190}\text{Os}(2^+ \text{ state})$	$^{190}\text{Os}(4^+ \text{ state})$	$^{192}\text{Os}(2^+ \text{ state})$	$^{192}\text{Pt}(2^+ \text{ state})$	$^{192}\text{Pt}(2^{+1} \text{ state})$
	$3^+(569)2^+(187)0^+$	$4^-(1030)4^+(361)2^+$	$3^+(484)2^+(206)0^+$	$2^+(296)2^+(316)0^+$	$3^+(308)2^+(612)0^+$
A_2	$-0.13 \pm 0.05^\dagger$	0.068 ± 0.007	-0.157 ± 0.008	-0.095 ± 0.005	-0.11 ± 0.01
A_4	$-0.008 \pm 0.006^\dagger$	0.01 ± 0.04	-0.005 ± 0.017	0.118 ± 0.006	-0.029 ± 0.011
θ	ROTATION	135°	135°	115°	150°
$R(\theta) \times 10^2$	-	0.6 ± 0.12	9.06 ± 0.54	2.67 ± 0.14	1.25 ± 0.25
$\omega \tau(\text{rad.})$	0.65 ± 0.05	0.060 ± 0.014	0.58 ± 0.07	0.088 ± 0.006	0.054 ± 0.011
$H(\text{kG})$	-1430	-1430	-1430	-1235	-1235
$\tau(\text{psec})$	346	40 ± 20	303	50.5 ± 4.3	29 ± 3
g	0.27 ± 0.03	0.22 ± 0.12	0.28 ± 0.04	0.28 ± 0.03	0.31 ± 0.07

Our results bring these g-factors back into the realm of collective excitations.

VII.2 Collective Nuclear Models and the Osmium Transition Region

a) Introduction

Collective phenomena in atomic nuclei were suggested as early as 1930. Thibaud¹⁶⁾ pointed out that alpha-decay measurements by Rosenblum¹⁷⁾ on ^{212}Bi could be explained if the daughter nucleus ^{208}Tl behaves as a system of rotation. In 1937 N. Bohr and Kalckar¹⁸⁾ introduced surface vibrations of a quantum fluid as a possible explanation of energy level densities in heavy nuclei. This liquid-drop model was used by von Weizsäcker¹⁹⁾ in 1939 to derive his famous mass formula. Nuclear shape calculations with this model²⁰⁾ resulted in the spherical shape being the most stable one. It was not until 1950 that Rainwater²¹⁾ showed that a single particle moving in a deformed oscillator well might have an energy lower than when moving in a similar spherical well. Rainwater's discovery was first used to calculate the deviations of the measured values of magnetic dipole moments from the predictions of the single-particle shell model. This was done by A. Bohr²²⁾ using a rotational model, and by Foldy and Milford²³⁾ using a vibrational model.

A detailed phenomenological investigation of collective properties of atomic nuclei was introduced by A. Bohr²⁴⁾ and by A. Bohr and B. Mottelson²⁵⁾ who treated the nucleus as a rotating-vibrating, incompressible liquid drop. Their ideas were expanded and developed in recent years (see Ref. 26 for a recent review of

phenomenological collective models). The success of these models results in a better understanding of the nature of the nuclear forces which are responsible for collective nuclear properties and paved the way to microscopic descriptions of collective phenomena in atomic nuclei.

Microscopic models approximaté the nuclear forces by short-range forces which tend to keep the nuclear shape spherical, and long-range forces which act to deform the nucleus. Treatments of these forces were reserved to cases in which one type dominates over the other (see Refs. 27,28 for a review of microscopic collective models). These treatments carefully avoided the osmium transition region in which energy levels and electromagnetic moments show large deviations^{29,30)} from both the rotational model and the vibrational model.

For a discussion of magnetic dipole moments in the osmium transition region, there are three models which played an important role. These are the cranking model, the rotational-vibrational model and the pairing-plus-quadrupole model. In all these models, the short-range forces are approximated by the pairing force³¹⁾ and the long-range ones, by the quadrupole force.

b) The Cranking Model³²⁾:

In this model the self-consistent field which determines the single-particle orbitals is assumed to be cranked around externally. The rotational energy of the system, in this description, is the extra energy necessary for the nucleons to follow a slow rotation thereby sustaining the field. The collective rotation takes place

perpendicularly to the nuclear symmetry axis and gives rise to a collective angular momentum \vec{R} . In the ground state of an even-even nucleus we have $\vec{R} = \vec{I}$. The collective motion of protons and neutrons also results in an instantaneous magnetic moment given by

$$\vec{\mu}_c = \sum_i (g_l^{(i)} \vec{\ell}_i + g_s^{(i)} \vec{s}_i) .$$

This is usually expressed in terms of a collective g-factor g_R defined by the relation

$$\vec{\mu}_c \equiv g_R \vec{R} .$$

If the pair-correlation interaction is included in the cranking approximation, the collective g-factor g_R is given by ³³⁾

$$g_R = \frac{J_p}{J} + (g_s^{(p)} - 1) \frac{W_p}{J} + g_s^{(n)} \frac{W_n}{J}$$

where J refers to the total moment of inertia; J_p refers to the proton contribution to J ; and

$$W = 2h^2 \sum_{\nu, \mu} \frac{\langle \nu | j_1 | \mu \rangle \langle \mu | s_1 | \nu \rangle}{E_\nu + E_\mu} (u_\nu v_\mu - v_\nu u_\mu)^2$$

where $u_\nu (v_\nu)$ is the probability amplitude that the state ν is not occupied (is occupied) in the pairing coupling scheme. The last two terms in g_R are the spin contributions of the protons and neutrons to g_R , and their combined effect is small since $(g_s^{(p)} - 1)$ is nearly the same magnitude as $g_s^{(n)}$ but of opposite sign. Neglecting spin contributions we get then

$$g_R \approx \frac{J_p}{J_p + J_n}$$

where

$$J = 2\hbar^2 \sum_{\nu, \mu} \frac{|\langle \mu | j_1 | \nu \rangle|^2}{E_\nu + E_\mu} (u_\nu v_\mu - u_\mu v_\nu)^2 .$$

The moment of inertia is very sensitive to the strengths of the pairing correlation force. If the strength of the pairing force is the same for protons and neutrons then the ratio of their contributions to the moment of inertia will be equal to the ratio of their relative numbers $J_n / J_p = N/Z$. In this case we get

$$g_R = Z/A$$

which is the hydrodynamical value. However, experimental values are consistently lower than the hydrodynamical value. Also, the experimentally observed odd-even mass differences for protons and neutrons lead to different pairing-force strengths for protons and neutrons. The protons' pairing force is found to be larger than the neutrons' one, and this is explained in terms of the differences in the oscillator shells they occupy. Another effect which lowers g_R from its hydrodynamical value is the 'blocking effect' in which breaking of a pair of quasi particles blocks the states they occupy from being populated by other pairs.

Calculations of collective g-factors using the cranking formula including pair correlation effects and 'blocking', were originally performed by Nilsson and Prior³³⁾. Since it obviously is a 'deformed' nuclear model, it was applied only to deformed nuclei ($150 < A < 190$ and $A > 225$). The calculations were improved and extended to cover the deformed edge of the osmium transition region,

by Prior, Boehm and Nilsson³⁴⁾. Where calculated, they are in satisfactory agreement with our results (see Table VII.2).

c) The Rotation-Vibration Model^{35,36)}

This model is a macroscopic model following the Bohr-Mottelson description^{24,25)}, in which the nuclear shape is expanded in spherical harmonics stopping at the quadratic term:

$$R = R_0 [1 + a_0 Y_{20} + a_2 (Y_{22} + Y_{2-2})].$$

The linear term does not appear since it corresponds to the motion of the nucleus as a whole. The collective Hamiltonian which is based on this description, uses the expansion coefficients a_0 and a_2 as generalized coordinates. In the above body-fixed axes, it decomposes into a vibrational term, a rotational term, and a rotation-vibration cross-term. This last term is usually neglected or treated very crudely by allowing for the so-called "centrifugal stretching" of the nucleus.

In the present model, the effect of this term on the generalized coordinates is calculated directly in the following manner. The protons' and neutrons' contributions to the nuclear shape are treated separately. The two systems are strongly coupled and rotate with the same angular velocity. Pair-correlation effects cause the proton shape to be less deformed than the neutron shape since the pairing force is larger for protons, i.e., $\beta_0(p) < \beta_0(n)$ where β_0 is the equilibrium deformation parameter. The average nuclear deformation is given then by:

$$\beta_0 = \frac{N\beta_0(n) + Z\beta_0(p)}{A}$$

The deformation parameter β is related to a_0 and a_2 through the relations

$$a_0 = \beta \cos \gamma \quad \text{and} \quad a_2 = \frac{1}{\sqrt{2}} \sin \gamma$$

where γ is the 'asymmetry parameter'; $\gamma = 0$ for axial symmetry. We therefore write

$$a_0 = \beta_0 + a_0' \quad \text{and} \quad a_2 = 0 + a_2'$$

where a_0' and a_2' are the corrections due to the vibrational degrees of freedom.

In addition to lowering the hydrodynamical value of g_R , the different deformations of the protons' and neutrons' shapes also cause the g -factor to depend on the (body) rotation axis, i.e.,

$$g_v = \frac{J_v(p)}{J_v} \quad \text{where} \quad J_1 = B(3a_0^2 + 2a_2^2 \pm 2\sqrt{6} a_0 a_2).$$

B is the mass parameter in the Bohr-Mottelson description, which is proportional to the system density, i.e., $B_p/B = Z/A$. The calculations can be performed in the body fixed axes and then transformed back to the laboratory system, using the rotation matrices. However, in the laboratory system, the magnetic moment $\vec{\mu}$ can be shown to be given by

$$\mu_i = g^{(0)} I_i + g^{(1)} \sum_{\mu, \nu} (2\mu, 1\nu | 1i) \alpha_{\mu} I_{\nu}$$

where α_{μ} correspond to the a_{μ} but in the lab system. The constants $g^{(0)}$ and $g^{(1)}$ are functions of g_1 and g_2 (of the body system) and are given by

$$g^{(0)} = \frac{Z}{A} (1 - 2f) \left(1 + \frac{2}{3} f\right) \simeq \frac{Z}{A} \left(1 - \frac{4}{3} f\right)$$

$$g^{(1)} = -\frac{Z}{A} (1 - 2f) \frac{3}{2} \sqrt{10} \frac{f}{\beta_0}$$

where

$$f = \frac{\beta_0 - \beta_0(p)}{\beta_0} \simeq \frac{N}{A} \left(\frac{\beta_0(n)}{\beta_0(p)} - 1 \right).$$

The collective g-factor is then given by

$$g_R = \frac{\langle II | \mu_0 | II \rangle}{I}.$$

The results of the calculations are as follows:

(i) ground-state rotational band

$$g_R = \frac{Z}{A} (1 - 2f)$$

(ii) γ -rotational band

$$g_R = \left(1 + \frac{8}{3} \frac{f}{I(I+1)}\right) \frac{Z}{A} (1 - 2f)$$

(iii) β -rotational band

$$g_R = \frac{Z}{A} (1 - 2f)$$

For all of the vibrational states this model predicts

$$g = g^{(0)} \simeq \frac{Z}{A} \left(1 - \frac{4}{3} f\right).$$

Note that if the equilibrium deformations of the protons' and neutrons' shapes are the same, i.e., if $f = 0$ we get for all collective states, regardless of their character, the same collective g-factor equal to the hydrodynamical value $g_R = Z/A$.

It has been shown by Greiner³⁷⁾ using the quasi-spin

formalism that the equilibrium deformations of the protons' and neutrons' shapes are inversely proportional to the square roots of their respective pairing-force constraints G_p and G_n , i.e.,

$$\frac{\beta_0(p)}{\beta_0(n)} = \sqrt{\frac{G_n}{G_p}} .$$

Even-odd mass differences have shown that

$$G_p \simeq \frac{30}{A} \quad \text{while} \quad G_n \simeq \frac{20}{A} .$$

The values quoted in Table VII.2 have been based on these numbers. They are in good agreement with our results.

d) The Pairing-Plus-Quadrupole Model

This model consists of the one-body shell model with the pairing and quadrupole forces as residual two-body interactions. The pairing force simulates the short-range part of nuclear forces. It preserves the most important features of the (more physical) δ -force, and is simpler to treat. It is responsible for the energy gap seen in the spectra of even-even nuclei³⁸⁾ and the systematic odd-even mass differences from which its strength is usually derived. Being isotropic, it tries to keep the nucleus spherical. The quadrupole force approximates the long-range part of nuclear forces. This particular form was chosen to explain the enhanced transition rates $B(E2)$ between nuclear states, the large static quadrupole moments observed in many nuclei and the existence of rotational bands in nuclei. The success of the Nilsson model³⁹⁾ is ample evidence of the importance of such an interaction in nuclear structure. This force does not, however, explain nuclear features

other than those with quadrupole character (for example, the 3^- state in ^{208}Pb). For nondeformed nuclei, this force makes the spherical shape less stable and increases the collectivity of quadrupole vibrational motion.

The Hamiltonian of this model consists then of three parts:

$$H = H_s + H_p + H_Q.$$

In the second quantization formalism we have

$$H_s = \sum_{\alpha} \epsilon_{\alpha} a_{\alpha}^{\dagger} a_{\alpha}$$

$$H_p = -\frac{1}{4} G \sum_{\alpha, \beta} a_{\alpha}^{\dagger} a_{\alpha}^{\dagger} a_{\beta} a_{\beta}$$

$$H_Q = -\frac{1}{2} \times \sum_{\alpha\beta\gamma\delta} \sum_{\mu} \langle \alpha | Q_{\mu} | \gamma \rangle \langle \delta | Q_{\mu} | \beta \rangle a_{\alpha}^{\dagger} a_{\beta}^{\dagger} a_{\delta} a_{\gamma}$$

where α denotes all quantum numbers necessary to specify a state, i.e., $a_{\alpha}^{\dagger} |0\rangle = |n\ell j m\rangle$ and $a_{\alpha}^{\dagger} |0\rangle = (-1)^{j-m} |n\ell j -m\rangle$ the time-reversed state. The quadrupole moment operator is $Q_{\mu} = r^2 Y_{2\mu}(\theta, \varphi)$.

This model was first discussed by Belyaev⁴⁰⁾. It was applied to single closed-shell nuclei by Kisslinger and Sorensen⁴¹⁾ who later extended their calculations to all spherical nuclei⁴²⁾. A recent review of the pairing-plus-quadrupole model is presented in Ref. 43. In relation to the osmium transition region, where the two residual forces are expected to be of equal importance, the only pertinent investigation was performed by K. Kumar and M. Baranger. In a series of papers (Refs. 43,44,45,46,47), these

authors systematically investigated the roles of these forces by a method which treats the pairing force and the quadrupole force on the same footing, without any a priori assumptions about the nuclear shape. Their approach is based on the following procedure:

(i) A deformed one-body Hamiltonian is defined

$$H_D = H_s - \sum_{\alpha\beta} \langle \alpha | \sum_{\mu} D_{\mu}^* Q_{\mu} | \beta \rangle a_{\alpha}^{\dagger} a_{\beta}.$$

The single particle states and eigenvalues of H_D are found; that is the equation

$$H_D |i\rangle = \eta_i |i\rangle$$

is solved for all possible values of the parameters D_{μ} .

(ii) The BCS procedure⁴⁸⁾ is applied to these levels, resulting in the quasi-particle energies

$$E_i = [(\eta_i - \lambda)^2 + \Delta^2]^{1/2}$$

and the occupation probabilities

$$v_i^2 = \frac{1}{2} \left(1 - \frac{\eta_i - \lambda}{E_i} \right) = 1 - u_i^2$$

where $\sum_i 1/E_i = 4/G$, $\sum_i v_i^2 = N$ (number of particles), and $\Delta = G/4 \sum_i u_i v_i$.

(iii) This BCS wave function is then used to find the expectation value of the total Hamiltonian. This deformation energy (as a function of D_{μ}) is found to be

$$E^0(D_{\mu}) = \sum_{i,\alpha} v_i^2 |\langle i|\alpha\rangle|^2 \epsilon_{\alpha} - \frac{\Delta^2}{G} - \frac{1}{2} \times \sum_{\mu} |q_{\mu}|^2$$

where

$$q_{\mu} = \sum_i v_i^2 \langle i | Q_{\mu} | i \rangle$$

is the average mass quadrupole moment of the nucleus.

(iv) The equilibrium shape of the nucleus is found by using the D_{μ} 's as variational parameters to find the minimum of E^0 . It has been shown⁴⁹⁾ that when $E^0(D_{\mu})$ is stationary, the self-consistent condition $D_{\mu} = \chi q_{\mu}$ is satisfied. This means that the potential $-\sum_{\mu} D_{\mu}^* Q_{\mu}$ in which the wave functions are calculated, is the same as $-\chi \sum_{\mu} q_{\mu}^* Q_{\mu}$ which is the average potential produced for one particle by its quadrupole interaction with all others. Since the deformation energy $E^0(D_{\mu})$ is rotationally invariant only two of D_{μ} 's are independent. These are taken to be linear combinations of the D_{μ} 's and when expressed in a suitable coordinate axes are related to conventional deformation parameters β and γ by

$$D_0 = D \cos \gamma \text{ and } D_2 = D \sin \gamma \text{ where } D = m\omega_0^2 \beta$$

(ω_0 and m relate to the harmonic oscillator Hamiltonian H_s).

So far, only the static Hamiltonian has been considered. Kumar and Baranger then solved Bohr's collective Hamiltonian²²⁾ which includes seven arbitrary functions of β and γ (the potential energy, the three moments of inertia for rotations and the three mass parameters for vibrations). This is done by a numerical method discussed in detail in Ref. 48. To compare their model with previous models, these authors first applied it⁴⁷⁾ to the only nuclear region in which earlier models encountered difficulties. This is the osmium transition region, carefully avoided earlier by nuclear

theorists who wished to compare their predictions with experimental results.

The main predictions of the pairing-plus-quadrupole model in the osmium region are: the nuclear shape changes around ^{190}Os from prolate ($^{182-186}\text{W}$) to asymmetric ($^{190-192}\text{Os}$) to oblate ($^{192-196}\text{Pt}$). There is strong coupling between the β -bands and γ -bands and rapid changes in quadrupole moments and $B(E2)$ values. With respect to magnetic properties, small $B(M1)$ values are predicted in fair agreement with experiment (in the hydrodynamical model by Bohr and Mottelson²⁵) $B(M1)$ values vanish completely). The reduction of the magnetic moment, of first 2^+ states, from the hydrodynamical values is observed, but the individual numbers do not always agree with experimental results (cf. Table VII.2).

e) Discussion

In Table VII.2 we present a summary of our experimental results, together with the predictions of the three nuclear models discussed above.

The first feature that one notices is that the predictions of all three models are in satisfactory agreement with our experimental results. This is not very surprising since these models basically use the same collective Hamiltonian and differ only in their treatments of the residual interactions. Greiner treats it phenomenologically, while Kumar and Baranger treat it microscopically. In fact, their treatment of the pairing-plus-quadrupole interaction, outlined in (d), is very similar to the cranking model treatment. The

main difference is that unlike the cranking model treatment, they do not assume a deformed shape for the nuclear surface, and secondly, they solve the Bohr's collective Hamiltonian by an accurate numerical method.

The best over-all agreement with our results comes from Greiner's model. However, his is a phenomenological model that does not shed any light on the origins of the nuclear forces and therefore is not very exciting. The treatment of the pairing-plus-quadrupole interaction by Kumar and Baranger may be regarded as an extension of the cranking approach. This point is discussed by them⁴⁶⁾. However, they are quick to point out the conceptual differences between the two treatments.

Finally, it should be mentioned that all these models attempt to describe nuclear properties over a range of nuclei using a few parameters. Their results therefore, are not expected to be in complete agreement with nuclear properties of any one nucleus. Rather, they try to predict and explain general trends and systematics of nuclear properties in a whole region of nuclei. As such, they are all successful and in particular, the pairing-plus-quadrupole model which covers the largest range of nuclei.

TABLE VII.2

Summary of the measured magnetic moments in ^{190}Os , ^{192}Os and ^{192}Pt together with theoretical predictions based on the pairing-plus-quadrupole model⁴⁷⁾, Greiner's model³⁶⁾ and the cranking model³⁴⁾.

Nucleus	$\mu_{\text{exp.}}$ (n.m.)	Kumar & Baranger ⁴⁷⁾	Greiner ³⁶⁾	Prior et al. ³⁴⁾
^{190}Os				
2^+	0.54 ± 0.06	0.593	0.605	0.62
4^+	0.88 ± 0.48	1.181	1.210	
^{192}Os				
2^+	0.56 ± 0.08	0.590	0.599	0.58
^{192}Pt				
2^+	0.56 ± 0.06	0.425	0.614	
2^{+1}	0.62 ± 0.14	0.441	0.647	

PART 3: HYPERFINE MAGNETIC FIELDS AT "IMPURITY" ATOMS IN FERRO-
MAGNETIC HOSTS

The nucleus of an atom in a solid experiences magnetic fields originating from three possible sources. These are: Its own electronic configuration, its neighboring atoms in the lattice, and external application of magnetic fields. If this atom is diamagnetic, all its electrons are paired off to yield no magnetic field at the nucleus. If, in addition, this atom is embedded in a ferromagnetic host lattice, its nucleus will experience strong magnetic fields, stronger usually than any laboratory magnet can produce. These fields are very sensitive to the type of the "impurity" atom and in fact show appreciable but systematic fluctuations as a function of the atomic number of the impurity. The mechanism which produces this behavior is only vaguely understood. The experiments described below were undertaken to furnish more data on these fields, which should lead to a better understanding of the solid state and in particular, ferromagnetism.

VIII INVESTIGATION OF INTERNAL MAGNETIC FIELDS OF ^{111}Cd IN NICKELVIII.1 Introduction

The radioactive decay of ^{111}In to ^{111}Cd is one of the few cases in which the technique of time-differential perturbed angular correlation can be used with high accuracy to investigate hyperfine interactions. In particular, it can be used to investigate the distribution of hyperfine magnetic fields acting on Cd impurities embedded in ferromagnetic hosts. The question of whether the values quoted for the measured internal fields pertain to impurities in substitutional lattice sites, interstitial sites or both, is of obvious importance to the theorist who bases his calculations on a solid state model.

VIII.2 Preparation of Sources

Sources were made by two independent methods:

1. Natural cadmium metal foil (12.75% ^{111}Cd), 20 mils thick, was bombarded by 30 MeV protons, for a total of 5×10^{-3} Coulomb charge, to produce indium by the reaction $^{111}\text{Cd}(p,n)^{111}\text{In}$. Long-lived ^{114}In was not produced and the only competing activities were short lived.

The radioactive sample containing the In activity in the cadmium target was dissolved in concentrated nitric acid and the solution evaporated to dryness. The cadmium was separated from the indium through precipitation of the activity as the hydroxide by addition of ammonium hydroxide, followed by repeated heating and centrifuging of the mixture. The activity was then electroplated

onto a tapered nickel pin from a high pH cyanide solution. The pin was driven into a matching nickel pot which was then melted in an induction furnace using a levitating silver boat. The source was coined, in a hydraulic press, into a cylindrical shape, for a good magnetic contact.

2. Natural silver foil (48.65% ^{109}Ag), 5 mils thick, was bombarded by 40 MeV alpha particles, for a total of 9×10^{-2} Coulomb charge, to produce ^{111}In by the reaction $^{109}\text{Ag}(\alpha, 2n)^{111}\text{In}$ (and to minimize competing reactions). The sample was dissolved in nitric acid, evaporating to dryness and redissolved in distilled water. The silver was then precipitated with 1/2 N hydrochloric acid. The supernate containing the In activity was evaporated to dryness and redissolved in water. The activity was then electroplated onto a nickel pin from the resulting neutral solution and source prepared as in method 1.

VIII.3 The Gamma-Gamma Cascade

Figure 1 shows the level diagram of ^{111}Cd . The parent ^{111}In ($T_{1/2} = 2.8$ days) decays by K capture populating almost exclusively the 419 keV, $7/2^+$ level. The latter, decays to the $J^\pi = 1/2^+$ ground state only via the $7/2^+(173 \text{ keV}) \rightarrow 5/2^+(247 \text{ keV}) \rightarrow 1/2^+$ cascade. Consequently, the energy spectrum of the decay of ^{111}In , taken with a 7.6 cm x 7.6 cm NaI spectrometer, shown in Fig. 2, displays only the above-mentioned 173 and 247 keV gamma rays and interference from other radiations is non-existent. The above cascade, with the known mixing ratio in the 173 keV gamma ray ($\delta^2 = 0.21$) is highly

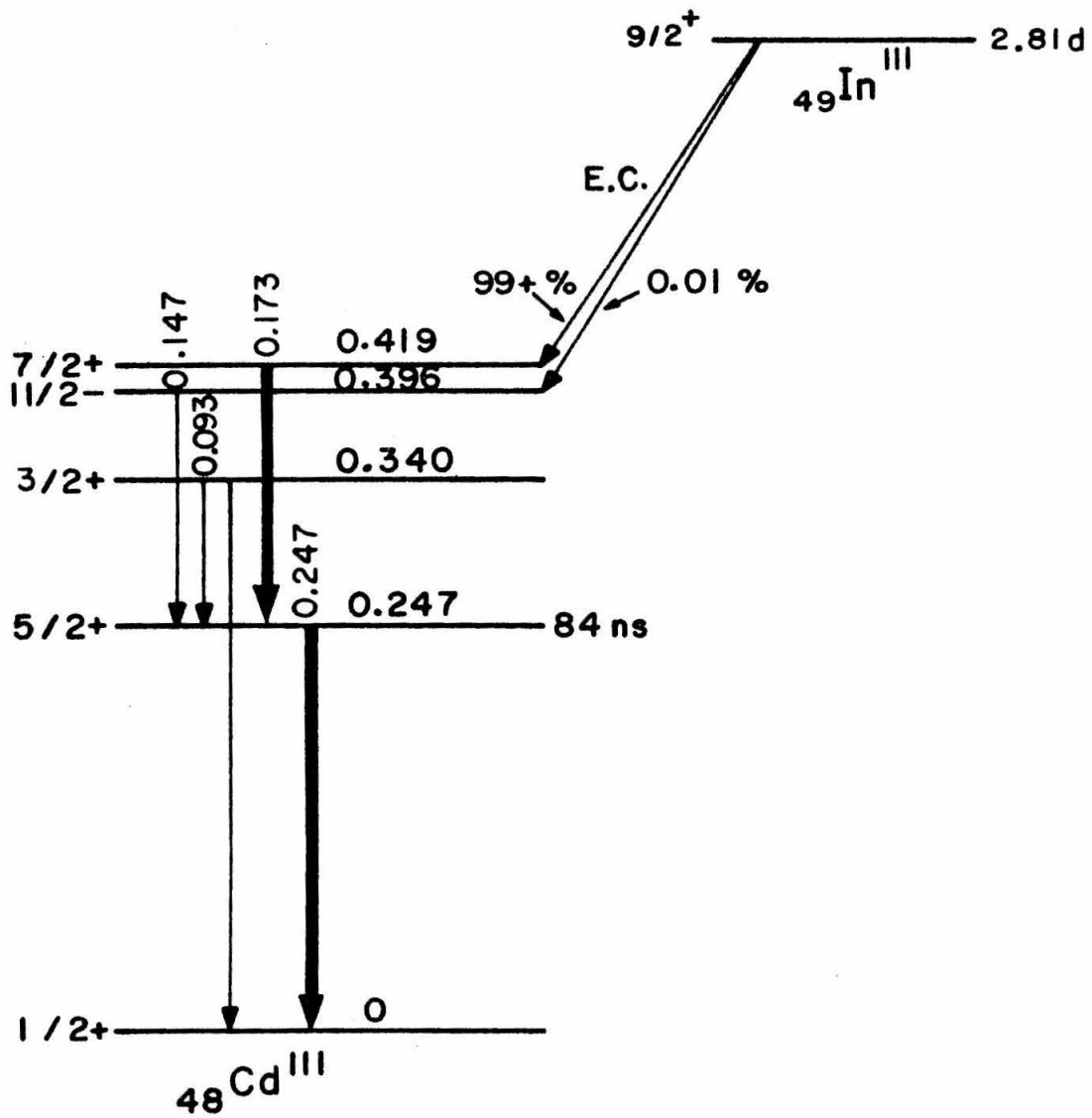


Figure 1
Decay scheme of $^{111}_{49}\text{Ir}$ (Energies in MeV)

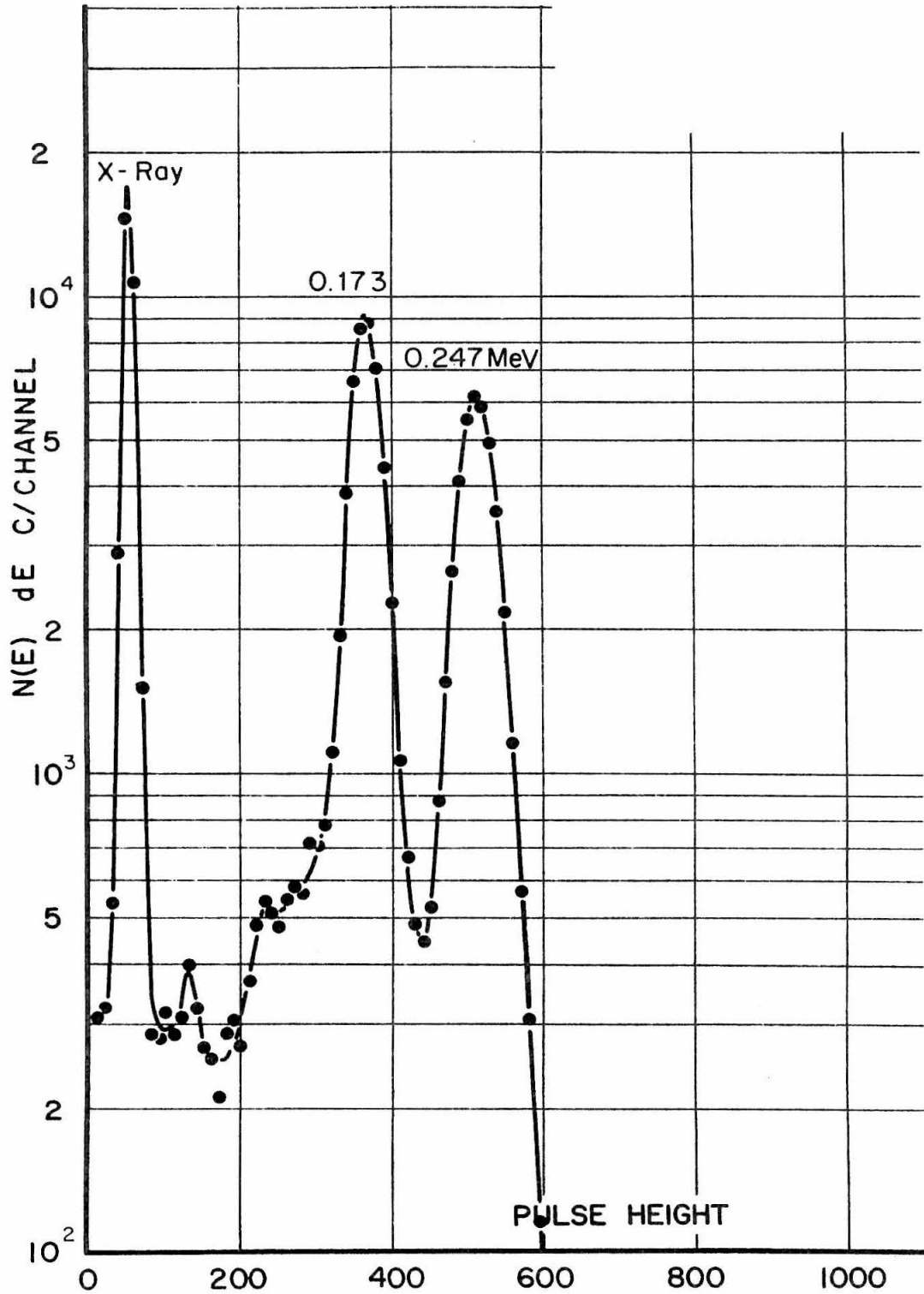


Figure 2: Energy spectrum of the radioactive decay of ^{111}In . Spectrum taken by a 7.6 cm x 7.6 cm NaI scintillation counter.

anisotropic. Also, the $5/2^+$ intermediate state has a relatively long half life ($T_{1/2} = 8.4 \times 10^{-8}$ sec) so that this cascade is well suited for a time-differential measurement. Also, hyperfine fields ranging from 5 kG to 200 kG can be investigated using this cascade.

VIII.4 Experimental Procedure

The two gamma rays were detected at a fixed angle θ with respect to one another, with runs taken at angles $\theta = 3\pi/4, \pi$ and $5\pi/4$ radians. The 177 keV γ_1 actuated the "start" channel and the 243 keV γ_2 , the "stop" channel. Saturation of the source was achieved with a small electromagnet. Compensating coils reduced any magnetic effects on the phototubes to a minimum. Data were collected in periods of 200 sec with 20 sec pauses, and stored "alternately" in the two halves of the analyzer. The magnetic field was reversed during each pause. Also, the singles count rate from each detector plus the triple coincidence rate were recorded, during each pause, and checked for irregularities during the several days runs.

Background runs were taken before and after runs and the time spectrum taken was also calibrated using a pulser and using annihilation radiation.

An RIDL 400 channel analyzer was used for source 1 produced by the reaction $^{111}\text{Cd}(p,n)^{111}\text{In}$ while a N.D. 4096 channel analyzer was used for source 2 produced by the reaction $^{109}\text{Ag}(\alpha,2n)^{111}\text{In}$.

VIII.5 Data Analysis and Results

As has been discussed earlier (Sec. II.5) it is customary to analyze data in terms of the field reversal ratio $R(\theta, t)$ which is independent of the lifetime of the intermediate state. Our analysis was performed on the difference

$$WT(\theta = \frac{3\pi}{4}, t, +H) - WT(\theta = \frac{3\pi}{4}, t, -H) \propto \frac{1}{\tau} e^{-t/\tau} 2b_2 \sin(2\omega_0 t).$$

In this case the b_4 term in $WT(\theta, t, H)$ vanishes so that only one frequency $\omega_0 = 2\omega_L$ is associated with the precession in the magnetic field. Also, background subtraction is taken care of automatically (although the statistical errors due to the background have to be accounted for). In addition, the mean life of the intermediate state was determined and checked against the time calibration of the apparatus. Finally, convenience in using the expression derived in Appendix A was also a contributing factor in data analysis methods.

The experimental data were Fourier analyzed by a straightforward Fourier transform (Figs. 3,4). A theoretical expression, modified to duplicate experimental conditions, was also Fourier analyzed (Fig. 5). In addition, a continuous theoretical expression was analyzed (Fig. 6) and the three Fourier transforms compared. It was found that modifying the continuous theoretical expression, introduced peaks in the transforms, due to the discreteness of the function, which far outweighed those due to the finiteness of time interval.

The results of the analysis were then used as initial guesses in a non-linear least-squares fitting program (a modified version of

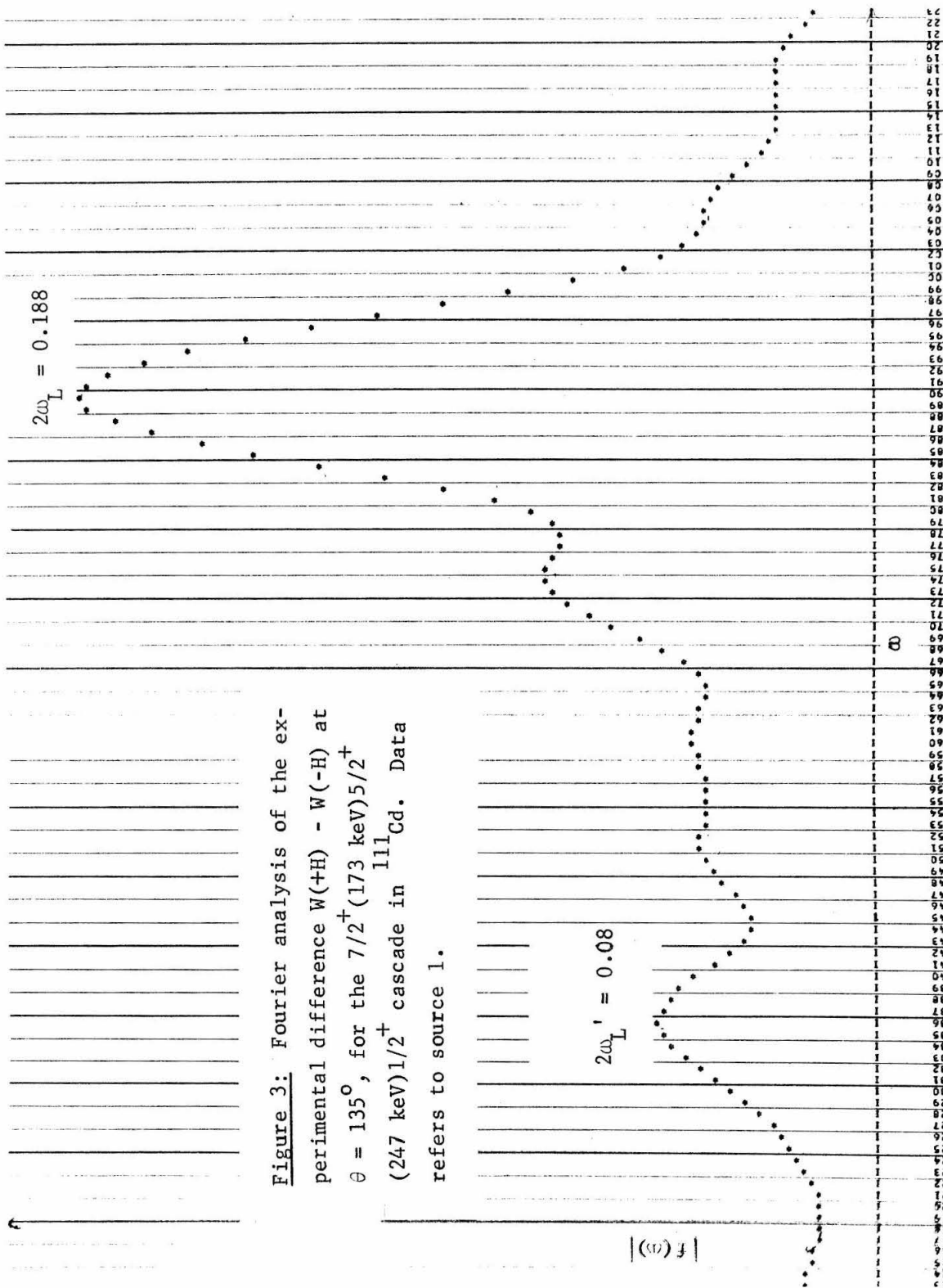


Figure 3: Fourier analysis of the experimental difference $W(+H) - W(-H)$ at $\theta = 135^\circ$, for the $7/2^+ (173 \text{ keV}) 5/2^+ (247 \text{ keV}) 1/2^+$ cascade in ^{111}Cd . Data refers to source 1.

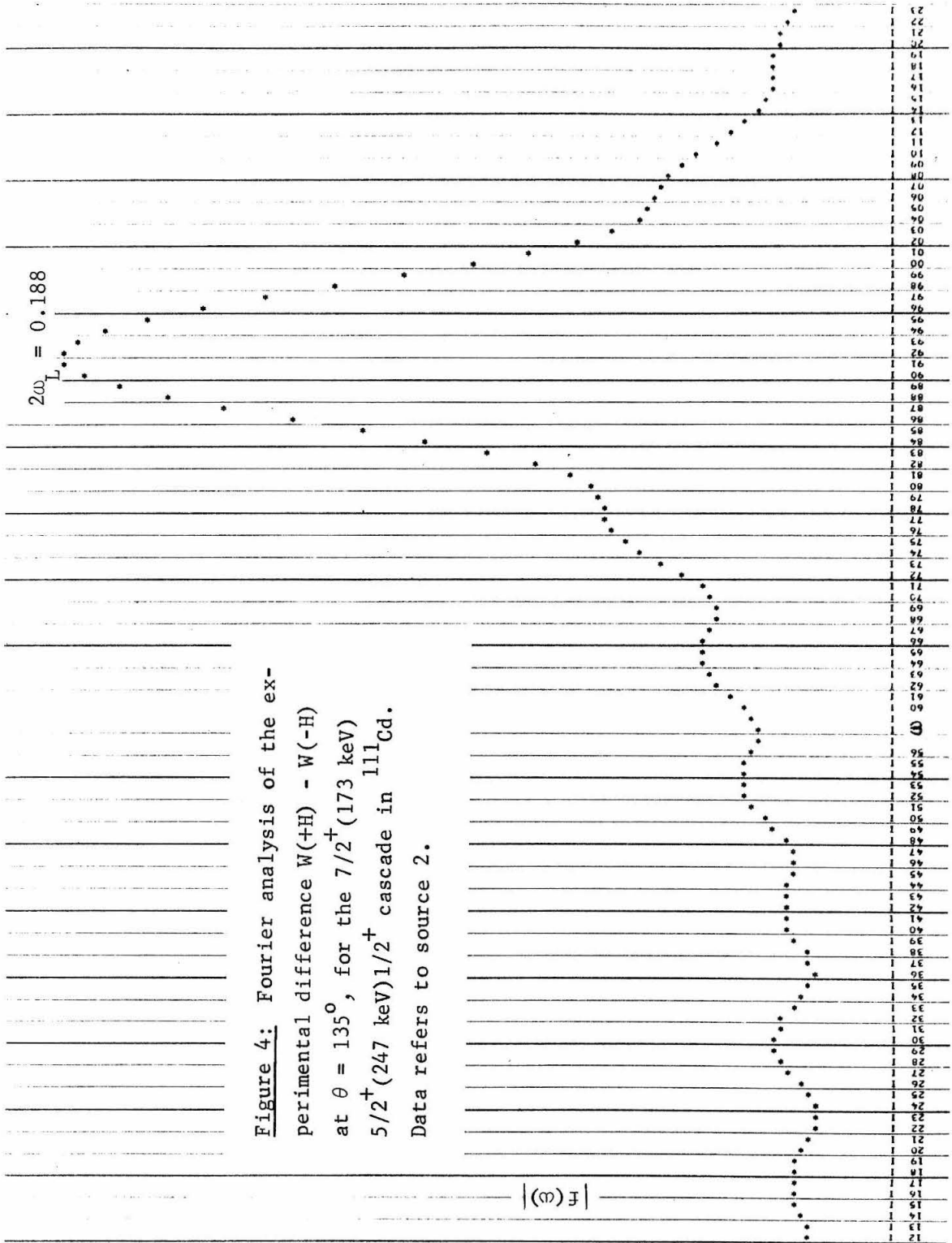
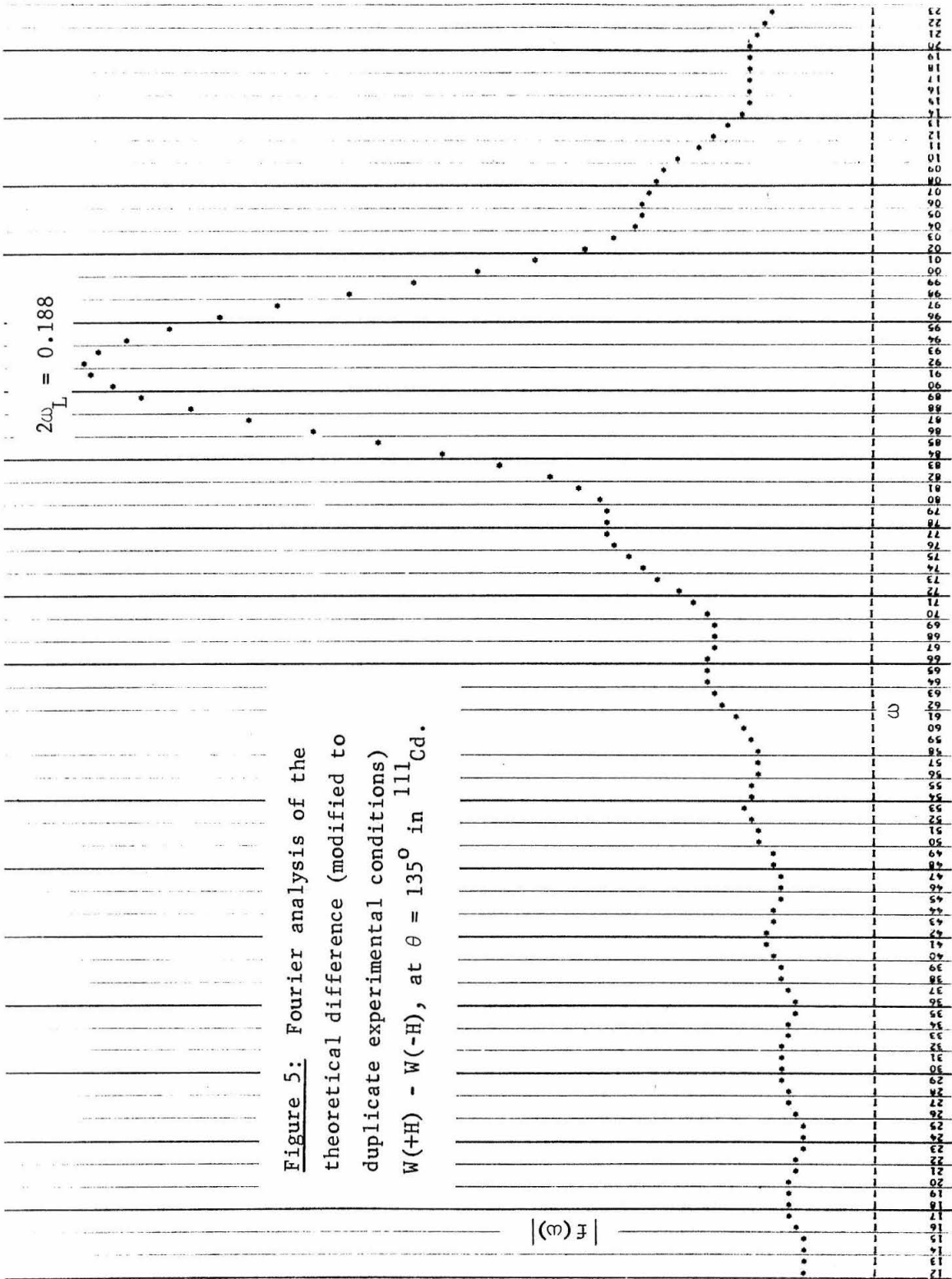


Figure 4: Fourier analysis of the experimental difference $W(+H) - W(-H)$ at $\theta = 135^\circ$, for the $7/2^+$ (173 keV) $5/2^+$ (247 keV) $1/2^+$ cascade in ^{111}Cd . Data refers to source 2.



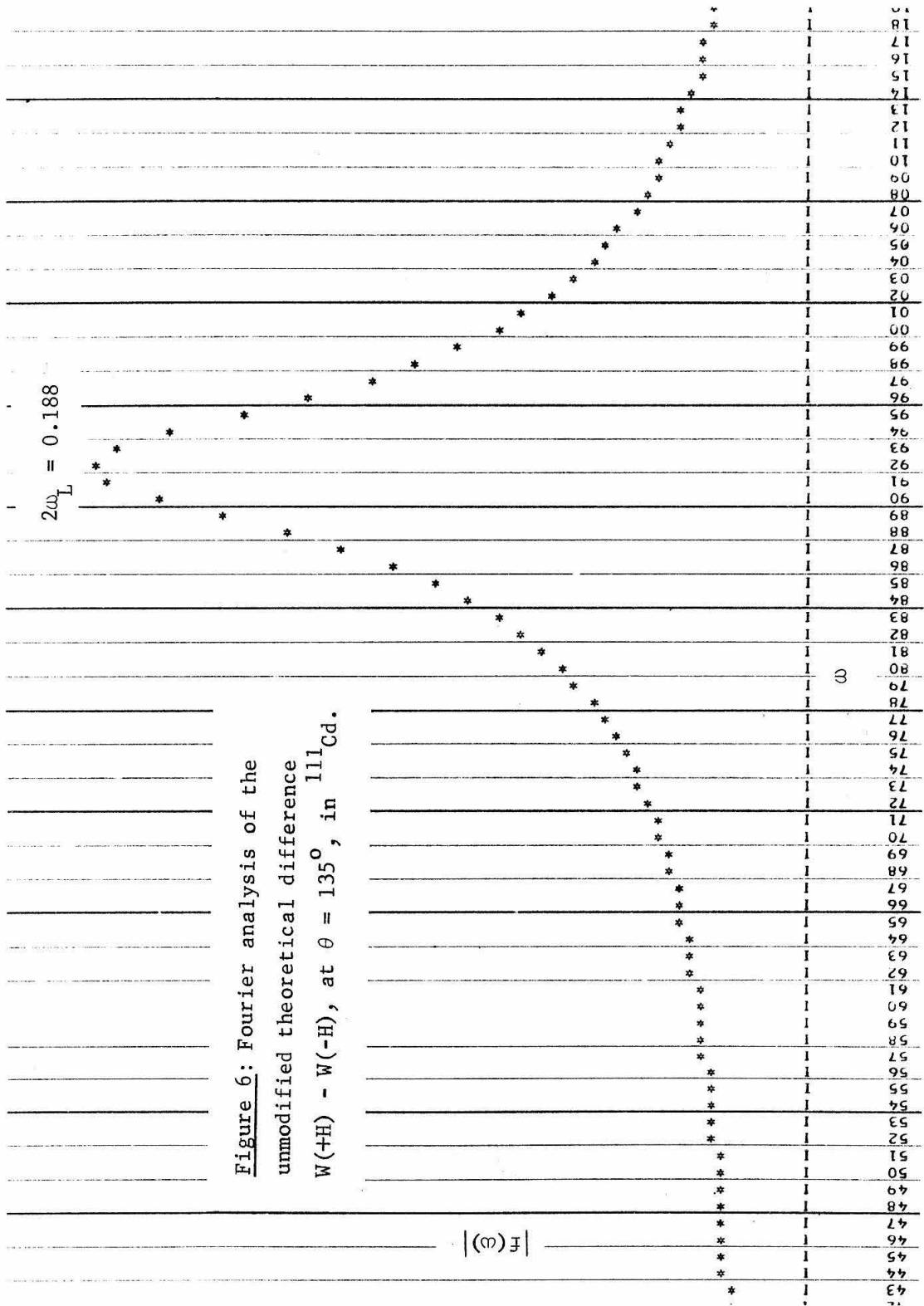


Figure 6: Fourier analysis of the unmodified theoretical difference $W(+H) - W(-H)$, at $\theta = 135^\circ$, in ^{111}Cd .

43
44
45
46
47
48
49
50
51
52
53
54
55
56
57
58
59
60
61
62
63
64
65
66
67
68
69
70
71
72
73
74
75
76
77
78
79
80
81
82
83
84
85
86
87
88
89
90
91
92
93
94
95
96
97
98
99
100
101
102
103
104
105
106
107
108
109
110
111
112
113
114
115
116
117
118
119
120

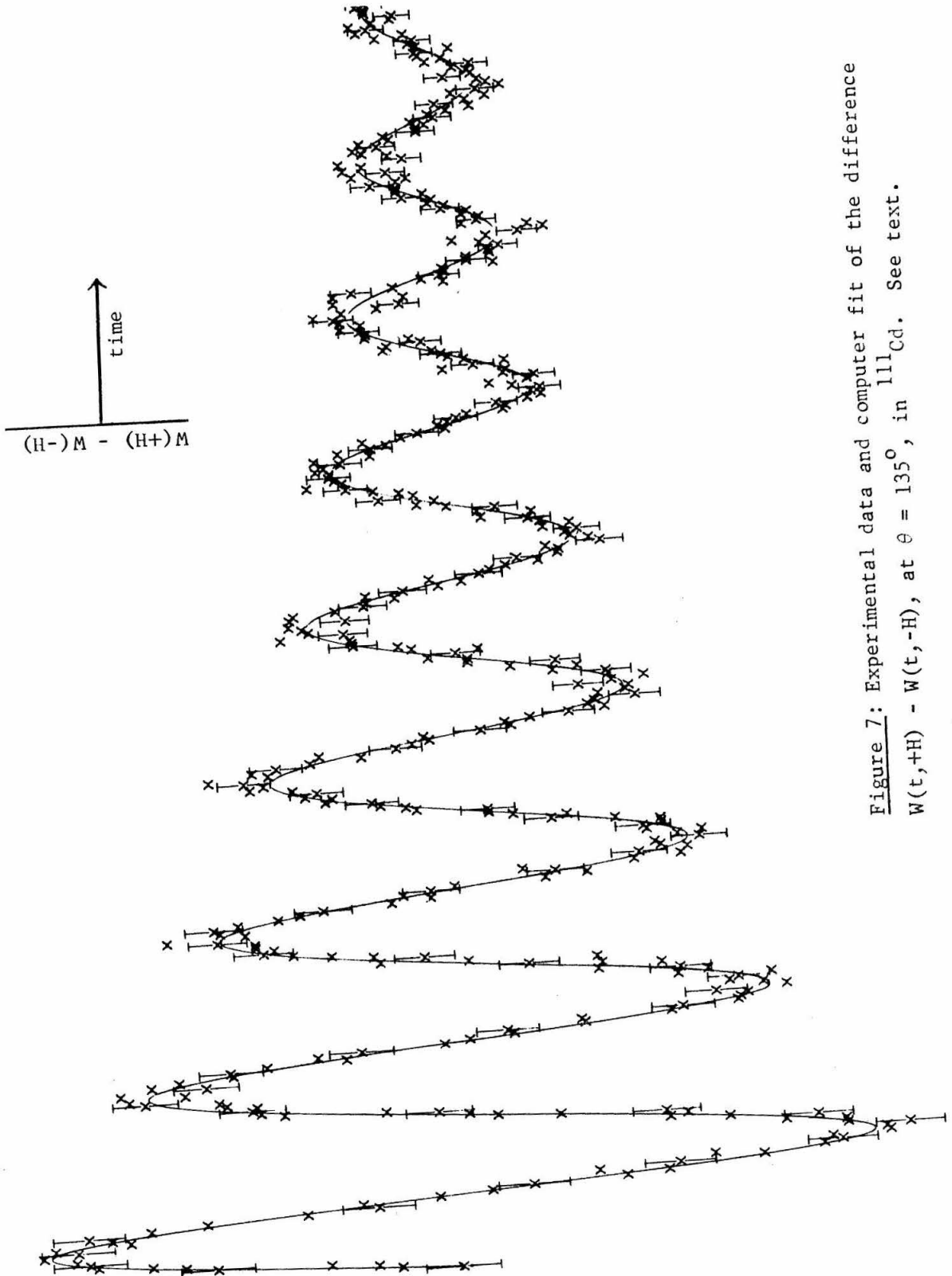


Figure 7: Experimental data and computer fit of the difference $W(t,+H) - W(t,-H)$, at $\theta = 135^\circ$, in ^{111}Cd . See text.

IBM SHARE No. 3094 program) and final results for the parameters were obtained (Fig. 7).

Runs at $\theta = \pi$ radians were analyzed to check for misalignment of the detectors and none was found. Also the sum $W(\theta, t, +H) + W(\theta, t, -H)$ was analyzed and compared with a decreasing exponential. No observable differential non-linearities in the system were found.

Fourier analysis of data from source 1, unannealed, revealed the existence of two fields. One at $2W_L = 0.188 \text{ ns}^{-1}$ ($H_{\text{eff}} = 61.7 \text{ kG}$) corresponding to the well-known field of 63.5 kG and another at $2W_L = 0.075 \text{ ns}^{-1}$ ($H_{\text{eff}} = 24.5 \text{ kG}$) with about 20% relative strength but of opposite polarity to the first.

Data from source 2, unannealed, yielded the main frequency only. However, several other frequencies, of weak strengths, both higher and lower than the main one, were observed.

Source 3 (same as source 2) was annealed for 2 1/2 hours at 800^oK. An analysis revealed one frequency only with no other peaks (except those due to the discreteness of the data). Fitted values of the mean life τ and the precession frequency of the 243 keV, $J^\pi = 5/2^+$ excited state were obtained with excellent agreement with earlier results. Table VIII.1 presents a summary of our results. We cannot, unfortunately, draw any definite conclusions regarding the 24.5 kG field, found in source 1. This source was not annealed and, in addition, was prepared by a different method than source 2. We therefore, merely point out that exchange effects (Sec. XII.2), can result in magnetic fields of opposite polarity, at two nuclei whose atoms are located at two different types of lattice sites.

TABLE VIII.1: Summary of precession measurements on ^{111}Cd in Ni

Fit	Source 1 one freq.	Source 1 two freq.	Source 2 (unannealed)	Source 3 (annealed)	Simms (Ref. 1)	Rietjens (Ref. 2)	Maier (Ref. 3)	Matthias (Ref. 4)
$\tau \times 10^9$ sec	125.4 ± 7.4	125.1 ± 6.5	122.0 ± 3.8	122.2 ± 2.0	$123.3^{+1.2}_{-0.8}$	123.0 ± 3.0	121.3 ± 0.7	-
$H_{hf} \times 10^{-3}$ gauss	$-(64.4 \pm 1.3)$ 25.0 ± 0.5	$-(64.2 \pm 1.3)$	$-(64.0 \pm 0.8)$	$-(63.9 \pm 0.8)$				65.3 ± 1

Note: The errors in H_{hf} are due almost entirely to the 1% uncertainty in the g-factor and the time calibration accuracy.

IX: THE INTERNAL MAGNETIC FIELDS AT Hg SITES IN Ni, Co AND Fe HOSTS

IX.1 Introduction

The internal magnetic fields acting at Hg nuclei embedded in Fe host lattice (Hg Fe), have been explored by Keszthelyi et al.⁵⁾ and by Murray et al.⁶⁾. The results reported by these authors; $H_{int} = -980$ kG and $H_{int} = -490$ kG, respectively, are in striking disagreement with each other. A re-examination of H_{int} (Hg Fe) seems important. At the same time a study of H_{int} (Hg Co) and H_{int} (Hg Ni) appears worthwhile since data on these two ferromagnets are not as abundant as data on impurities in Fe host lattices.

IX.2 Source Preparation and the Cascade

The 2.7 days source ^{198}Au was produced at the UCLA reactor via the reaction $^{197}\text{Au}(n,\gamma)^{198}\text{Au}$. The large neutron absorption cross section for ^{197}Au resulted in a high specific activity source. The activity of ^{198}Au in metallic form was deposited in pots made of 1.3 grams of pure (99.99%) Fe, Co and Ni. Tapered pins were driven into the pots under vacuum and the sealed pots were melted in an induction furnace in argon atmosphere. All samples had active concentration of less than 0.1 atomic percent.

From the decay scheme of ^{198}Au shown in Fig. 8 it is clear that only the one cascade, the $2^+(676 \text{ keV})2^+(412 \text{ keV})0^+$ is present and is rather weak as can be seen in the NaI energy spectrum displayed in Fig. 9. The measurements were performed using the integral-reverse-field method and the gamma rays were detected by two

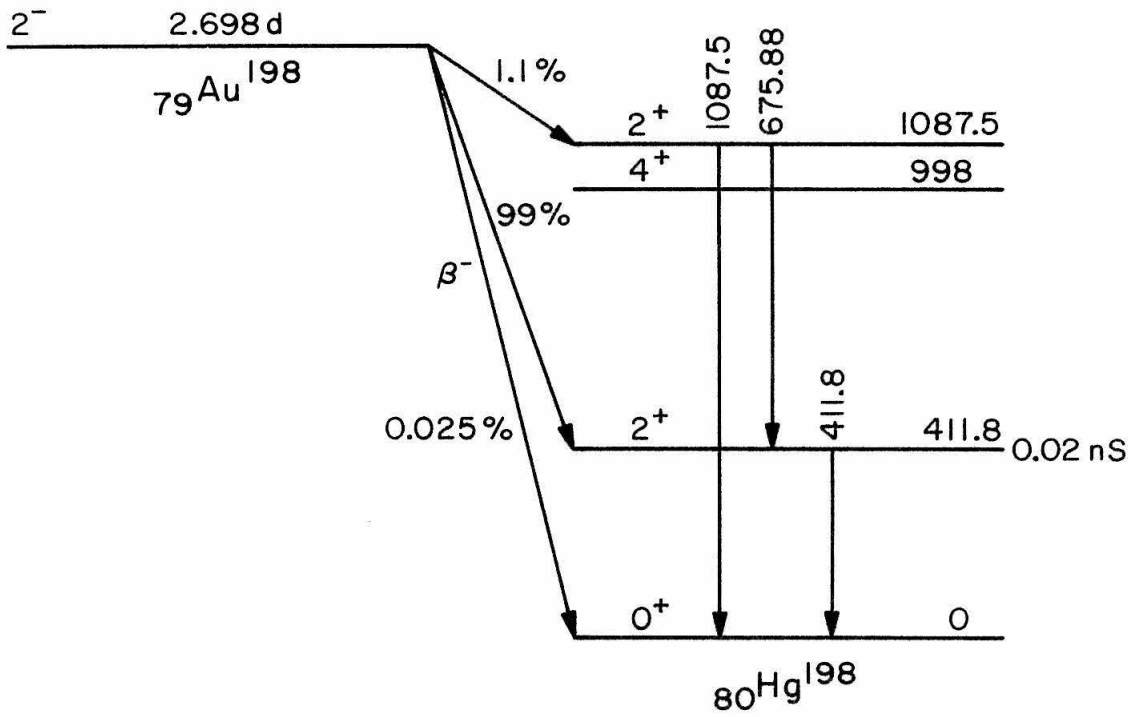


Figure 8

Decay scheme of $^{79}\text{Au}^{198}$ (Energies in keV)

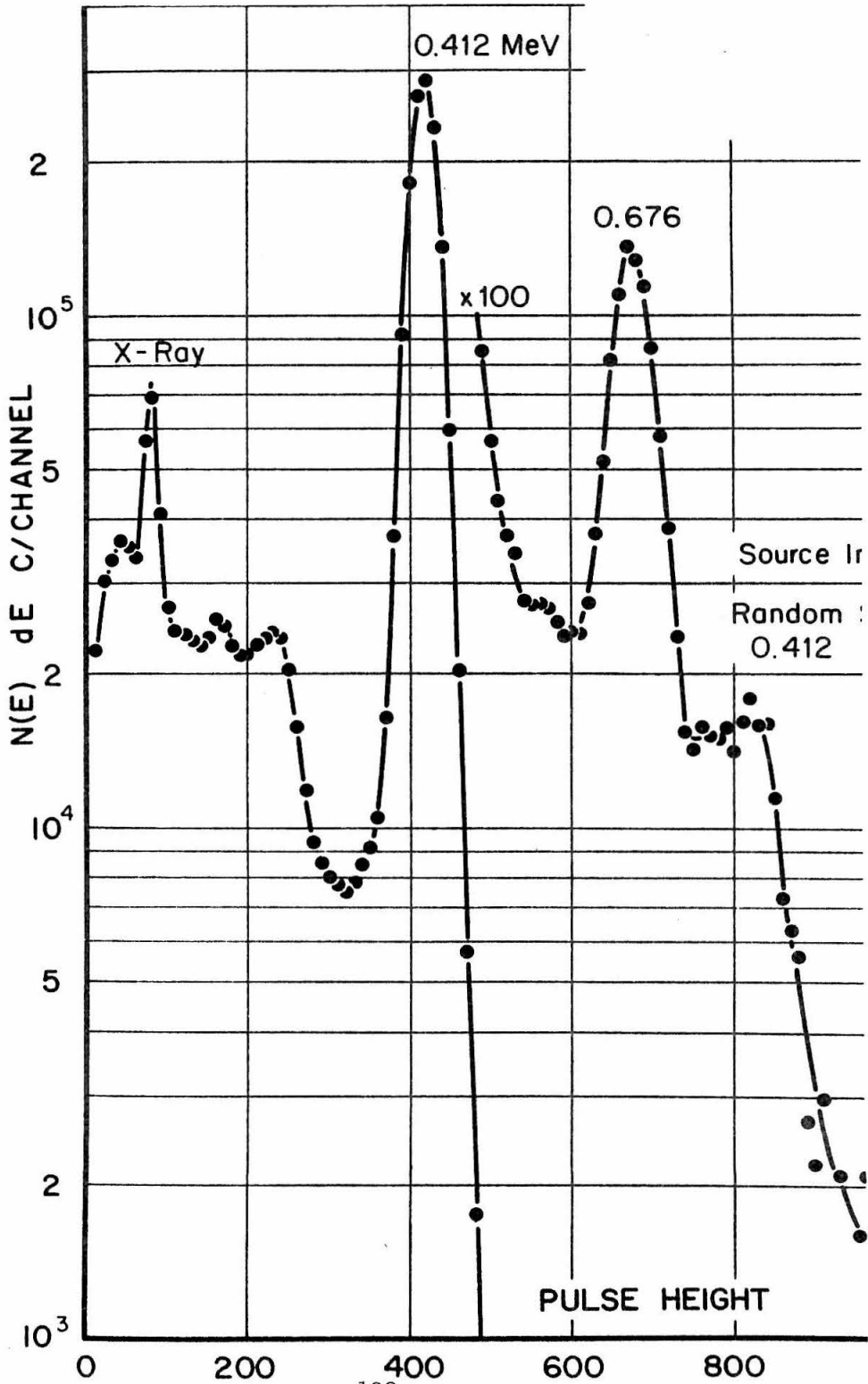


Figure 9: Energy spectrum of ^{198}Au decay taken with a 7.6 cm x 7.6 cm NaI scintillation counter.

7.6 cm x 7.6 cm NaI detectors. The experimental set-up was described earlier (Chapter III). The Fe and Ni ferromagnetic samples were aligned with an external magnetic field of $H_{\text{ext}} = 5$ kG and the Co source with a field of 18 kG.

IX.3 Results

The experimental angular correlation coefficients of the 676-412 keV cascade were found to be $A_2 = -0.253 \pm 0.005$ and $A_4 = 0.107 \pm 0.007$. Precession measurements were made at fixed angles 120° and 240° . At these angles the field-reversal ratio $R(\theta)$ reaches its largest absolute value. The internal magnetic fields were derived using the mean life and the g-factor of the first 2^+ state measured previously⁷⁾ $\tau = (3.15 \pm 0.15) \times 10^{-11}$ sec, $g_{2^+}({}^{198}\text{Hg}) = 0.55 \pm 0.11$. The results are:

Hg Ni source: $\omega_T = (6.8 \pm 2.1) \times 10^{-3}$ radians and $H_{\text{int}} = -(86 \pm 22)$ kG

Hg Co source: $\omega_T = (30.0 \pm 2.3) \times 10^{-3}$ radians and

$$H_{\text{int}} = -(370 \pm 78)$$
 kG

Hg Fe source: $\omega_T = (36.5 \pm 3.2) \times 10^{-3}$ radians and

$$H_{\text{int}} = -(440 \pm 105)$$
 kG.

The measured value of $H_{\text{int}}(\text{Hg Fe})$ is in agreement with the recent measurement $H_{\text{int}} = -(490 \pm 125)$ kG of Murray et al.⁶⁾. In addition, the internal magnetic fields experienced by the Hg nuclei embedded in the three ferromagnets show the expected proportionality between the induced fields on diamagnetic impurities and the magnetic moments of the host metals.

X THE HYPERFINE MAGNETIC FIELDS EXPERIENCED BY Tl NUCLEI IN THE FERROMAGNETS

X.1 Introduction

In Chapter IX, the magnetic hyperfine fields on Hg nuclei ($Z = 80$) in ferromagnetic hosts were found to be negative and of medium strength. In Pb, these fields are known⁸⁾ to be positive and also of medium strength. Since magnetic hyperfine fields on impurity nuclei in the ferromagnets have a definite trend in this region, it is safe to assume that the fields on Tl are small in magnitude. It is not possible yet, however, to even predict their sign. In fact, they may very well prove to be highly valuable in determining the parameters of hyperfine interaction theories, used to fit experimental results. At present, no such theories exist and even empirical formulae do not yield satisfactory predictions (Chapter XII). The measurements of the internal magnetic field on Tl in ferromagnetic hosts is therefore highly desirable both for the growing field of hyperfine interactions and for nuclear physics as a future nuclear probe.

X.2 Source Preparation

Of all the Tl isotopes, the only one which can be used with our present experimental set-up is ^{203}Tl . The parent ^{203}Pb ($T_{1/2} = 52$ hours) was obtained by using the reaction $^{203}\text{Tl}(d,2n)^{203}\text{Pb}$ on a Tl metal target. The Pb activity was separated from the Tl metal target in the following procedure. The sample was

dissolved in a minimum amount of HNO_3 . The solution was made basic through the addition of NH_4OH and a few milligrams of iron carrier were added. SO_2 gas was bubbled through the solution to change the valency of Tl to Tl^{+1} , and excess SO_2 was expelled by heating. Addition of concentrated H_2SO_4 precipitated the activity plus iron and the supernate was discarded. The iron carrier was removed by extraction with ethyl ether. The PbSO_4 activity was diluted in H_2O and put in a pot made of the desired ferromagnetic host. The sample was heated at 700°C in vacuum to convert PbSO_4 to PbO which was then reduced in H_2 gas at 200°C . The source was finally melted in an induction furnace. The above procedure was necessary since Pb has a very low melting point and previous attempts using carrier-free Pb activity failed upon melting of the source since all the activity evaporated before the ferromagnetic pot even started to melt. Even with our procedure about 70% of the activity was lost. Due to the larger solubility of Pb in Co than in Fe, the Pb Co source was stronger.

A sample of Tl in Fe was also prepared by using a different technique of source preparation. The PbO was dissolved in NH_3 and mixed with fine iron powder. This mixture was dried, reduced in H_2 , coined into the form of a small cylinder and annealed at 800°C for 12 h. This sample gave a field of -30 ± 30 kG. This is a smaller field than that obtained with the melted alloy and it appears that the sample has to pass through the molten phase in order to get the binary alloy.

X.3 The Gamma-Gamma Cascade and Results

The decay scheme of ^{203}Pb is shown in Fig. 10. The $5/2^+$ (401 keV) $3/2^+$ (279 keV) $1/2^+$ cascade was used in the measurements and the gamma rays were detected by two 7.6 cm x 7.6 cm integral line NaI spectrometers. The angular correlation coefficients for this cascade were measured to be $A_2 = -0.120 \pm 0.008$ and $A_4 = -0.015 \pm 0.012$ in the experimental geometry. Precession measurements were performed at fixed angles $\theta = \pm 3\pi/4$ radians between the detectors. Using $\tau = (4.05 \pm 0.06) \times 10^{-10}$ sec. and $g = 0.110 \pm 0.033$ for the 279 keV state reported by Ref. 7, the magnetic fields were found to be

$$H_{\text{int}}(\text{Tl } \underline{\text{Fe}}) = -185 \pm 70 \text{ kG}$$

$$H_{\text{int}}(\text{Tl } \underline{\text{Co}}) = -90 \pm 35 \text{ kG.}$$

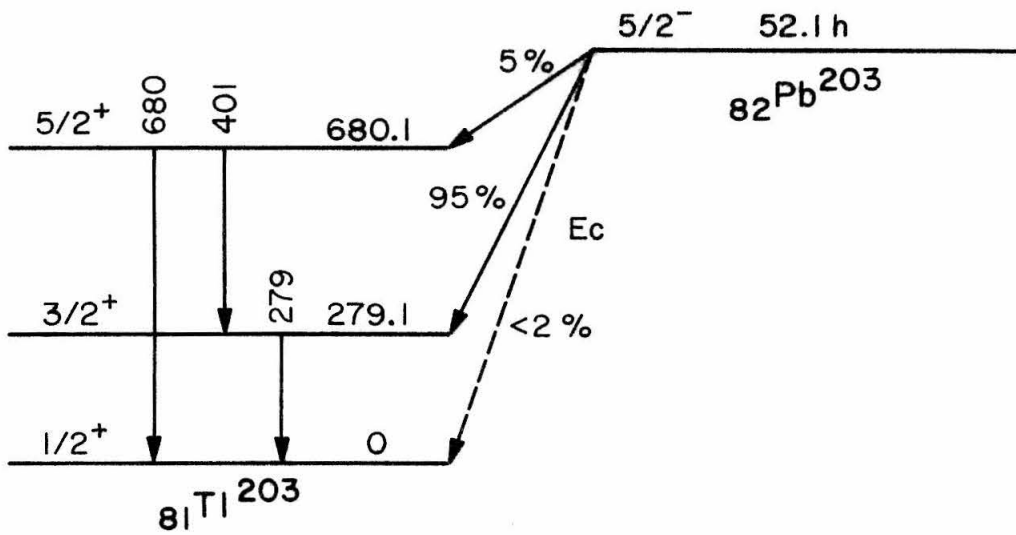


Figure 10

Decay scheme of $^{203}_{82}\text{Pb}$ (Energies in keV)

XI THE MAGNETIC MOMENT OF THE 50 keV, $3/2^-$ STATE IN ^{223}Ra AND THE
INTERNAL MAGNETIC FIELDS ACTING ON Ra NUCLEI DIFFUSED INTO FERRO-
MAGNETIC HOSTS

XI.1 Introduction

The hyperfine magnetic fields at the sites of impurity atoms diffused in ferromagnetic hosts have been observed to exhibit a frequent change of sign as a function of the atomic number of the impurity. This behavior can be qualitatively understood from the electron configuration of the impurity. It has recently been found that the field of radon⁹⁾ ($Z = 86$) in iron is positive, while the field of uranium¹⁰⁾ ($Z = 90$) in iron is negative. From systematics one does indeed expect a sign change in this region of atomic numbers. In addition, the hyperfine magnetic fields on "5d" impurity atoms diffused in Fe lattice should have a behavior similar to the fields observed on "4d" elements in the same host. In particular, the field on Ba in Fe has been recently reported to be $H_{\text{int}}(\text{Ba Fe}) = 0 \pm 100 \text{ kG}$ ¹¹⁾ and since Ra is the "5d" counterpart of the "4d" Ba (both terminate their respective series), a similar result in Ra seems likely.

XI.2 The Magnetic Moment of the $3/2^-$ State

From the partial level diagram of ^{223}Ra shown in Fig. 11 it is clear that a measurement on the $3/2^-$ state requires the use of Ge(Li) spectrometers. In addition, the only long-lived radioactive source is the 21.6 years ^{227}Ac which β decays to ^{227}Th ($T_{1/2} = 18.2$ days). The levels in ^{223}Ra are directly populated via the

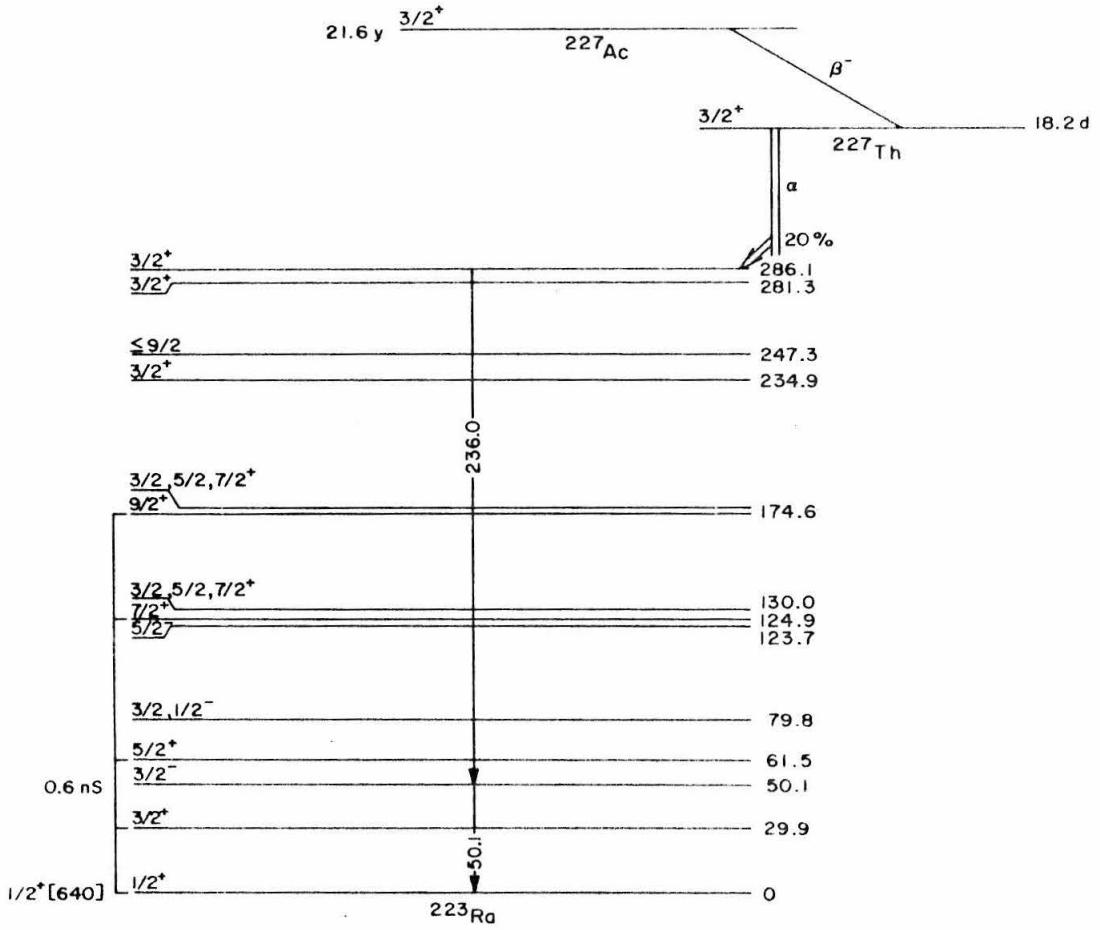


FIGURE 11
 ^{227}Ac partial decay scheme

α -decay of ^{227}Th . ^{223}Ra itself is not stable ($T_{1/2} = 11.43$ days) being part of the actinium decay series which terminates with ^{207}Pb . A Ge(Li) energy spectrum of the decay of ^{227}Ac is shown in Fig. 12.

The measurement was performed using the integral-reverse-field method and the gamma rays were detected by two 5 cm^3 planar Ge(Li) detectors. Angular correlation measurements were performed on a liquid source made of carrier-free ^{227}Ac activity in dilute solution of HNO_3 which was put in a small plastic container. The $3/2^+(236\text{ keV})3/2^-(50\text{ keV})1/2^+$ cascade used in the measurement, yielded the angular correlation coefficients (corrected for geometry) $A_2 = -0.205 \pm 0.005$ and $A_4 = 0$. These values are in agreement with previous measurements¹²⁾ and indicate that time-dependent quadrupole interactions that could attenuate the correlation during the relatively long life of the intermediate state are not present. The mean life of this state $\tau = (0.91 \pm 0.10) \times 10^{-9}\text{ sec}$ ¹³⁾ made it possible to measure the magnetic moment with an external magnetic field of $H_{\text{ext}} = 28.0\text{ kG}$. The integral-reverse-field method was used in the precession measurement and the mean precession angle $\omega\tau = 0.034 \pm 0.003$ radians for the 50 keV state was obtained from the field reversal ratio $R(\theta)$ at $\theta = 3\pi/4$ radians. Using these results, the magnetic moment of the $3/2^-$ state was found to be

$$\mu(50\text{ keV}, 3/2^-) = 0.56 \pm 0.08\text{ nm.}$$

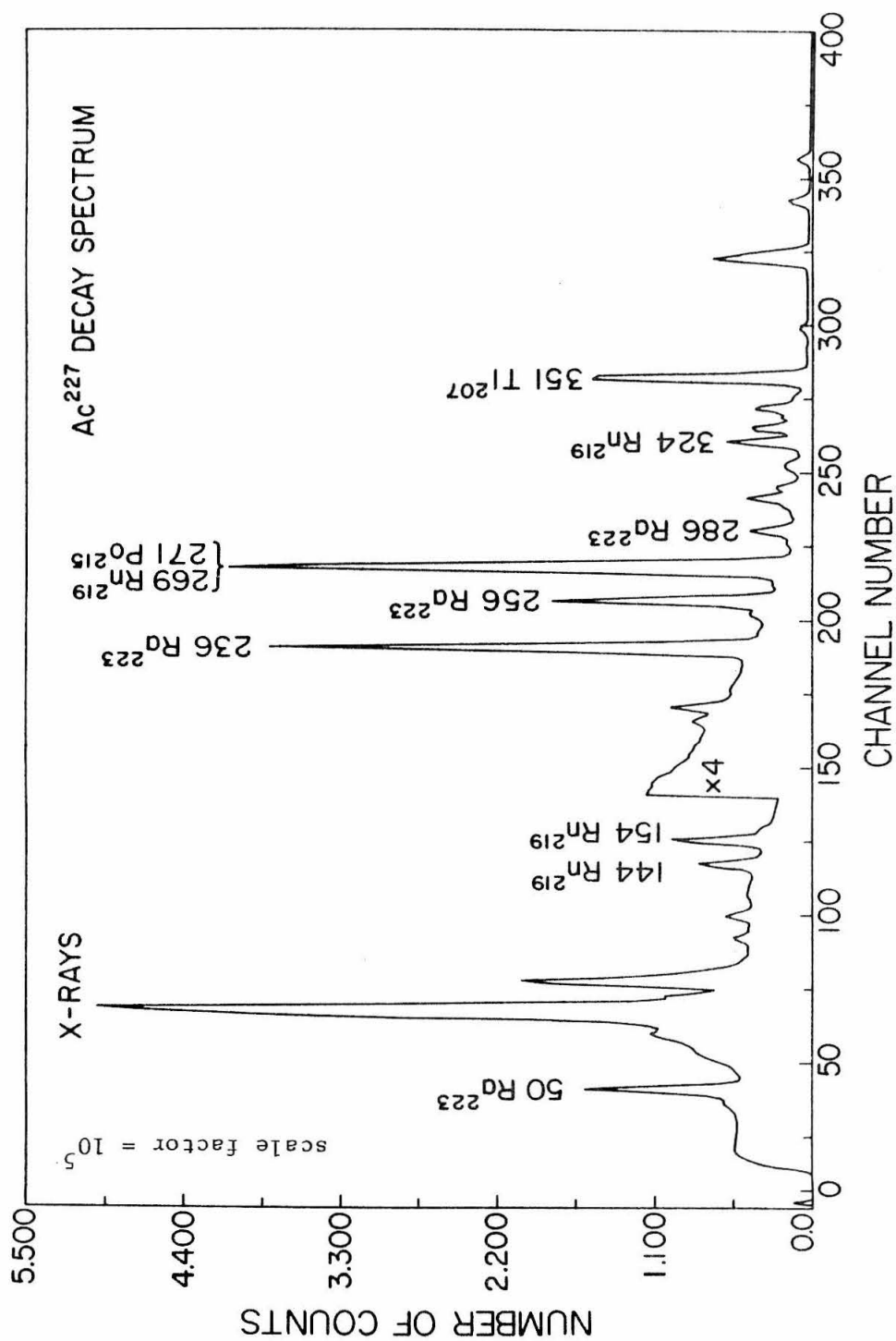


Figure 12: Ge(Li) energy spectrum of ²²⁷Ac.

XI.3 Preparation of Ferromagnetic Sources

The dilute alloys of Ac with the ferromagnets were prepared by depositing the carrier-free ^{227}Ac activity in dilute HNO_3 on ~ 80 mg of powder of pure Fe, Co or Ni metals. The mixtures were washed with water, dried and reduced in hydrogen. The reduced powders were coined into small cylinders under a pressure $\sim 10^3$ atm. In a second step the cylinders were rolled into thin foils (~ 0.3 mm thickness) and annealed for 5 h at 800°C . All alloys had less than 0.01 atomic percent of Ac. The necessity for use of thin foils is explained in Appendix B in which the effects of source thickness on angular correlation measurements are described. This is particularly important in the present case which involves a very low energy line (50 keV) and a relatively low gamma ray (the 236 keV line).

XI.4 Experimental Techniques and Results

The hyperfine magnetic field in the Ra Ni source was measured using the integral-reverse-field method while the Ra Co and Ra Fe sources were investigated by both the integral-reverse-field and the integral rotation methods. The metallic foil sources were polarized by an external magnetic field; the Ni and Fe alloys were aligned with a field $H_{\text{ext}} = 3$ kG while a field of $H_{\text{ext}} = 18$ kG was needed to saturate the Co source. The hyperfine fields quoted below have been corrected for the external aligning fields. The experimental procedure was the same as for the liquid source, but both detectors were moved closer to the source to increase the coincidence rate. In all cases the angular correlation coefficient A_4 was

found to be $A_4 \simeq 0$ within experimental errors as is expected theoretically. The results are:

Liquid source: $A_2 = -0.12 \pm 0.004$

Ra Ni source: $A_2 = -0.10 \pm 0.005$ and $\omega_T = 0.035 \pm 0.010$ radians

Ra Co source: $A_2 = -0.08 \pm 0.004$ and $\omega_T = 0.076 \pm 0.013$ radians

Ra Fe source: $A_2 = -0.07 \pm 0.004$ and $\omega_T = 0.125 \pm 0.016$ radians.

Using these results and the magnetic moment of the $3/2^-$ state reported above, the following internal magnetic fields were obtained:

$$H_{\text{int}}(\text{Ra } \underline{\text{Ni}}) = -30 \pm 10 \text{ kG}$$

$$H_{\text{int}}(\text{Ra } \underline{\text{Co}}) = -80 \pm 16 \text{ kG}$$

$$H_{\text{int}}(\text{Ra } \underline{\text{Fe}}) = -105 \pm 20 \text{ kG.}$$

It is of interest to note that all the metallic sources yielded angular correlations which are attenuated with respect to the angular correlation of the liquid source. These attenuations are larger than the expected attenuation factor of $1/\sqrt{1 + (2\omega_T)^2}$ due to magnetic hyperfine interactions. This discrepancy disappears if one takes into account the scattering of the low energy gamma rays in the cascade. This mechanism could also explain the small differences in the correlation observed for the three ferromagnetic sources. However, since there seem to exist slightly larger attenuations on going from the Ni through Co, to the Fe sources, it is also possible that small quadrupole interaction is present in the host lattices. In fact, since alpha decay populates ^{223}Ra , it is indeed possible that the cubic symmetry usually enjoyed by these

ferromagnetic lattices is disturbed. Also, it may cause the radioactive nuclei to recoil out of substitutional sites into interstitial ones in which case they will experience different internal fields. On the other hand it is known that the radius of a radium atom is much larger than the radii of any of the ferromagnetic host atoms. As a result, ordinary diffusion techniques are not capable of embedding the radium impurity in any of the host lattices. The alpha decay of ^{227}Th is then actually helpful in implanting the active radium atoms into the ferromagnetic lattices. Also, the appreciable difference between the radius of the impurity atoms and the radii of the host atoms causes the impurity atoms to be implanted preferentially in substitutional sites where the lattice spacing is the largest.

XII DISCUSSION OF EXPERIMENTAL RESULTS

XII.1 Summary of Experimental Results

The hyperfine magnetic fields experienced by the nuclei of Cd, Hg, Tl and Ra atoms, embedded in ferromagnetic lattice hosts, are summarized in Table XII.1.

The measurement on Cd is in good agreement with the earlier measurement of Matthias et al.⁽⁴⁾ The appearance of a satellite field of opposite polarity is inconclusive. However, our analysis reveals the necessity for caution in data analysis. The discrete nature and finite time-interval of the experimental data introduce spurious frequency components into the time-differential measurement. These can best be seen in our Fourier analysis (Figs. 3-6) and very likely mask a whole distribution of internal magnetic fields, which in some cases may be significant. Data fitting by theoretical expressions, modified to duplicate experimental conditions, should prove useful in overcoming these difficulties. In addition, there are cases in which the mean life of the investigated state is comparable to the time resolution of the experimental system. These can then be measured by the highly sensitive time-differential technique rather than by insensitive time-integral techniques. Appendix A presents such a modified function. The lifetime of the $5/2^-$ state in ^{111}Cd , measured by us, agrees well with previous measurements and reflects the accuracy of this method.

The measurements on Hg indicate that the internal field of Hg in Fe, reported by Keszthelyi et al.⁵⁾ is incorrect, being too high

TABLE XII.1

Alloy	$\omega\tau$ (m rad.)	g-factor	τ (nsec)	H_{int} (kG)
<u>Cd Ni</u>	$\omega = 0.099 \text{ nsec}^{-1}$	- (0.315 \pm 0.003)		- (64.0 \pm 0.8)
<u>Hg Fe</u>	+ (36.5 \pm 3.2)	{ 0.55 \pm 0.11 }	{ 0.0315 \pm 0.0015 }	- (440 \pm 105)
<u>Hg Co</u>	+ (30.0 \pm 2.3)			- (370 \pm 78)
<u>Hg Ni</u>	+ (6.8 \pm 2.1)			- (86 \pm 22)
<u>Tl Fe</u>	+ (40 \pm 10)	{ 0.110 \pm 0.033 }	{ 0.405 \pm 0.006 }	- (185 \pm 70)
<u>Tl Co</u>	+ (15 \pm 4)			- (90 \pm 35)
<u>Ra Fe</u>	+ (125 \pm 16)	{ 0.28 \pm 0.04 }	{ 0.91 \pm 0.10 }	- (105 \pm 20)
<u>Ra Co</u>	+ (76 \pm 13)			- (80 \pm 16)
<u>Ra Ni</u>	+ (35 \pm 10)			- (30 \pm 10)

by approximately a factor of 2. The internal fields of Hg in Co and Ni are found to be in reasonable agreement with the prediction that these fields should be proportional to the magnetic moment of the host atoms.

The magnetic hyperfine fields of Tl and Ra in ferromagnetic hosts are small as expected from systematics. In Ra, these fields have indeed changed sign in going from Ra to U. Again the proportionality between the fields and the host's moments is observed.

XII.2 Status of Theoretical Investigations

The Hamiltonian for the magnetic interaction between a single electron and the nuclear magnetic moment is given by

$$H = - g_0 g_N \mu_0 \mu_N \left\{ \frac{8\pi}{3} \delta(\vec{r}) \vec{S} \cdot \vec{I} + \frac{(\vec{L} - \vec{S}) \cdot \vec{I}}{r^3} + \frac{3(\vec{S} \cdot \vec{r})(\vec{I} \cdot \vec{r})}{r^5} \right\} \quad (\text{XII.1})$$

where g_0 and g_N are the electronic and nuclear g-factors, μ_0 and μ_N are the Bohr and nuclear magnetons and \vec{L} , \vec{S} , and \vec{I} represent, respectively, electron orbital, electron spin, and nuclear spin angular momentum operators. The first term, which is called the Fermi contact term⁽¹⁴⁾ is non-zero only for s electrons, in which case the last two terms are zero. These two terms are dipolar interaction terms. The interaction Hamiltonian can also be written in the form

$$H = - \vec{\mu}_I \cdot \vec{H}_J \quad (\text{XII.2})$$

where $\vec{\mu}_I$ is the nuclear magnetic moment and \vec{H}_J is the magnetic field at the nucleus of the atom having total angular momentum J.

For a single electron (or a single hole in closed shell) with $L \neq 0$, Eq. (XII.1) can be replaced by the operator

$$H' = -g_0 g_N \mu_0 \mu_N \frac{\vec{I} \cdot \vec{J}}{J(J+1)} \left[\frac{L^2}{r^3} - \frac{S^2}{r^3} + \frac{3(\mathbf{S} \cdot \mathbf{r})^2}{r^5} \right] \quad (\text{XII.3})$$

where use was made of the fact that only the components of \vec{L} and \vec{S} along \vec{J} contribute to the average value. The last two terms cancel each other on taking the average, leaving only the orbital term. The orbital angular momentum is quenched, in most cases, by the crystal field so that it usually does not contribute to the interaction. Exceptions are the "4f" ions in the rare-earth region.

For atoms with unpaired s electrons, the field at the nucleus arises only from the contact part of the Hamiltonian. This field is

$$\vec{H}_c = \frac{8\pi}{3} g_0 \mu_0 \vec{S} |\psi_s(0)|^2 \quad (\text{XII.4})$$

where $|\psi_s(0)|^2$ is the density of the s electrons at the nucleus.

For atoms with a net spin but no unpaired s electrons, the above one-electron theory predicts zero hyperfine magnetic fields, whereas large fields were observed for such cases. It was then suggested by Sternheimer¹⁵⁾ that the polarization of the core electrons by the spin of the outer electrons would produce a net unpaired spin density at the nucleus. This would result then in a hyperfine magnetic field via the Fermi contact term. The best treatment of this core polarization effect is supplied by the unrestricted Hartree-Fock method. It is identical to the conventional Hartree-Fock method, except that the radial part of an orbital wave function is allowed to depend on

the magnetic quantum number " M_s " within an " n, l " shell. Thus orbitals of spin "up" and spin "down" may differ in their spatial behavior resulting in a net spin-density at the nucleus. This difference is a consequence of the exchange interaction which affects only electrons with spin parallel to the net spin of the atom. The exchange interaction acts as an attractive interaction for parallel spins though actually it is a reduction in electrostatic repulsion due to the exclusion principle. Thus, all inner s electron shells are exchange polarized by outer electrons and contribute to net spin-density at the nucleus. A detailed discussion of core polarization is given in Ref. 16.

In a ferromagnetic lattice, the nucleus of a normally diamagnetic impurity atom will experience magnetic fields due to two possible mechanisms. These are conduction-electrons polarization and core-polarization, both producing a net spin-density at the nucleus. Direct overlap of the "3d" spin-density from neighboring ferromagnetic atoms is small.

Conduction-electrons polarization is produced by exchange interactions of the magnetic electrons on the ferromagnetic atoms with s-type conduction bands, thus producing a field at the nucleus via the Fermi contact term. This polarization is partially ordinary exchange polarization described above. It is also partially due to the Ruderman-Kittel-Kasuya-Yosida exchange interaction which arises from the effects of local electronic magnetic moments on the conduction electron spin distribution.

Core polarization is produced by exchange interaction with neighboring ferromagnetic atoms. It can be also produced by interaction with polarized conduction bands. The outer electrons of the impurity atom are first exchange polarized and contribute a field at the nucleus through the Fermi contact term, or by core-polarizing the inner electron shells.

In the above, only a few of the possible interactions were mentioned. Their contributions to hyperfine magnetic fields vary in signs and magnitudes and even qualitative treatments have not been satisfactory. In fact, simple unrestricted Hartree-Fock calculations were performed only for free ions⁽¹⁶⁾. It is therefore of interest to describe the empirical systematics displayed by these fields.

These systematics are:

- (i) Proportionality of the magnetic field at the nucleus of the impurity atom to the effective magnetic moment of the host atoms (2.2, 1.7, and 0.6 for Fe, Co, and Ni, respectively). This law holds for the majority of known cases, including our recent results.
- (ii) Dependence of the magnetic field on the number of electrons in the outer shells of the impurity atom. Within one period, the fields follow a definite pattern displayed in Fig. 13. Our measurements on Hg, Tl, and Ra fit well into this pattern for the "5d" period.
- (iii) Dependence of the magnetic field on the number of the periodic group. The value of the magnetic field increases with the number of the period.

These systematics are obeyed in most cases, with very few ex-

ceptions (disregarding the rare-earth elements). Based on these systematics, Shirley and Westenbarger⁽¹⁸⁾ suggested that conduction electron polarization may be the major contributing mechanism to magnetic fields at diamagnetic atoms in ferromagnetic hosts. Balabanov and Delyagin⁽¹⁹⁾ very recently arrived at the conclusion that core polarization is the major mechanism. The confusion does not end there, since both descriptions are inaccurate. For instance, Shirley and Westenbarger predict large positive field for Ba in Fe whereas the measured field is very small and possibly negative. Balabanov and Delyagin predict positive fields for Ra in the ferromagnets, while our measurements indicate small but negative fields.

Finally, we would like to point out that although interest in hyperfine interactions of impurities has been growing in recent years, it is by no means a widely investigated phenomenon. The solid state theorists would rather deal with perfectly regular lattices while nuclear physicists are only interested in using hyperfine fields to probe the nucleus. However, putting the same impurity in several host lattices and putting several impurities in the same host lattice should yield valuable information about the solid state. This has been done for semiconductors, resulting in the modern era of semiconductor devices. The use of hyperfine interactions could result in a better understanding of electric and magnetic properties of solids.

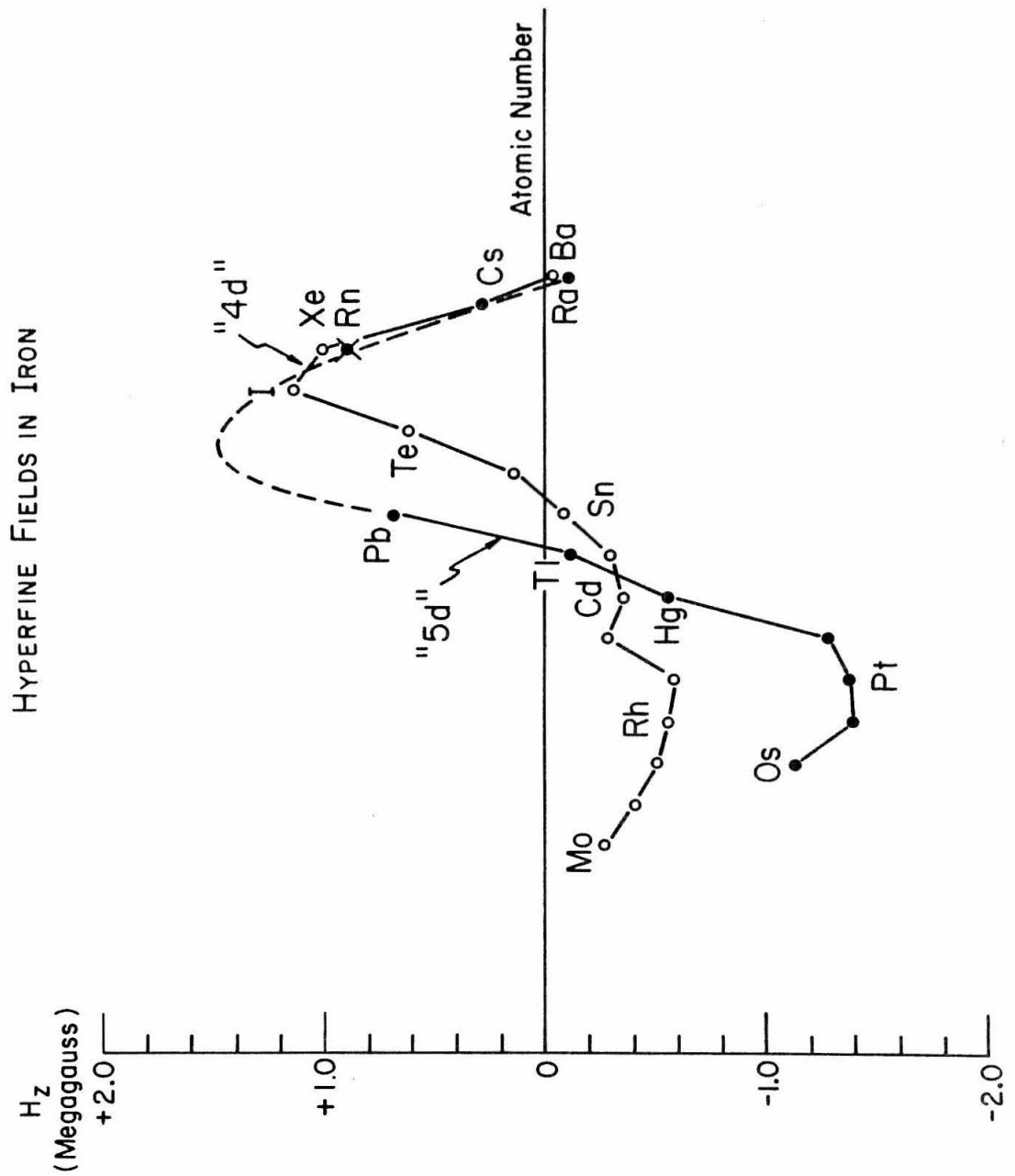


Figure 13: Hyperfine magnetic fields of "4d" and "5d" series elements in Fe.

APPENDIX A

ANALYSIS OF TIME-DIFFERENTIAL PERTURBED ANGULAR CORRELATION MEASUREMENTS

A.1 Introduction

The method of time-differential perturbed angular correlation, has been used for some time as a nuclear and solid-state probe. It makes possible accurate measurements of magnetic and electric moments of excited state of nuclei, which are not accessible to other methods. Spin assignments and in some cases mixing ratios of gamma rays have been determined by this method. Lately this method has been increasingly used, not only in determining magnetic hyperfine interactions in solids, but also in measuring time relaxation phenomena and other time-dependent interactions in solids.

Differential measurements have several advantages over integral ones. They yield more information with much higher accuracy than integral measurements. Experimentally they are easier to perform since both detectors are stationary and a separate timing/switching control system is not necessary.

On the other hand, differential measurements are much more sensitive to fluctuations in the time-response of the coincidence system, because the correlation pattern is observed directly as a function of the delay between the emission of the two gamma-rays in the investigated cascade.

In the following, an expression for the observed differential perturbed correlation is obtained. It takes into account time-fluctuations in the response of the various components of the

correlation apparatus, i.e., it describes the probability that the experimental system will introduce extra delay into the true delay time, which will result in the information being stored in a certain channel of a multichannel analyzer.

The treatment is divided into several steps:

1. The theoretical expression is presented and the various parameters are described. Effects such as scattering in the source and surrounding material and of the finite solid angles subtended by the detectors, are assumed to be included in the angular-correlation coefficients. Correction tables are available for finite solid angle effects and scattering effects can be minimized by making the source dimensions small.

2. The response of the two detector systems is evaluated, both in the time and frequency domains. It is assumed that the response of each detector is Poisson distributed with a characteristic decay constant. This description specifically applies to scintillation counters, however, it also applies to solid-state counters to a high degree of accuracy.

3. Time-dispersion in the 'electronics' section of the apparatus is described both in the time and frequency domains. Here, the 'electronics' section includes the various electronic components which relay the timing information from the detectors, until this information is stored away. These usually include phototubes (for scintillation counters), preamplifiers, fast amplifiers, fast triggers and a time-to-amplitude converter. The normal distribution is assumed for the time-dispersion curve.

4. The total response of both the detectors' section and the electronics section is then calculated by folding the two distributions in the time domain, and by using the convolution theorem in the frequency domain.

5. The results of the previous step are then used to obtain an expression for the perturbed angular correlation just before it is stored away.

6. The effects of finite time-widths of the various channels in which information is stored are taken into account, assuming each channel to have a rectangular shape. The final, discrete expression for the observed perturbed correlation is then derived.

7. The importance of the various terms in the modified correlation expression is discussed.

8. Simplified versions of the observed correlation, which pertain to specific cases (of experimental importance) are described.

A.2 The Theoretical Expression

The theoretical expression obeyed by time differential, perturbed angular correlation is given by (Sec. II.3)

$$W(t) = \lambda e^{-\lambda t} \{ 1 + A_2 e^{-\lambda_2 t} P_2[\cos(\theta - \omega_L t)] \\ + A_4 e^{-\lambda_4 t} P_4[\cos(\theta - \omega_L t)] \} U(t)$$

where

$\lambda = \frac{1}{\tau}$ = decay constant of intermediate state.

A_2, A_4 = angular correlation coefficients.

λ_2, λ_4 = attenuation coefficients.

$P_2(x), P_4(x)$ = Legendre polynomials of 2nd and 4th order.

θ = constant angle between detectors' directions.

ω_L = Larmor frequency of precession.

t = time delay between the emission of the first and second gamma rays in the investigated cascade.

$U(t) = \begin{cases} 0 & t < 0 \\ 1/2 & t = 0 \\ 1 & t > 0 \end{cases}$ unit step function.

The first term in the product is the probability (density) that the intermediate state will decay via the second gamma ray at time 't' after being populated at time $t = 0$ by the first gamma ray in the cascade.

The term in parentheses is the perturbed angular correlation expression and is proportional to the probability that at time t after the emission of the first gamma ray, the second gamma ray will be emitted at an angle $(\theta - \omega_L t)$ with respect to the direction of

emission of the first. The attenuation coefficients λ_2 and λ_4 are related to time dependent interactions due to fluctuations in magnetic or electric fields experienced by the nucleus in its intermediate state.

The unit step function $U(t)$ insures that the emission of the second gamma-ray in the cascade will occur after the emission of the first.

A.3 Time-Dispersion in the Detector System

If the two gamma rays in the cascade reach the two scintillators simultaneously (and according to Poisson statistics, simultaneous emission of the two gamma rays is the most probable case), the information they carry will not necessarily be transmitted simultaneously to the next respective stages since each scintillator has a characteristic lifetime. Let α_1 and α_2 be the characteristic decay constants of the scintillators accepting the first and second gamma rays, respectively. The probability that the information carried in the second will suffer a time delay T with respect to the first, in the scintillators, is given by

$$D(T) = \int_{-\infty}^{\infty} [\alpha_1 e^{-\alpha_1(t' - T)} U(t' - T)] [\alpha_2 e^{-\alpha_2 t'} U(t')] dt' = \frac{\alpha_1 \alpha_2}{\alpha_1 + \alpha_2} \begin{cases} e^{\alpha_1 T} & T < 0 \\ e^{-\alpha_2 T} & T > 0 \end{cases} .$$

The first and second terms in the integrand are the probabilities that the information carried in the first and second gamma rays will suffer time delays of $(t' - T)$ and t' , respectively, so that the

delay of the second with respect to the first is $t' - (t' - r) = T$. The summation is over all combinations which result in total delay of T . In the above derivation of time dispersion in the scintillators, it was assumed that the two gamma rays entered the detectors simultaneously. Obviously the result is still true in the general case where T now denotes the extra delay in relaying the information carried in the two gamma rays.

It will be useful later to know also the Fourier transform of the time dispersion caused by the detectors.

$$D(\omega) = \frac{\alpha_1 \alpha_2}{\alpha_1 + \alpha_2} \left\{ \int_{-\infty}^0 e^{(\alpha_1 + i\omega)t} dt + \int_0^{\infty} e^{(-\alpha_2 + i\omega)t} dt \right\} =$$

$$= \frac{\alpha_1 \alpha_2}{\alpha_1 + \alpha_2} \left(\frac{1}{\alpha_1 + i\omega} + \frac{1}{\alpha_2 - i\omega} \right).$$

A.4 Time-Dispersion in the "Electronics" Section

Information concerning the time dispersion occurring in the various electronic components which relay the necessary timing pulses from the detectors to the multichannel analyzer is nonexistent. Assuming random fluctuations and in accord with the central-limit theorem of statistics, the time dispersion in the electronics is taken to be Gaussian distributed about the initial delay so that the probability of extra delay, between the two timing pulses, due to the electronics is given by

$$E(t) = \frac{1}{\sqrt{2\pi} \sigma} e^{-\frac{t^2}{2\sigma^2}}$$

and in the frequency domain

$$E(\omega) = \frac{1}{\sqrt{2\pi} \sigma} \int_{-\infty}^{\infty} e^{-\left(\frac{t^2}{2\sigma^2} - i\omega t\right)} dt = e^{-\frac{\sigma^2}{2} \omega^2}$$

where σ = width of the distribution.

A.5 Total Response of the Detector Plus "Electronics" Sections

In order to obtain an expression for the total time dispersion in both the detectors and the electronics, it is necessary to convolute the two distributions, i.e., sum over all different combinations of delays which result in a certain total delay t between the two timing pulses. This probability is given by

$$\begin{aligned} P(t) &= \int_{-\infty}^0 D(T)E(t - T)dT = \frac{\alpha_1\alpha_2}{\sqrt{2\pi} \sigma(\alpha_1 + \alpha_2)} \left\{ \int_{-\infty}^0 e^{-\frac{(t-T)^2}{2\sigma^2}} e^{-\alpha_1 T} dT + \right. \\ &\quad \left. + \int_0^{\infty} e^{-\frac{(t-T)^2}{2\sigma^2}} e^{-\alpha_2 T} dT \right\} \\ &= \frac{\alpha_1\alpha_2}{2(\alpha_1 + \alpha_2)} \left\{ e^{\left(\frac{\alpha_1^2 \sigma^2}{2} + \alpha_1 t\right)} \operatorname{erfc} \left(\frac{\alpha_1 \sigma}{\sqrt{2}} + \frac{t}{\sqrt{2} \sigma} \right) + e^{\left(\frac{\alpha_2^2 \sigma^2}{2} - \alpha_2 t\right)} \right. \\ &\quad \left. \operatorname{erfc} \left(\frac{\alpha_2 \sigma}{\sqrt{2}} - \frac{t}{\sqrt{2} \sigma} \right) \right\} \end{aligned}$$

where, $\operatorname{erfc}(x) = \frac{2}{\sqrt{\pi}} \int_x^{\infty} e^{-u^2} du$ = complimentary error function.

In the frequency domain, use of the convolution theorem yields immediately

$$P(\omega) = D(\omega)E(\omega) = \frac{\alpha_1 \alpha_2}{\alpha_1 + \alpha_2} e^{-\frac{\sigma^2}{2} \omega^2} \left(\frac{1}{\alpha_1 + i\omega} + \frac{1}{\alpha_2 - i\omega} \right).$$

A.6 The Modified Perturbed Correlation Function

It is now possible to calculate the dispersion effects, in the correlation apparatus, on the angular correlation pattern. Again it is necessary to convolute the two distributions. The calculation is simplified considerably if use is made of the convolution theorem, i.e.,

$$W'(t) = \int_{-\infty}^{\infty} W(t')P(t - t')dt' \Rightarrow W'(\omega) = W(\omega)P(\omega).$$

Now,

$$\begin{aligned} W(\omega) = \int_{-\infty}^{\infty} W(t)e^{i\omega t} dt = & \lambda \left\{ \frac{1}{\lambda - i\omega} + \frac{A_2}{8} \left[\frac{3e^{2i\theta}}{\lambda + \lambda_2 - i(\omega - 2\omega_L)} + \right. \right. \\ & \left. \left. + \frac{3e^{-2i\theta}}{\lambda + \lambda_2 - i(\omega + 2\omega_L)} + \frac{2}{\lambda + \lambda_2 - i\omega} \right] \right. \\ & + \frac{A_4}{128} \left[\frac{35e^{4i\theta}}{\lambda + \lambda_4 - i(\omega - 4\omega_L)} + \frac{35e^{-4i\theta}}{\lambda + \lambda_4 - i(\omega + 4\omega_L)} + \right. \\ & \left. \left. + \frac{20e^{2i\theta}}{\lambda + \lambda_4 - i(\omega - 2\omega_L)} + \frac{20e^{-2i\theta}}{\lambda + \lambda_4 - i(\omega + 2\omega_L)} + \frac{18}{\lambda + \lambda_4 - i\omega} \right] \right\} \end{aligned}$$

and

$$P(\omega) = \frac{\alpha_1 \alpha_2}{\alpha_1 + \alpha_2} e^{-\frac{\sigma^2}{2} \omega^2} \left(\frac{1}{\alpha_1 + i\omega} + \frac{1}{\alpha_2 - i\omega} \right) = \frac{\alpha_1 \alpha_2 e^{-\frac{\sigma^2}{2} \omega^2}}{\alpha_1 \alpha_2 + \omega^2 - i\omega(\alpha_1 - \alpha_2)}.$$

The calculation is long and tedious. Frequent use is made of the

inverse Fourier transform:

$$F^{-1} \left[\frac{1}{\beta - i\omega} \frac{e^{-r^2 \omega^2}}{\gamma + i\omega} \right] = \frac{S(t, \gamma, r) + S(-t, \beta, r)}{\gamma + \beta}$$

where

$$S(t, \alpha, r) = \frac{1}{2} e^{\alpha t + \alpha^2 r^2} \operatorname{erfc} \left(\frac{t}{2r} + \alpha r \right).$$

The result is

$$\begin{aligned} W'(t) = & \frac{\alpha_1 \alpha_2}{\alpha_1 + \alpha_2} \lambda \left\{ \mu(t, \lambda) + \frac{3}{4} A_2 \operatorname{Re} \left[e^{2i\theta} \mu(t, \lambda + \lambda_2 + 2i\omega_L) \right] \right. \\ & \left. + \frac{1}{4} A_2 \mu(t, \lambda + \lambda_2) \right. \\ & \left. + \frac{35}{64} A_4 \operatorname{Re} \left[e^{4i\theta} \mu(t, \lambda + \lambda_4 + 4i\omega_L) \right] + \frac{5}{16} A_4 \right. \\ & \left. \operatorname{Re} \left[e^{2i\theta} \mu(t, \lambda + \lambda_4 + 2i\omega_L) \right] \right. \\ & \left. + \frac{9}{64} A_4 \mu(t, \lambda + \lambda_4) \right\} \end{aligned}$$

where

$$\begin{aligned} \mu(t, \beta) = \mu(t, \beta, \alpha_1, \alpha_2, r) &= F' \left[\frac{1}{\beta - i\omega} \left(\frac{e^{-r^2 \omega^2}}{\alpha_1 + i\omega} + \frac{e^{-r^2 \omega^2}}{\alpha_2 - i\omega} \right) \right] \\ &= \frac{S(t, \alpha_1, r) + S(-t, \beta, r)}{\alpha_1 + \beta} + \frac{S(t, -\alpha_2, r) + S(-t, \beta, r)}{\alpha_2 - \beta}. \end{aligned}$$

Here, $r = \frac{\sigma}{\sqrt{2}}$ = normalized width of the Gaussian distribution. All the other parameters have been defined above.

A.7 The Response of the Multichannel Analyzer

The last modification the perturbed angular correlation is subjected to, occurs when the time delay information is stored in different channels of the multichannel analyzer.

In the following, it is assumed that the time-to-amplitude converter and the analyzer have no differential non-linearities, or that the appropriate corrections were made so that each and every channel has the same, fixed time width "T". It is also assumed that each channel has a rectangular shape so that an event due to time delay t has unit probability of being stored in channel "j" if $t_j \leq t < t_j + T$ and zero probability if $t < t_j$ or $t \geq t_j + T$.

A.8 The Observed Discrete Correlation Function

It now remains to sum the continuous distribution, derived above, over the channels' widths, i.e., the resulting discrete distribution is $W'(j) = \int_{t_j}^{t_j + T} W'(t) dt$, where j refers to the j 'th channel. The calculation is straightforward though tedious, and the resulting discrete distribution is:

$$\text{Let } S(t, \gamma, r) = \frac{1}{2} e^{\gamma t} + \gamma^2 r^2 \operatorname{erfc} \left(\frac{t}{2r} + \gamma r \right)$$

$$\text{and } U(t, T, \gamma, r) = S(t + T, \gamma, r) - S(t, \gamma, r)$$

then,

$$W'(j) = \operatorname{Re}[W_1 + W_2 - W_3 - W_4 + W_5]$$

where,

$$W_1 = U(t_j, T, \alpha_1, r) \frac{\lambda \alpha_2}{\alpha_1 + \alpha_2} \left[\frac{1}{\lambda + \alpha_1} + \frac{1/4 A_2}{\lambda + \lambda_2 + \alpha_1} + \frac{9/64 A_4}{\lambda + \lambda_4 + \alpha_1} \right. \\ \left. \frac{3/4 A_2 e^{2i\theta}}{\lambda + \lambda_2 + \alpha_1 - 2i\omega_L} + \frac{5/16 A_4 e^{2i\theta}}{\lambda + \lambda_4 + \alpha_1 + 2i\omega_L} + \frac{35/64 A_4 e^{4i\theta}}{\lambda + \lambda_4 + \alpha_1 + 4i\omega_L} \right]$$

$$W_2 = U(t_j, T, -\alpha_2, r) \frac{\lambda \alpha_1}{\alpha_1 + \alpha_2} \left[\frac{1}{\lambda - \alpha_2} + \frac{1/4 A_2}{\lambda + \lambda_2 - \alpha_2} + \frac{9/64 A_4}{\lambda + \lambda_4 - \alpha_2} \right. \\ \left. \frac{3/4 A_2 e^{2i\theta}}{\lambda + \lambda_2 - \alpha_2 + 2i\omega_L} + \frac{5/16 A_4 e^{2i\theta}}{\lambda - \lambda_4 - \alpha_2 + 2i\omega_L} + \frac{35/64 A_4 e^{4i\theta}}{\lambda + \lambda_4 - \alpha_2 + 4i\omega_L} \right]$$

$$W_3 = U(t_j, T, \theta, r) \lambda \left[\frac{\lambda + \alpha_1 - \alpha_2}{(\lambda + \alpha_1)(\lambda - \alpha_2)} + \frac{1/4 A_2 (\lambda + \lambda_2 + \alpha_1 - \alpha_2)}{(\lambda - \lambda_2 + \alpha_1)(\lambda + \lambda_2 - \alpha_2)} \right. \\ \left. + \frac{9/64 A_4 (\lambda + \lambda_4 + \alpha_1 - \alpha_2)}{(\lambda + \lambda_4 + \alpha_1)(\lambda + \lambda_4 - \alpha_2)} + \frac{3/4 A_2 e^{2i\theta} (\lambda + \lambda_2 + \alpha_1 - \alpha_2 + 2i\omega_L)}{(\lambda + \lambda_2 + \alpha_1 + 2i\omega_L)(\lambda + \lambda_2 - \alpha_2 + 2i\omega_L)} \right. \\ \left. + \frac{5/16 A_4 e^{2i\theta} (\lambda + \lambda_4 + \alpha_1 - \alpha_2 + 2i\omega_L)}{(\lambda + \lambda_4 + \alpha_1 + 2i\omega_L)(\lambda + \lambda_4 - \alpha_2 + 2i\omega_L)} \right. \\ \left. + \frac{35/64 A_4 e^{4i\theta} (\lambda + \lambda_4 + \alpha_1 - \alpha_2 + 4i\omega_L)}{(\lambda + \lambda_4 + \alpha_1 + 4i\omega_L)(\lambda + \lambda_4 - \alpha_2 + 4i\omega_L)} \right]$$

$$W_4 = U(-t_j, -T, \theta, r) \lambda \alpha_1 \alpha_2 \left[\frac{1}{\lambda (\lambda + \alpha_1) (\lambda - \alpha_2)} + \right. \\ \left. + \frac{1/4 A_2}{(\lambda + \lambda_2) (\lambda + \lambda_2 + \alpha_1) (\lambda + \lambda_2 - \alpha_2)} + \frac{9/64 A_4}{(\lambda + \lambda_4) (\lambda + \lambda_4 + \alpha_1) (\lambda + \lambda_4 - \alpha_2)} \right. \\ \left. + \frac{3/4 A_2 e^{2i\theta}}{(\lambda + \lambda_2 + 2i\omega_L) (\lambda + \lambda_2 + \alpha_1 + 2i\omega_L) (\lambda + \lambda_2 - \alpha_2 + 2i\omega_L)} \right. \\ \left. + \frac{5/16 A_4 e^{2i\theta}}{(\lambda + \lambda_4 + 2i\omega_L) (\lambda + \lambda_4 + \alpha_1 + 2i\omega_L) (\lambda + \lambda_4 - \alpha_2 + 2i\omega_L)} \right]$$

$$\begin{aligned}
& + \left[\frac{35/64 A_4 e^{4i\theta}}{(\lambda + \lambda_4 + 4i\omega_L)(\lambda + \lambda_4 + \alpha_1 + 4i\omega_L)(\lambda + \lambda_4 - \alpha_2 + 4i\omega_L)} \right] \\
W_5 = & + \lambda \alpha_1 \alpha_2 \left[\frac{1}{\lambda(\lambda + \alpha_1)(\lambda - \alpha_2)} \right. \\
& U(-t_j, -T, \lambda, r) + \frac{1/4 A_2}{(\lambda + \lambda_2)(\lambda + \lambda_2 + \alpha_1)(\lambda + \lambda_2 - \alpha_2)} U(-t_j, -T, \lambda + \lambda_2, r) \\
& + \frac{9/64 A_4}{(\lambda + \lambda_4)(\lambda + \lambda_4 + \alpha_1)(\lambda + \lambda_4 - \alpha_2)} U(-t_j, -T, \lambda + \lambda_4, r) + \\
& + \frac{3/4 A_2 e^{2i\theta} U(-t_j, -T, \lambda + \lambda_2 + 2i\omega_L, r)}{(\lambda + \lambda_2 + 2i\omega_L)(\lambda + \lambda_2 + \alpha_1 + 2i\omega_L)(\lambda + \lambda_2 - \alpha_2 + 2i\omega_L)} \\
& + \frac{5/16 A_4 e^{2i\theta} U(-t_j, -T, \lambda + \lambda_4 + 2i\omega_L, r)}{(\lambda + \lambda_4 + 2i\omega_L)(\lambda + \lambda_4 + \alpha_1 + 2i\omega_L)(\lambda + \lambda_4 - \alpha_2 + 2i\omega_L)} \\
& \left. + \frac{35/64 A_4 e^{4i\theta} U(-t_j, -T, \lambda + \lambda_4 + 4i\omega_L, r)}{(\lambda + \lambda_4 + 4i\omega_L)(\lambda + \lambda_4 + \alpha_1 + 4i\omega_L)(\lambda + \lambda_4 - \alpha_2 + 4i\omega_L)} \right] .
\end{aligned}$$

This last result demonstrates the rather drastic modification the perturbed correlation pattern undergoes (fundamentally, at least) due to the response of the correlation apparatus. It is of interest to investigate the behavior of the five terms in $W'(j)$ when the response of the components of the apparatus becomes perfect.

i.e., as $r \rightarrow 0$ or $\alpha_1, \alpha_2 \rightarrow \infty$.

- (a) The first term vanishes when either $r \rightarrow 0$ or $\alpha_1 \rightarrow \infty$.
- (b) The second term vanishes when either $r \rightarrow 0$ or $\alpha_2 \rightarrow \infty$.
- (c) The third term vanishes when either $r \rightarrow 0$ or both α_1 and $\alpha_2 \rightarrow \infty$.
- (d) The fourth term vanishes only when $r \rightarrow 0$.
- (e) The fifth term does not vanish in either case.

$$\text{If } r = 0, \text{ then } S(t, \gamma, 0) = \begin{cases} 0 & \text{if } t > 0 \\ \frac{1}{2} & \text{if } t = 0 \\ e^{\gamma t} & \text{if } t < 0 \end{cases}$$

so that for $t > 0$

$$U(-t, -T, \gamma, 0) = - (1 - e^{-\gamma t}) e^{-\gamma t}$$

and so, if $r = 0$ as well as $\alpha_1 \rightarrow \infty$ and $\alpha_2 \rightarrow \infty$, the observed correlation reduces to

$$\begin{aligned} W'(j) \xrightarrow[\alpha_1 \alpha_2 \rightarrow \infty]{r = 0} \lambda e^{-\lambda T} j \left\{ \frac{1 - e^{-\lambda T}}{\lambda} + A_2 e^{-\lambda 2^t j} \operatorname{Re} \left[\frac{1}{4} \frac{1 - e^{-(\lambda + \lambda_2)T}}{\lambda + \lambda_2} \right. \right. \\ \left. \left. + \frac{3}{4} e^{2i(\theta - \omega_L t_j)} \frac{1 - e^{-(\lambda + \lambda_2 + 2i\omega_L)T}}{\lambda + \lambda_2 + 2i\omega_L} \right] \right. \\ \left. + A_4 e^{-\lambda_4 t_j} \operatorname{Re} \left[\frac{9}{64} \frac{1 - e^{-(\lambda + \lambda_4)T}}{\lambda + \lambda_4} + \frac{5}{16} e^{2i(\theta - \omega_L t_j)} \frac{1 - e^{-(\lambda + \lambda_4 + 2i\omega_L)T}}{\lambda + \lambda_4 + 2i\omega_L} \right. \right. \\ \left. \left. + \frac{35}{64} e^{4i(\theta - \omega_L t_j)} \frac{1 - e^{-(\lambda + \lambda_4 + 4i\omega_L)T}}{\lambda + \lambda_4 + 4i\omega_L} \right] \right\}. \end{aligned}$$

It can be easily verified that the original correlation $W(t)$ is obtained if the channel width $T \rightarrow 0$, by transforming the discrete variables into continuous ones in the usual way, i.e., $W'(j) \rightarrow W'(t)dt$, $t_j \rightarrow t$ and $T \rightarrow dt$.

A.9 Useful, Simplified Versions of the Observed Correlation

Inspection of the "experimental" angular correlation expression $W'(j)$ reveals that several terms in it are independent of the precession frequency. Therefore, analysis is simplified considerably if one observes the difference $WD(j, \theta) = W'(j, +\omega_L, \theta) - W'(j, -\omega_L, \theta)$.

The calculation is simple if use is made of the fact that

$$W'(j, +\omega_L, \theta) - W'(j, -\omega_L, \theta) = W'(j, \omega_L, +\theta) - W'(j, \omega_L, -\theta).$$

If, in addition, the observation is performed at any of the angles $\theta = \pi/4, 3\pi/4, 5\pi/4$ or $7\pi/4$ between the detectors, further simplification is achieved and we get

$$\begin{aligned} WD(j, \theta = 3\pi/4) = & U(t_j, T, \alpha_1, r) \frac{\lambda \alpha_2}{\alpha_1 + \alpha_2} \operatorname{Im} \left\{ \frac{3/2 A_2}{\lambda + \lambda_2 + \alpha_1 + 2i\omega_L} \right. \\ & \left. + \frac{5/8 A_4}{\lambda + \lambda_4 + \alpha_1 + 2i\omega_L} \right\} \\ & + U(t_j, T, -\alpha_2, r) \frac{\lambda \alpha_1}{A_1 + \alpha_2} \operatorname{Im} \left\{ \frac{3/2 A_2}{\lambda + \lambda_2 - \alpha_2 + 2i\omega_L} \right. \\ & \left. + \frac{5/8 A_4}{\lambda + \lambda_4 - \alpha_2 + 2i\omega_L} \right\} \\ & - U(t_j, T, 0, r) \lambda \operatorname{Im} \left\{ \frac{3/2 A_2 (\lambda + \lambda_2 + \alpha_1 - \alpha_2 + 2i\omega_2)}{(\lambda + \lambda_2 + \alpha_1 + 2i\omega_L) (\lambda + \lambda_2 - \alpha_2 + 2i\omega_L)} \right. \\ & \left. + \frac{5/8 A_4 (\lambda + \lambda_4 + \alpha_1 - \alpha_2 + 2i\omega_L)}{(\lambda + \lambda_4 + \alpha_1 + 2i\omega_L) (\lambda + \lambda_4 - \alpha_2 + 2i\omega_L)} \right\} \\ & - U(-t_j, -T, 0, r) \lambda \alpha_1 \alpha_2 \\ & \operatorname{Im} \left\{ \frac{3/2 A_2}{(\lambda + \lambda_2 + 2i\omega_L) (\lambda + \lambda_2 + \alpha_1 + 2i\omega_L) (\lambda + \lambda_2 - \alpha_2 + 2i\omega_L)} \right\} \end{aligned}$$

$$\begin{aligned}
& + \frac{5/8 A_2}{(\lambda + \lambda_4 + 2i\omega_L)(\lambda + \lambda_4 + \alpha_1 + 2i\omega_L)(\lambda + \lambda_4 - \alpha_2 + 2i\omega_L)} \Bigg\} \\
& + \lambda \alpha_1 \alpha_2 \operatorname{Im} \left\{ \frac{3/2 A_2 U(-t_j, -T, \lambda + \lambda_2 + 2i\omega_L, r)}{(\lambda + \lambda_2 + 2i\omega_L)(\lambda + \lambda_2 + \alpha_1 + 2i\omega_L)(\lambda + \lambda_2 - \alpha_2 + 2i\omega_L)} \right. \\
& \left. + \frac{5/8 A_4 U(-t_j, -T, \lambda + \lambda_4 + 2i\omega_L, r)}{(\lambda + \lambda_4 + 2i\omega_L)(\lambda + \lambda_4 + \alpha_1 + 2i\omega_L)(\lambda + \lambda_4 - \alpha_2 + 2i\omega_L)} \right\}.
\end{aligned}$$

Finally, for the specific case in which $\lambda_2 = \lambda_4 = 0$ and where identical detectors are used ($\alpha_1 = \alpha_2 = \alpha$) we get:

$$\begin{aligned}
\text{WD}(j, \theta = 3\pi/4) &= \lambda \left(\frac{3}{4} A_2 + \frac{5}{16} A_4 \right) \left\{ U(t_j, T, \alpha, r) \operatorname{Im} \left[\frac{1}{\lambda + \alpha + 2i\omega_L} \right] \right. \\
&+ U(t_j, T, -\alpha, r) \operatorname{Im} \left[\frac{1}{\lambda - \alpha + 2i\omega_L} \right] \\
&- U(t_j, T, 0, r) 2 \operatorname{Im} \left[\frac{\lambda + 2i\omega_L}{(\lambda + \alpha + 2i\omega_L)(\lambda - \alpha + 2i\omega_L)} \right] \\
&- U(-t_j, -T, 0, r) 2\alpha^2 \operatorname{Im} \left[\frac{1}{(\lambda + 2i\omega_L)(\lambda + \alpha + 2i\omega_L)(\lambda - \alpha + 2i\omega_L)} \right] \\
&\left. + U(-t_j, -T, \lambda + 2i\omega_L, r) 2\alpha^2 \operatorname{Im} \left[\frac{1}{(\lambda + 2i\omega_L)(\lambda + \alpha + 2i\omega_L)(\lambda - \alpha + 2i\omega_L)} \right] \right\}.
\end{aligned}$$

The coefficient $\left(\frac{3}{4} A_2 + \frac{5}{16} A_4 \right)$ is seen to be proportional to the coefficient b_2 in the expansion $W(\theta) = 1 + b_2 \cos(2\theta) + b_4 \cos(4\theta)$.

APPENDIX B

SOURCE THICKNESS EFFECTS ON ANGULAR CORRELATIONS

The finite dimensions of the radioactive source have one obvious effect on a measurement of an angular correlation function. This effect is a reduction of the anisotropy of the correlation function. This attenuation is a simple consequence of the different contributions, from different points in the source. Therefore, each angle on the measured correlation curve represents an average of a range of angles about the measured angle. The effect is similar to the attenuation resulting from the finite solid angles subtended by the radiation counters (Sec. II.2). It is important for accurate measurement of angular correlation coefficients and the determination of mixing ratios of gamma rays. However, it does not modify precession measurements, although it makes them more difficult since it is easier to observe the precession of a highly anisotropic correlation pattern than an almost isotropic one.

A much more serious effect is the observation of an anisotropic correlation function when in fact it is completely isotropic. Absorption of gamma rays in the source material is responsible for such an effect and therefore it is enhanced in the case of low energy gamma rays. If θ denotes the angular separation of the two detectors (Fig. 1, Ch. II), then the coincidence rates at $\theta = 180^\circ$ will invariably be smaller than the rate at $\theta = 90^\circ$. This effect is caused simply by the different thicknesses the source presents to

coincident gamma rays at different angles. Monitoring the 'singles' count rates of these gamma rays does not detect this effect since it only helps to physically center the radioactive source. It is for this reason that very thin cylindrical shells were used in the ^{223}Ra measurements.

In conclusion, there are two major effects due to source thickness, which modify the correlation function. The first attenuates it without changing its characteristics. It does not modify the results of precession measurements, based on the experimentally observed correlation function. The second, can result in an appearance of a 'fake' correlation function and affects both angular correlation and precession measurements.

REFERENCES

References to Chapter I

1. M. Levanoni, Phys. Rev. (to be published).
2. M. Levanoni, F.C. Zawislak, and D.D. Cook, Nuclear Phys. (to be published).
3. F.C. Zawislak, D.D. Cook and M. Levanoni, Physics Letters 30B (1969) 541.
4. M. Levanoni and F.C. Zawislak, to be published.

References to Part 1

1. E.L. Brady and M. Deutsch, Phys. Rev. 78 (1950) 558.
2. H. Aeppli, H. Albers-Schönberg, A.S. Bishop, H. Frauenfelder and E. Heer, Phys. Rev. 84 (1951) 370.
3. K. Alder, Helv. Phys. Acta 25 (1952) 235 and Phys. Rev. 84 (1951) 369; A. Abragam and R.V. Pound, Phys. Rev. 92 (1953) 943; H. Frauenfelder and R.M. Steffen in Alpha-, Beta-, and Gamma-Ray Spectroscopy ed. K. Siegbahn (North-Holland Publ. Co., Amsterdam 1965) Vol. 2, Ch. 19.
4. H. Frauenfelder and R.M. Steffen in Alpha-, Beta-, and Gamma-Ray Spectroscopy, ed. K. Siegbahn (North-Holland Publ. Co., Amsterdam 1965) p. 1031.
5. H. Ferentz and N. Rosenzweig, Argonne National Laboratory Report 5324 (1954). A.H. Wapstra, G.J. Nijgh and R. Van Lieshout, Nuclear Spectroscopy Tables (North-Holland Publ. Co. Amsterdam 1959).

6. A. Abragam and R.V. Pound, Phys. Rev. 92 (1953) 943.
7. D. Dillenburg and Th. A.J. Maris, Nuclear Phys. 33 (1962) 208
and Physics Letters 5 (1963) 357.
8. E. Bodenstedt and J.D. Rogers in Perturbed Angular Correlations
ed. E. Karlsson, E. Mattias and K. Siegbahn (North-Holland
Publ. Co., Amsterdam 1964) p. 95.
9. G. Racah, Phys. Rev. 62 (1942) 438 and 63 (1943) 367.

References to Part 2

1. K. Kumar and M. Baranger, Nuclear Phys. A122, (1968) 273.
2. G. Goldring, R. Kalish and H. Spehl, Nuclear Phys. 80, (1966) 33.
3. P. Gilad, G. Goldring, R. Herber and R. Kalish, Nuclear Phys.
A91 (1967) 85.
4. V.S. Shirley in "Hyperfine Structure and Nuclear Radiation",
edited by E. Mathias and D.A. Shirley, North-Holland Publ.
Co. (1968).
5. C.M. Lederer, J.M. Hollander and I. Perlman in Table of Isotopes,
John Wiley & Son, Inc. (1967).
6. T. Yamazaki, H. Ikegami and M. Sakai, Nuclear Phys. A131, (1969)
169.
7. See Ref. 4
8. L. Keszthelyi, I. Berkes, I. Deszi and L. Pocs, Nuclear Phys.
71, (1965) 662.
9. G.C. Pramila and L. Grodzins, Bull. Am. Phys. Soc. 11, (1966) 353.
10. L. Grodzins in Annual Review of Nuclear Science vol. 18,
edited by E. Segre, Annual Review, Inc. (1968).

11. Y.K. Agarwal, C.V.K. Baba and S.K. Bhattacharjee, Nuclear Phys. 79 (1966) 437.
12. R. Kalish and L. Grodzins, Phys. Rev. 161 (1967) 1196.
13. J.A. Cameron, Canadian Journal of Phys. 42 (1964) 1680.
14. R. Beraud et al., in "Hyperfine Structure and Nuclear Radiation", edited by E. Mathias and D.A. Shirley, North-Holland Publ. Co. (1968).
15. O.B. Kenyon, L. Keszthelyi and J.A. Cameron, Canadian Journal of Phys. 21 (1969) 2395.
16. J. Thibaud, Compt. Rend. 191 (1930) 656.
17. S. Rosenblum, Compt. Rend. 188 (1929) 1401 and 190 (1930) 1124.
18. N. Bohr and F. Kalckar, Kgl. Danske Videnskab. Selskab. Mat. Fys. Medd. 14 (1937) 10.
19. C.F. Von Weizsäcker, Naturwiss. 27 (1939) 133.
20. E. Feenberg, Phys. Rev. 55 (1939) 504;
N. Bohr and J.A. Wheeler, Phys. Rev. 56 (1939) 426.
21. J. Rainwater, Phys. Rev. 79 (1950) 432.
22. A. Bohr, Phys. Rev. 81 (1951) 134.
23. L.L. Foldy and F.J. Milford, Phys. Rev. 80 (1950) 751.
24. A. Bohr, Kgl. Danske Videnskab. Selskab Mat. Fys. Medd. 26 (1952) 14.
25. A. Bohr and B.R. Mottelson, Kgl. Danske Videnskab Selskab Mat. Fys. Medd. 27 (1953) 16.
26. J.P. Davidson, Rev. Mod. Phys. 37 (1965) 105.
27. A.M. Lane, Nuclear Theory (W.A. Benjamin, Inc., New York 1964).
28. G.E. Brown, Unified Theory of Nuclear Models and Forces (North-Holland Publ. Co. 1967).

29. G.T. Emery et al., Phys. Rev. 129 (1963) 2597.
30. J. Burde, R.M. Diamond and F.S. Stephens, Nuclear Phys. A92
(1967) 306.
31. A. Bohr, B.R. Mottelson and D. Pines, Phys. Rev. 110 (1958) 936.
32. D.R. Inglis, Phys. Rev. 96 (1954) 1059 and 103 (1956) 1786.
33. S.G. Nilsson and O. Prior, Danske Videnskab. Selskab. Mat. Fys.
Medd. 32 (1960) 16.
34. O. Prior, F. Boehm, and S.G. Nilsson, Nuclear Phys. A110
(1968) 257.
35. A. Faessler and W. Greiner, Z. Phys. 168 (1962) 425 and 170
(1962) 105.
36. W. Greiner, Nuclear Phys. 80 (1966) 417.
37. W. Greiner, Z. Phys. 179 (1964) 343.
38. O. Nathan and S.G. Nilsson, in Alpha-, Beta-, and Gamma-Ray
Spectroscopy, ed. K. Siegbahn (North-Holland Publ. Co.
Amsterdam 1965) p. 602.
39. S.G. Nilsson, Kgl. Danske Videnskab. Selskab. Mat. Fys. Medd.
29 (1955) 16.
B.R. Mottelson and S.G. Nilsson, Kgl. Danske Videnskab. Selskab.
Mat. Fys. Skrifter 1 (1959) 8.
40. S.T. Belyaer, Kgl. Danske Videnskab. Selskab. Mat. Fys. Medd.
31 (1959) 11.
41. L.S. Kisslinger and R.A. Sorensen, Kgl. Danske Videnskab.
Selskab. Mat. Fys. Medd. 32 (1960) 9.
42. L.S. Kisslinger and R.A. Sorensen, Rev. Mod. Phys. 35 (1963) 853.
43. M. Baranger and K. Kumar, Nuclear Phys. 62 (1965) 113.

44. M. Baranger and K. Kumar, Nuclear Phys. 110 (1968) 490.
45. K. Kumar and M. Baranger, Nuclear Phys. 110 (1968) 529.
46. M. Baranger and K. Kumar, Nuclear Phys.
47. K. Kumar and M. Baranger, Nuclear Phys. A122, (1968) 273.
48. K. Kumar and M. Baranger, Nuclear Phys. A92 (1967) 608.
49. D.K. Bès, Kgl. Danske Videnskab. Selskab. Mat. Phys. Medd. 33 (1961) 2.
A.K. Kerman, Ann. of Phys. 12 (1961) 300.

References to Part 3

1. P.C. Simms and R.M. Steffen, Phys. Rev. 108 (1957) 1459.
2. Rietjens, Van Den Bold and Heylingers, Physics 21 (1955) 899.
3. A. Maier and K.P. Mayer, Helv. Phys. Acta. 30 (1957) 611.
4. E. Matthias, S.S. Rosenblum and D.A. Shirley, Phys. Rev. Letters 14 (1965) 461.
5. L. Keszthelyi, I. Berkes, I. Dezsi, B. Molner and L. Pocs, Physics Letters 8 (1964) 195.
6. J. Murray, T.A. McMath and J.A. Cameron, Canadian Journal of Phys. 46 (1968) 75.
7. V.S. Shirley in Hyperfine Structure and Nuclear Radiation ed. E. Matthias and D.A. Shirley (North-Holland Publ. Co., Amsterdam 1968).
8. J.D. Bowman and F.C. Zawislak, Nuclear Phys. A138 (1969) 90.
9. E. Anselmo, L. Grodzins and R. Kalish, Physics Letters 30B (1969) 538.

10. E.N. Kaufmann, H.P. Lie and D.E. Murnick, International Conference on Nuclear Reaction Induced by Heavy Ions (Heidelberg 1969).
11. H.W. Kugel, T. Polza and R.R. Borchers, B.A.P.S. 14 (1970) 1202.
12. F.B. Gil, R. Foucher and G.V. Pettit, J. Phys. Radium 22 (1961) 289.
13. H. Vartapetian, C.R. Acad. Sci. 246 (1958) 1680.
14. E. Fermi, Z. Phys. 60 (1930) 320.
15. R.M. Sternheimer, Phys. Rev. 84 (1952) 244.
16. A.J. Freeman and R.E. Watson, in Treatise on Magnetism, Vol. IIA, ed. Suhl-Rado (Academic Press, 1965).
17. M.A. Ruderman and C. Kittel, Phys. Rev. 96 (1954) 99.
T. Kasuya, Progr. Theoret. Phys. (Kyoto) 16 (1956) 45.
K. Yosida, Phys. Rev. 106 (1957) 893.
18. D.A. Shirley and G.A. Westenbarger, Phys. Rev. 138 (1965) A170.
19. A.E. Balabanov and N.N. Delyagin, Soviet Phys. JETP (English transl.) 27 (1968) 752.